# SEISMIC PERFORMANCE COMPARISON OF BASE-ISOLATED HOSPITAL BUILDING WITH VARIOUS ISOLATOR MODELING APPROACHES

A THESIS SUBMITTED TO
THE GRADUATE SCHOOL OF NATURAL AND APPLIED SCIENCES
OF
MIDDLE EAST TECHNICAL UNIVERSITY

BY

ESER ÇABUK

IN PARTIAL FULFILLMENT OF THE REQUIREMENTS
FOR
THE DEGREE OF MASTER OF SCIENCE
IN
CIVIL ENGINEERING

SEPTEMBER 2021

Approval of the thesis:

**SEISMIC PERFORMANCE COMPARISON OF BASE-ISOLATED HOSPITAL BUILDING WITH VARIOUS ISOLATOR MODELING APPROACHES**

submitted by **ESER ÇABUK** in partial fulfillment of the requirements for the degree of **Master of Science** i**n Civil Engineering, Middle East Technical University** by,

Prof. Dr. Halil Kalıpçılar
Dean, Graduate School of **Natural and Applied Sciences** _____

Prof. Dr. Ahmet Türer
Head of the Department, **Civil Engineering** _____

Prof. Dr. Uğurhan Akyüz
Supervisor, **Civil Engineering** _____

**Examining Committee Members:**

Prof. Dr. Ahmet Yakut
Civil Engineering METU _____

Prof. Dr. Uğurhan Akyüz
Civil Engineering METU _____

Prof. Dr. Özgür Kurç
Civil Engineering METU _____

Prof. Dr. Murat Altuğ Erberik
Civil Engineering. METU _____

Assist. Prof. Dr. Fatih Sütçü
Civil Engineering. ITU _____

Date: 09.09.2021

**I hereby declare that all information in this document has been obtained and presented in accordance with academic rules and ethical conduct. I also declare that, as required by these rules and conduct, I have fully cited and referenced all material and results that are not original to this work.**

Name Last name : Eser Çabuk

Signature :

# ABSTRACT

## SEISMIC PERFORMANCE COMPARISON OF BASE-ISOLATED HOSPITAL BUILDING WITH VARIOUS ISOLATOR MODELING APPROACHES

Çabuk, Eser
Master of Science, Civil Engineering
Supervisor : Prof. Dr. Uğurhan Akyüz

September 2021, 147 pages

In Turkey, seismic base isolation have become mainly used passive earthquake control system especially among hospital structures after the amendment of Ministry of Health in 2014, regulating the design of hospitals in high seismic zones. Rubber and sliding type of isolators have been applied, and several different hysteresis models, which are essentially acceptable in seismic codes, were used in their design process. However, due to the complexity in the development of highly nonlinear models, engineers tend to use more practical ones such as smoothed or sharp bilinear models. Literature and experience have shown that differences in hysteresis characteristics may lead to variance in performance parameters resulting in possible overdesign or underdesign. In this thesis, to assess the effect of the modeling approach on seismic performance, for a selected hospital building, high damping rubber bearing, and friction pendulum-type isolators were designed according to Turkish Building Seismic Code and evaluated in terms of structural performance. For both designs, commonly used bilinear and highly nonlinear isolator hysteresis models from the literature were adopted, and structural models were created for 2475

years, and 475 years return period seismic ground motions. Three-dimensional nonlinear time history analyses were conducted on the building model under a set of 11 ground motions. For each model, structural performance is evaluated and compared in terms of (i) maximum isolator displacements, (ii) base shear reactions, (iii) story accelerations, (iv) inter-story drifts, (v) isolator hysteretic response and (vi) uplift behavior conforming the international code limitations. The results show that when bilinear models are used instead of more accurate nonlinear models, there is a significant variation in the superstructural response, especially for sharply bilinear models.

Keywords: Seismic Base Isolation, Nonlinear Model, Bilinear Model, High Damping Rubber Bearing, Friction Pendulum Isolator

# ÖZ

## FARKLI YAKLAŞIMLAR KULLANILARAK MODELLENEN İZOLATÖRLÜ HASTANE BİNASININ DEPREM PERFORMANS KARŞILAŞTIRMASI

Çabuk, Eser
Yüksek Lisans, İnşaat Mühendisliği
Tez Yöneticisi: Prof. Dr. Uğurhan Akyüz

Eylül 2021, 147 sayfa

Türkiye'de sismik taban izolasyonu, 2014 yılında Sağlık Bakanlığı'nın yüksek deprem bölgelerindeki hastanelerin tasarımını düzenleyen değişikliğinden sonra özellikle hastane yapılarında ağırlıklı olarak kullanılan pasif deprem kontrol sistemi haline gelmiştir. Kauçuk ve kayar tip izolatörler uygulanmış ve tasarım süreçlerinde esasen şartnemelerde kabul edilen birkaç farklı histeresis modeli kullanılmıştır. Ancak, yüksek düzeyde doğrusal olmayan modellerin geliştirilmesindeki karmaşıklık nedeniyle, mühendisler çift doğrusal modeller gibi daha pratik olanları kullanma eğilimindedir. Literatür ve geçmiş deneyimler, histeresis özelliklerindeki farklılıkların, olası aşırı tasarım veya eksik tasarım ile sonuçlanan performans parametrelerinde farklılıklara yol açabileceğini göstermiştir. Bu tez çalışmasında, modelleme yaklaşımının sismik performansa etkisini değerlendirmek macıyla, seçilmiş bir hastane binası için yüksek sönümlü kauçuk izolatör ve çift yüzeyli sürtünmeli sarkaç tipi izolatörler Türkiye Bina Deprem Yönetmeliği'ne (TBDY2019) uygun olarak tasarlanmış ve değerlendirilmiştir. Her iki tasarım için de literatürde yaygın olarak kullanılan çift doğrusal ve doğrusal olmayan izolatör histeresis davranış modelleri benimsenmiş ve 2475 yıl ve 475 yıl geri dönüş periyotlu

deprem yer hareketleri için yapısal modeller oluşturulmuştur. Seçilen 11 yer hareketi seti altında Üç boyutlu zaman tanım alanında doğrusal olmayan analizler gerçekleştirilmiştir. Her izolatör modeli için yapısal performans, (i) maksimum izolatör yer değiştirmeleri, (ii) üstyapı ve taban kesme kuvvetleri, (iii) kat ivmeleri, (iv) katlar arası ötelenmeler, (v) izolatör histeretik davranışı ve (vi) izolatör kalkma davranışı açısından uluslararası şartnamelere göre değerlendirilmiş ve karşılaştırılmıştır. Sonuçlardan hareketle, daha gerçekçi doğrusal olmayan modeller yerine çift doğrusal modeller kullanıldığında, maksimum izolatör yer değiştirmelerinin ve histeretik eğrilerin olduğundan az veya fazla tahmin edildiğini göstermektedir. Bununla birlikte, özellikle keskin çift doğrusal modeller için üstyapı performansında önemli bir artış gözlenmiştir.

Anahtar Kelimeler: Sismik Taban İzolasyonu, Doğrusal Olmayan Model, Çift Doğrusal Model, Yüksek Sönümlü Kauçuk İzolatör, Sürtünmeli Sarkaç İzolatör

To My Family

## ACKNOWLEDGMENTS

First of all, I would like to thank and express my gratitude to my supervisor and director, Prof. Dr. Uğurhan Akyüz, for his guidance, patience, and support throughout my study and work-life. He offered valuable opportunities to develop my structural engineering skills in academic and professional life and self-development.

I also would like to thank Prof. Dr. Ahmet Yakut, with whom I had the chance to study and work together on different topics. His experience and guidance will support me in the later stages of my life as a structural engineer.

I want to express my deepest gratitude to the members of Bridgestone Corporation; Dr. Nobuo Murota, Dr. Shigenobu Suzuki, Dr. Takahiro Mori, and Dr. Fatih Sütçü from Istanbul Technical University. Working with them in collaborative research has always been a pleasure and contributed invaluable knowledge and experience for me during the preparation of this thesis.

This thesis would not have been possible without the support of my friends. I would like to thank Namık Erkal, Elife Çakır, Cansu Balku, Mehmet Ali Çetintaş, İsmet Gökhan, Remzi Mert Polatçelik and Ceren Maden. I also would like to thank Yunus Anıl Köşker for his friendship and a structural engineer fellowship during this MSc. degree.

Last but not least, I would like to express my love and appreciation to my family. I am very grateful to my mom and dad, Hasibe and Kerim, for their endless support, care, patience, and love. I also thank to my sister Esin Günalp, brother-in-law Yasin Günalp and my loving nephews Ceren and Kerem Günalp for their support and motivation. I feel fortunate to have such a family.

**TABLE OF CONTENTS**

## LIST OF TABLES

TABLES

## LIST OF FIGURES

FIGURES

## LIST OF ABBREVIATIONS

ABBREVIATIONS

| | |
|---|---|
| 2-D | Two Dimensional |
| 3-D | Three Dimensional |
| AASHTO | American Association of State Highway and Transportation Officials |
| ASCE7-16 | American Society of Civil Engineers 7-16 |
| Ave | Average |
| BL | Sharp Bilinear Model |
| BW | Bouc-Wen Bilinear Model |
| CSI | Computers and Structures Inc. |
| DBE | Design Basic Earthquake |
| DHI | Deformation-History Integral Type Model |
| ELFP | Equivalent Lateral Force Procedure |
| FNA | Fast Nonlinear Analysis |
| FPI | Friction Pendulum Isolator Model |
| FPS | Friction Pendulum System |
| HDRB | High Damping Rubber Bearing |
| LB | Lower Bound |
| LRB | Lead Rubber Bearing |
| MCE | Maximum Considered Earthquake |
| MLP | Multilinear Plastic |
| MoH | Ministry of Health of Turkey |
| Nom | Nominal |
| NRB | Natural Rubber Bearing |
| NTHA | Nonlinear Time History Analysis |
| PEER | Pacific Earthquake Engineering Research Center |
| Ph.D. | Doctor of Philosophy |

| | |
|---|---|
| RSN | Record Sequence Number from PEER database |
| SI | Seismic Isolation |
| TBDY2019 | Turkish Building Seismic Code 2019 |
| UB | Upper Bound |

# INTRODUCTION

Structures that can withstand earthquake ground motions have been successfully built. To withstand devastating eartuquake forces, the classical seismic design approach builds more rigid systems by increasing structural members and cross-sections and adding shear walls to the load carrying system. But this approach lead to higher inertial accelerations, and structural or non-structural damage have been allowed up to a certain limit. Furthermore, a new method is to sustain seismic effects with ductility and energy dissipation terms. Since early 1900s, many kinds of energy dissipating devices have been developed, such as viscous dampers, tuned mass dampers and seismic base isolation (SI). Base isolation has become one of the most influential and widely used passive protection systems around the world.

The aim of SI is to increase the natural vibration period of the structure by decoupling the superstructure from the foundation. Energy dissipating property of isolation layer is also commonly considered. This results in a reduction in both superstructural displacements and accelerations. In other words, SI provides dissipated energy (damping) for the superstructure to remain elastic and reduced accelerations for non-structural equipment protection.

The evolution of SI from the beginning to date is covered in Naeim (1986), Naeim & Kelly (1999), and Warn & Ryan (2012). The history dates back more than 100 years, starting with basic applications of introducing a layer of sand, mud or roller to decouple the structure from the ground. Modern applications frequently include two types of isolators. The rubber types often include natural rubber bearing (NRB), lead rubber bearing (LRB), and high damping rubber bearing (HDRB). The sliding-type isolators include single, double, and triple curved surface sliding systems (friction pendulum system, FPS) with or without frictional surface for system damping capability. The first modern application of rubber type isolator for seismic protection was a school building in Skopje, Yugoslavia, built in 1969. Since then, many

examples of SI applications have become widespread, and code developments have started across Japan, United States, China, Italy, Russia, and other earthquake-prone countries. The isolated building number has increased to tens of thousands of buildings around the world.

## 1.1 Rubber Type (Elastomeric) Isolators

The rubber type isolators typically consist of thin steel plates in-between natural rubber layers of a certain height, glued together under temperature and pressure, called vulcanization. The steel plates contribute vertical rigidity and rubber layers provide horizontal flexibility to the system. The damping is implemented in the isolator by a lead core in LRB or a special rubber compound in the HDRB system. In contrast, NRB isolators do not have significant damping properties. Schematic figures are given in Figure 1.1 for NRB and HDRBs, and Figure 1.2 for the LRB isolators. Squared isolators are shown in the figures and are often used in bridges. However, circular type bearings are the most commonly used among building structures in recent applications.

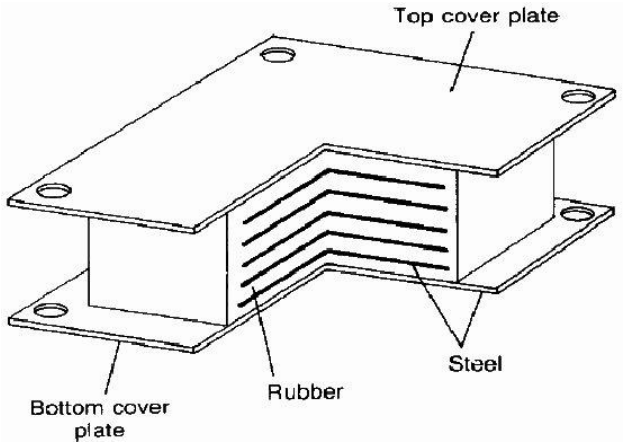


Figure 1.1. Natural and high damping rubber bearing (Kunde & Jandig, 2003)

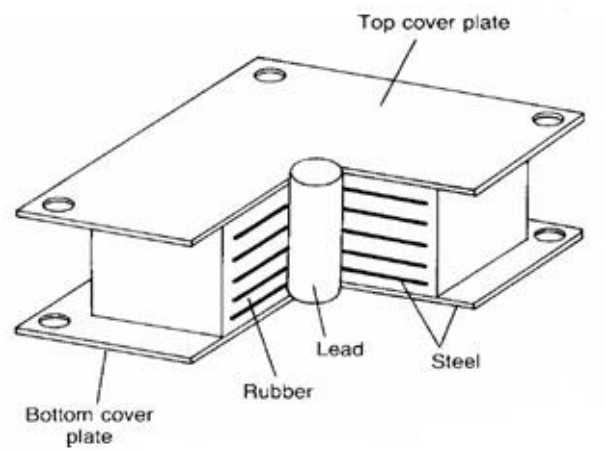


Figure 1.2. Lead rubber bearing (Kunde & Jandig, 2003)

## 1.2 Sliding Type Isolators

The sliding-type isolators (Figure 1.3) consist of a sliding element between flat or concave steel plates and act as the principle of a pendulum. When the inertial movement occurs, the restoring force is provided by the radius of curvature of the sliding surface (initially Teflon or different patented materials) and the the self-weight of the superstructure. The energy dissipation is satisfied by the friction between the curved surfaces. Occasionally, flat surface sliders with or without friction are used where there is no need for restoring force for the corresponding element.

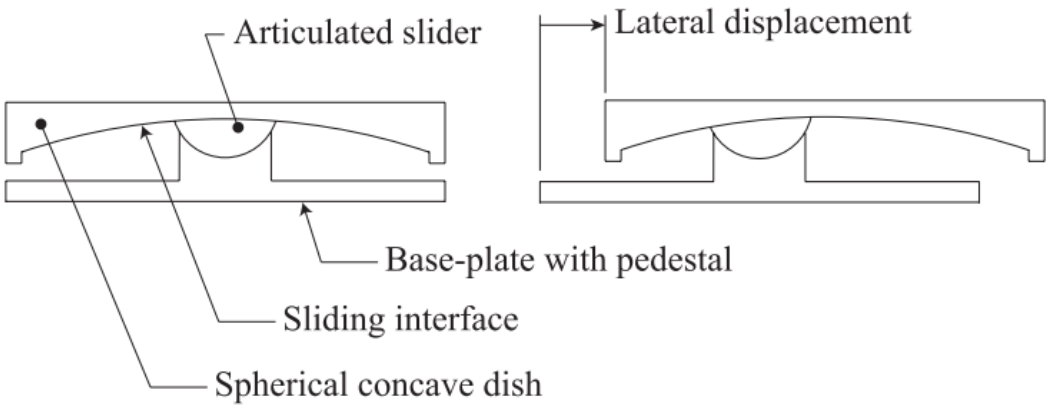


Figure 1.3. Sliding Isolator (Warn & Ryan, 2012)

## 1.3 Development of SI in Turkey

In Turkey, as a seismically active country, SI applications have become popular in 2000's, especially after the amendment of Ministry of Health in 2013 obligating the use of SI in hospitals with more than 100 beds and located in high seismic zones. The specification includes limitations on target performance of the structure, requirements on analysis and structural design, quality control and testing of isolators. Later in 2019, the updated Turkish Building Seismic Code (TBDY2019) was officially announced, including a performance-based design approach and base isolation chapter. Since 2013, dozens of large hospital buildings have already been constructed according to national and international codes (Erdik et al., 2018). Furthermore, airport roofs, bridges, viaducts, data centers, residential, industrial and storage buildings have been constructed, reaching a total of 104 isolated structures until 2018, including the ones under the planning stage mentioned in Murota et al. (2021). This number has been increasing rapidly since then. However, Erdik et al. (2018) also mention the lack of facilities and experience in architectural, engineering, production, testing and logistics aspects of a base isolation design in Turkey.

## 1.4 Problem Statement

Isolated buildings have been designed using linear and nonlinear approaches. Recent international codes (TBDY2019, ASCE7-16, Eurocode8, AASHTO) require isolators to be preliminarily designed with linear analyses such as equivalent lateral force approach or response spectrum analysis to evaluate maximum displacements and structural forces. Then, nonlinear time history analyses (NTHA) are conducted, and performance criteria are checked for both the isolation system and the superstructure. Those performance parameters generally include maximum displacements, structural forces, story accelerations, interstory drifts, isolator hysteresis and uplift behavior.

In the analytical modeling stage, researchers and engineers tend to use different mathematical models suggested by design codes or the literature to define the hysteretic behavior of isolators for NTHA. These include bilinear models (sharp and smoothed) and highly nonlinear models, which will be covered later in detail. The bilinear models are more practical and can easily be implemented in the structural analysis by following the design code guidelines. In contrast, nonlinear models which accurately capture the actual behavior are more complex to implement and require better comprehension of nonlinear dynamic isolator characteristics. These models were used in both research and design projects. However, experience and literature have shown that the characteristics of the hysteresis loops might introduce significant variations in performance parameters.

## 1.5 The Aim and Research Objectives

The aim of this study is to assess the effect of the isolator modeling approach on earthquake performance of 10 stories base-isolated reinforced concrete hospital building, with plan irregularity, under a set of 11 ground motions. The structural system consists primarily of beam-column frame elements. In addition, shear walls are present at the core regions, which significantly affects the isolation system design and evaluation. For the building, two types of isolation systems, HDRB, and double-curved type FPS were designed and evaluated primarily according to the Turkish seismic code (TBDY2019). In addition, international codes were also referenced where needed. The reason behind selecting HDRB and FPS is that they both show highly nonlinear responses under earthquake excitation. There is a sudden increase in stiffness of HDRB under high shear strains, whereas the nonlinear restoring stiffness of FPS type depends heavily on corresponding column axial load for which strict bilinear relationship might not be observed for both types. However, the findings of the research can also be partially applicable for LRB or other sliding-type isolators, as the same nonlinear models can be used.

The objectives of this research are as follows:

- To observe the effect of isolator modeling approach on the structural performance
- To highlight the advantages and drawbacks of each isolator model encountered during the design and analysis.

## 1.6 The Outline of the Thesis

In Chapter 1, a brief introduction and history of SI isolator types are mentioned. The research objectives are defined and a brief literature review regarding the objectives are given.

Chapter 2 includes information on the building model and the design and different modeling approaches of isolation elements.

In Chapter 3, seismic conditions of the building site, ground motion selection, and nonlinear time history analysis approach are discussed.

The analysis results are presented in Chapter 4. Maximum displacements, structural forces, story accelerations, inter-story drifts, hysteresis curves and uplift conditions are evaluated for each isolator type and modeling approach. Performance comparisons with code requirements are given.

Finally, Chapter 5 summarizes this study. Conclusions and recommendations are discussed.

# CHAPTER 1

# LITERATURE REVIEW

In this chapter, the literature review of the topics which is covered in this thesis is summarized. First, the nonlinear hysteresis models most often used by researchers and engineers are addressed, including bilinear and other nonlinear models for HDRB and FPS. Next, the studies, which focus on variation in structural performance when one of these models is used, will be mentioned. In addition, the uplift behavior of isolators are investigated.

## 2.1 Isolator Nonlinear Models

Adequacy of the force-displacement relationship of sharp bilinear (BL) models was investigated in numerous studies and recommended (Robinson, 1982; Skinner et al. 1993; Kikuchi & Aiken, 1997, Kampas & Makris, 2012, Vassiliou et al. 2013).In addition, international design codes besides Naeim and Kelly (1999) suggest all type isolators can essentially be modeled by bilinear models. An illustration of force-displacement relationship of the sharp BL model is shown in Figure 2.1 with the dotted line. Three parameters are associated with this model: the initial elastic stiffness, the characteristic strength and the post-yield (secondary) stiffness. A secondary parameter, yield displacement, is optionally neglected in most cases due to a small magnitude of elastic deformation of the isolator. A sharp and sudden corner is provided between stiffness transitions, for which the effects on the response will be discussed in the following chapters. After the maximum load in each cycle is reached, the unloading curve follows a parallel line of the same length with the previous loaded segments, in the opposite direction, until it reconnects the envelope

curve. The sharp bilinear model, which is implemented in the commercial structural analysis programs as a link element, does not account for the bilateral excitation of the ground motion components. In other words, the internal deformations are uncoupled, and the deformation in a direction does not affect the motion in the orthogonal direction (CSI Analysis Reference Manual, 2017).

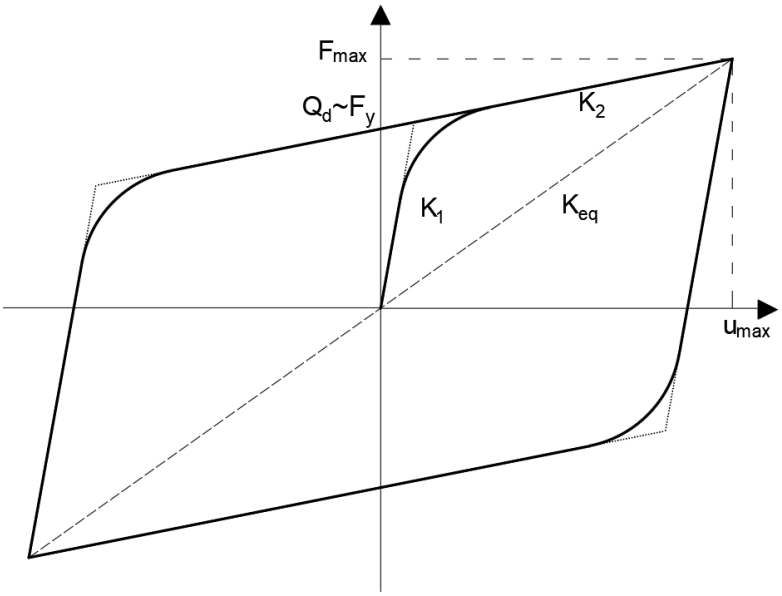


Figure 2.1. Force-displacement relationship of BL (dotted line) and BW (solid line)

Another bilinear model, called as smoothed bilinear (or Bouc-Wen, BW) model, was introduced by Bouc (1971) and modified by Wen (1976) and Park et al. (1986). This analytical model can be applied to a wide range of hysteretic systems and was verified for base isolation of a six-story reinforced concrete building by Nagarajaiah et al. (1991) for both elastomeric and sliding isolators. In Figure 2.1 with solid line, the hysteresis is defined by three parameters: elastic stiffness, the ratio of post-yield stiffness to elastic stiffness, and the yield force. Unlike the sharp bilinear model, the transition between initial and post-yield stiffness is smoothed by a circular yield surface function, and the two lateral degrees of freedom are coupled. Therefore, the model is able to capture nonlinear characteristics of isolators under biaxial lateral excitation. The vertical degree of freedom is linearly elastic and uncoupled from the

horizontal directions. This model is implemented in ETABS software as Rubber Isolator link element (CSI Analysis Reference Manual, 2017).

A nonlinear model which can be applicable for elastomeric isolators, specifically HDRB, was developed by Kato et al. (2015) and validated by Masaki et al. (2017). A time-independent "Deformation History Integral Type Model (DHI model)" can accurately capture the highly nonlinear behavior of rubber bearings under biaxial and uniaxial excitations. An elastoplastic model (DHI) was constructed by modifying the viscoelastic models of Simo and Hughes (1997) since the velocity dependency of restoring force was overestimated when compared by the HDRB test results in the original one. Although the real rubber has velocity dependence, the DHI model does not exhibit dependency on the strain rate. The characteristics of the hysteresis highly depend on the shear strain and have stiffness increase when the shear strain exceeds 200%. This model is also implemented in ETABS, named as High Damping Rubber Isolator Link (CSI Analysis Reference Manual, 2017). The axial behavior is linearly elastic and independent from the two coupled shear directions. The following parameters are required to define the DHI model. Isolator cross-sectional area, isolator effective height, added elastic stiffness. which controls elastic region of the response, hysteretic parameters (number of terms, control strain, and control strength) which affects the hysteretic behavior, damage parameters which define the damage function and elastic stiffness degradation (resistance ratio and control strain); and finally, stiffness for iteration which might change the convergence rate of the model.

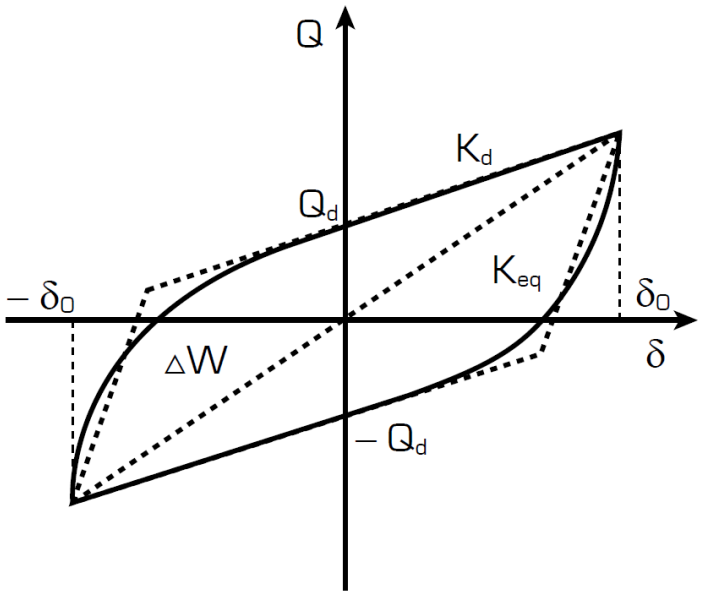


Figure 2.2. Force-displacement relationship of HDRB (solid line) (retrieved from Bridgestone Isolation Product Line-up)

Another highly nonlinear model can accurately capture the behavior of sliding isolators, recommended by Nagarajaiah et al. (1991). This model is an advanced model used both in research and practice and will be called as Friction Pendulum Isolator (FPI) model in this study. The horizontal frictional hysteretic behavior is based on the theory of smoothed bilinear model (Wen, 1976; Park et al., 1986). A pendulum behavior was also added by Zayas and Low (1990). The axial behavior of the model is always nonlinear, with a linear elastic compressive stiffness and zero tensile stiffness. The horizontal force-deformation behavior of the isolator is the same as the BW model, in Figure 2.1. Both shear directions are coupled with axial behavior. When the axial load on the isolator increases, the restoring stiffness increases, and lateral force also increases along with the frictional. The shear behavior is velocity dependent, and two types of friction coefficient are introduced; shear coefficient at fast velocities and zero velocity. Nagarajaiah et al. (1991) state that the friction coefficient essentially increases with sliding velocity. To construct the hysteresis loop, initial elastic stiffness, friction coefficient with zero and fast velocities, the rate parameter which controls the rate of frictional change with the velocity, and the radius of curvature are defined.

Some trilinear hysteretic models account for a higher degree of nonlinearity in the isolators (Furukawa et al., 2005; Markou & Manolis, 2016). Furthermore, additional models for triple friction pendulum bearings are also present (Fenz & Constantinou, 2008). However, these models are not a concern of this study.

## 2.2 Effect of Isolator Model on the Response

Studies mentioned in this section have shown that different analytical hysteretic models of isolators may yield significant deviations in seismic response. Isolator models, having sharper edges between stiffness transitions, tend to show higher superstructural response. On the other hand, more accurate hysteretic and structural responses could be achieved using smoothed or highly nonlinear models, which are relatively more complex to implement in structural analysis.

Mavronicola and Komodromos (2014) conducted a series of analysis using 18 pulse-like ground motions to compare sharp and smoothed (Bouc-Wen) bilinear models for LRB isolators. Several cases were investigated in the parametric study; different normalized characteristic strength, yield displacement of isolator, isolation period, earthquake ground motion, and the number of stories (three and five stories). The results showed that the maximum isolator relative displacements could be overestimated or underestimated with the sharp bilinear model. Average displacements do not significantly change with the isolation system characteristics but were mostly influenced by the earthquake characteristics. However, seismic response accelerations seem to be slightly increased when the sharp bilinear model was used instead of a more accurate and smoothed model. which was attributed to the contribution of higher modes and the abrupt change in the isolator stiffness. It was also stated that the ratio of the characteristic (yield) strength to the seismic weight on the isolator has considerable effects on the isolation system's behavior and the superstructure.

In a Ph.D. dissertation thesis (Mavronicola, 2017), the discrepancies of the response of sharply bilinear and smoothed bilinear models were investigated. 2-D analyses of 3 and 5 story base-isolated buildings with LRB were conducted under 50 pulse-like ground motions. It was found that when the sharp bilinear model is used, computed maximum floor acceleration and story drifts are overestimated. The deviation was more significant when the isolation system has higher normalized characteristic strength values. The displacement response for both models was comparable, and sharp bilinear models can be used with confidence if appropriate safety factors are included.

A commentary in ASCE7-16 (Chapter C17, C17.5.5) states that sharp bilinear systems were observed to have higher floor accelerations and superstructural forces. Therefore, it recommended a higher vertical force distribution factor in Equivalent Lateral Force Procedure (ELFP) for the systems with sharper bilinear hysteresis, basically for FPS. However, these findings were insufficiently developed to include in the design guidelines.

Several hysteretic models were developed and compared with the experimental results of triple friction pendulum isolators in Ray et al. (2013). The hysteresis response of the isolator showed better agreement with test results when the stiffness transition regions were modeled in a smoother manner, despite the fact that sharp edges also showed acceptable compliance but were more susceptible to numerical problems during the sudden stiffness transitions.

## 2.3 Tensile Behavior of Isolators

High rise structures, having shear walls, irregularities, and higher structural aspect (height/width) ratio, may induce significant tensile (uplift) forces, especially on corner isolators during a seismic action. Therefore, it is essential to comprehend the tensile behavior and the capacity of the isolators during an earthquake event.

A parametric study was conducted on a four-story base-isolated steel building with asymmetry and different isolators, vibration periods, damping ratio under various ground motions, with and without vertical earthquake components (Koshnudian & Motamendi, 2013). The study highlighted the importance of including the vertical component of the earthquake in the analysis as overturning moments, beam shear forces, corner column axial loads, and local uplifts could be significantly affected, especially for structures with a high aspect ratio. On the other hand, it was shown that the vertical component has negligible influence on system isolator hysteretic response. Furthermore, several dynamic shake table test specimens with high aspect ratio and having strong ground motion (Feng et al., 2004; Takaoka et al., 2011; Masaki et al., 2000) show that although the isolation system was stable, isolators are prone to tensile forces for buildings with such characteristics.

Novel research was conducted in Japanese literature on tensile behavior and capacity of all rubber isolators during displaced positions (Kani et al., 1999; Iwabe et al., 1999; Takayama et al., 1999). Moreover, a nonlinear tensile stiffness model and deformation behavior were investigated by the test results up to 250% shear strain in Yang et al. (2010). It is also mentioned that maximum tensile shear strains from 17% up to 42% were observed in experimental studies for structures with different characteristics. To avoid excessive tensile deformations and damage in the isolator, the tensile strain was restricted to 5% of total rubber height in Japanese literature and more than 1 MPa of tensile stress is not allowed in the Chinese design code.

An experimental study (Erkakan, 2014) was conducted on the isolation performance of circular rubber bearings with different sizes and loading protocols during horizontal deformation. The isolators were subjected to tensile stresses up to 2 MPa and shear strain up to 100% without significant degradation in hysteretic parameters. Also, it is mentioned that in the literature (Mano & Mangerig, 2018)., isolator limit tensile stress value is often taken as $2G_v$ (where $G_v$ is the shear modulus of rubber) and after this limit, the tensile stiffness of rubber isolators drops significantly due to the cavitation damage.

If uplift in rubber bearings cannot be avoided, some bilinear or multi spring models could be used to reflect the axial behavior accurately into the analytical model (Warn & Ryan, 2012). In practice, the axial force-deformation relationship is often taken as bilinear elastic, multiplying the compression stiffness by a reduction factor in order to calculate tensile stiffness. In Pietra and Park (2017), 190 full-scale tests were conducted on different isolator diameter and lead plug sizes. It was seen that when working under $3G_v$ tensile stresses, the tensile post-yield stiffness degradation during the cycles was not significant. It is also stated that lower bound cavitation occurred when 10-12% tensile strains were reached, and acceptable cavitation limit loads were specified between $2G_v$-$3G_v$. Finally, the ratio of tensile stiffness to the compressive stiffness was found to vary between 1/10 (for isolator of small diameter) to 1/80 (large diameter).

International design codes have different requirements about the uplift behavior in rubber bearings. In ASCE7-16 (2016), local uplift of elements might be allowed if the resulting deflections will not result in overstress or instability of the isolator. In EN15129 (2009), it is mentioned that a tensile stresses up to $2G_v$ can be bearable without significant cavitation; otherwise, uplift restraining connections are recommended. California Department of Transportation (Caltrans, 2010) does not allow uplift. Finally, TBDY2019 and AASHTO LRFD (2010) recommends tie-down or anchorage systems to eliminate the uplift effect.

Conventional sliding isolators have no tensile carrying capability, and a gap is generated between the upper and lower plates when the tensile load exceeds the weight on the isolator during an earthquake due to the high vertical accelerations or overturning. Therefore, no frictional restoring force is generated when the isolator is in uplift condition. Similarly, very high compressive forces are also generated during a seismic event, followed by the uplift, resulting in excessively high shear restoring forces due to the friction action. Moreover, following the uplift of isolators, an impact could happen between the sliding materials, which could significantly damage sliding surfaces and the isolator and hysteretic behavior.

Although, so far, no reported real earthquake case of sliding isolator failure due to uplift has been documented (Calvi & Calvi, 2018). several studies aim to observe uplift behavior on sliding pendulum isolators understructures with high aspect ratio and significant overturning.

Morgan (2007) conducted shaking table tests on quarter scale base-isolated steel braced frame. The study highlighted the importance of variation of axial loads due to overturning, and the aspect ratio (approximately 3:1) of the structure was selected large enough to create uplift under selected ground motions. The stability of the isolators was preserved after the tests where local uplift motions (not exceeding 0.25 seconds of disconnection of the plates) were observed. However, the isolators' significant variations in axial forces were attained, diverging from a bilinear hysteretic shape. These test results are compatible with Fenz's (2008) findings in which double and triple friction pendulum isolators were dynamically tested to facilitate practical implementation. In the study, approximately a magnitude of 2-3 mm of uplift displacements were observed for two cases; by the overturning and rocking (isolator hitting the displacement restrainer) motions. For both cases, instantaneous uplift behavior was observed, and upon contact of sliding surfaces, isolators normally continued to their hysteretic motion without any problem. If such a motion is observed, uplift magnitudes should be carefully assessed to prevent the slider from toppling over the isolator and become unstable or resulting in structural damage.

Uplift restrained devices were proposed and studied in many cases for the situations where uplift demands are unbearable or unwanted for sliding isolators (Roussis & Constantinou, 2006; Roussis, 2009; Kasalanati & Constantinou, 2005) and for rubber isolators (Griffith et al., 1990). However, these systems are not investigated in the concept of this thesis.

# CHAPTER 2

# ANALYTICAL MODEL

## 3.1 Building Model Information

The building is one of the 10-story T-shaped blocks of a base-isolated reinforced concrete (RC) hospital which was built in a high seismic zone in Turkey. The structural system consists mostly of column and beam (frame) elements and shear walls supporting the core (elevators and stairs) regions to limit the lateral displacements on the superstructure. The plan geometry is 115 m in the X direction and 75 m in the orthogonal Y direction, and the total height is 40.9 m.

The pedestal sizes are 1250x1250 mm below the isolation layer. The column dimensions are mostly 900x900 mm for the first floor and 800x800 mm for the upper floors. Moreover, beam dimensions of 800x600 mm were used throughout the structure. In addition, a limited number of columns and beams of different sizes were also used in the structural system. The shear wall thickness is 300 mm everywhere. Section rigidities of all members were modified by recommended values in Table 13.1 in TBDY2019 to account for cracking during the earthquake.

A 3-D structural model was created and analyzed using the commercial structural analysis program ETABS (v18.1.1) (Figure 3.1. ), and the isolation layout is given in Figure 3.2.

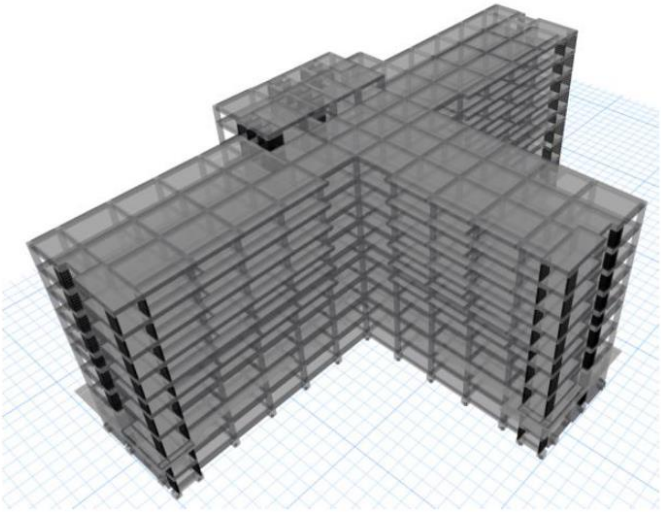

Figure 3.1. 3-D view of building model

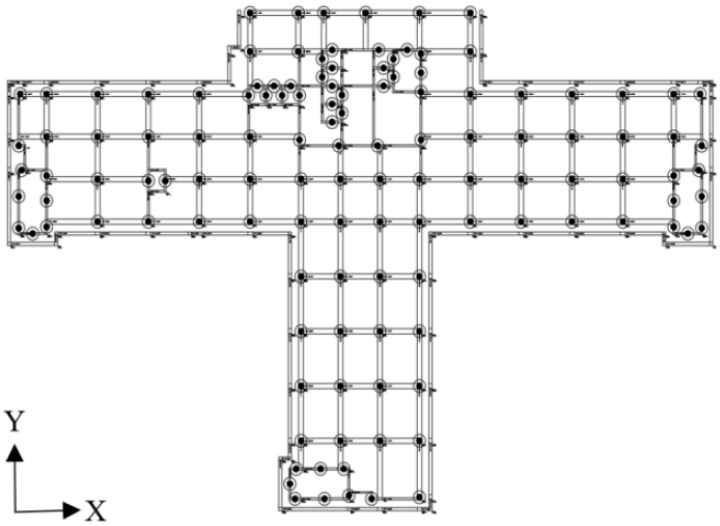


Figure 3.2. Isolator plan layout

In addition to the self-weight of the reinforced-concrete structure, a uniform load of 3.92 kN/m$^2$ of dead load (G) and 3.5 kN/m$^2$ of live load (Q) were used throughout the structure and on the top floor, 1 kN/ m$^2$ of snow load, which was also included as a live load, was used. The floor masses and the seismic mass of the structure from the G+0.3Q loading condition are shown in Table 3.1. The first ten periods and total mass participation ratios of the fixed base structure are given in Table 3.2. The first mode period is 19 s, and coupling of the X and Y directions is observed.

Table 3.1 Story and structural masses

| **Story** | ***Mass*** |
|---|---|
| Floor 10 | 664 |
| Floor 9 | 5307 |
| Floor 8 | 4861 |
| Floor 7 | 4862 |
| Floor 6 | 4862 |
| Floor 5 | 4803 |
| Floor 4 | 4986 |
| Floor 3 | 4909 |
| Floor 2 | 5175 |
| Floor 1 | 5374 |
| Isolation | 5142 |
| Floor -1 | 1070 |
| Tot. Str. Mass | 52015 |

Table 3.2 Modes of fixed base structure

| **Mode** | ***Period*** | $M_x$ | $M_y$ |
|---|---|---|---|
| 1 | 1.912 | 0.4480 | 0.1148 |
| 2 | 1.860 | 0.1003 | 0.5920 |
| 3 | 1.693 | 0.1481 | 0.0019 |
| 4 | 0.559 | 0.0339 | 0.0320 |
| 5 | 0.547 | 0.0265 | 0.0475 |
| 6 | 0.490 | 0.0260 | 0.0003 |
| 7 | 0.285 | 0.0089 | 0.0317 |
| 8 | 0.278 | 0.0201 | 0.0158 |
| 9 | 0.254 | 0.0003 | 0.0000 |
| 10 | 0.237 | 0.0207 | 0.0001 |

## 3.2 Seismicity and Selected Ground Motions

The building is located in a high seismic region in Turkey. The shear wave velocity at 30 m depth of the soil, $Vs_{30}$, was retrieved as 350 m/s. It corresponds to ZD soil class in TBDY2019. MCE and DBE level elastic spectra were obtained from Interactive Seismic Hazard Map (AFAD, Ministry of Interior of Turkey). In order to conduct nonlinear time history analysis, eleven ground motions were selected from PEER NGA-West2 Ground Motion Database (Pacific Earthquake Engineering Research Center, University of California). The selected ground motions are scaled so that the average accelerations of the ground motion spectra will not be less than 1.3 times the response spectra. The characteristics of the ground motions and their scale factors for MCE and DBE are shown in Table 3.3. Comparison of acceleration spectrum of each ground motion with the target spectra in Figure 3.3 and Figure 3.4 for MCE and DBE level seismic condition.

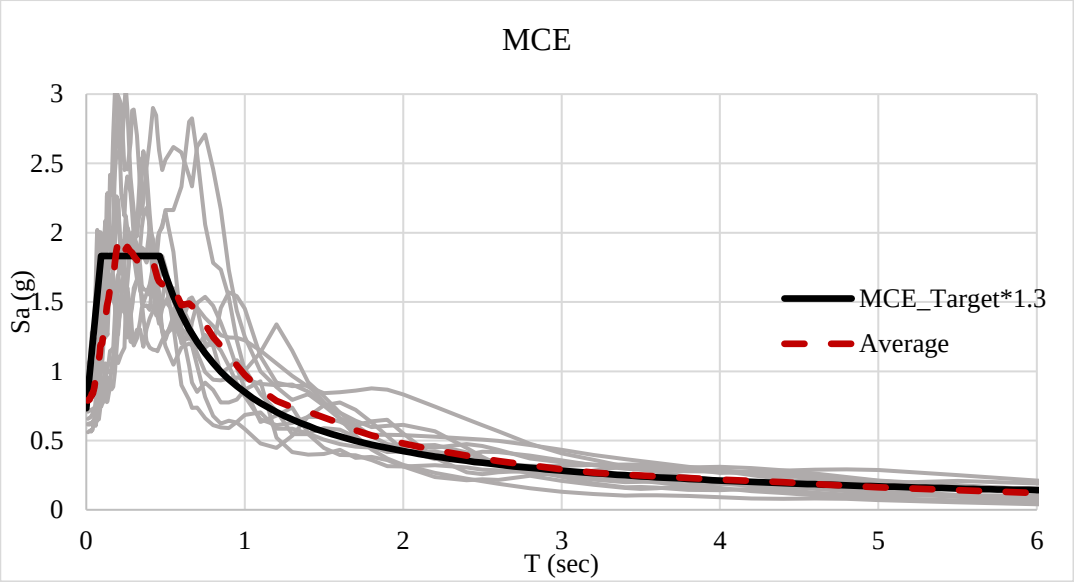


Figure 3.3. Target spectra and averaged spectra of eleven ground motions for MCE

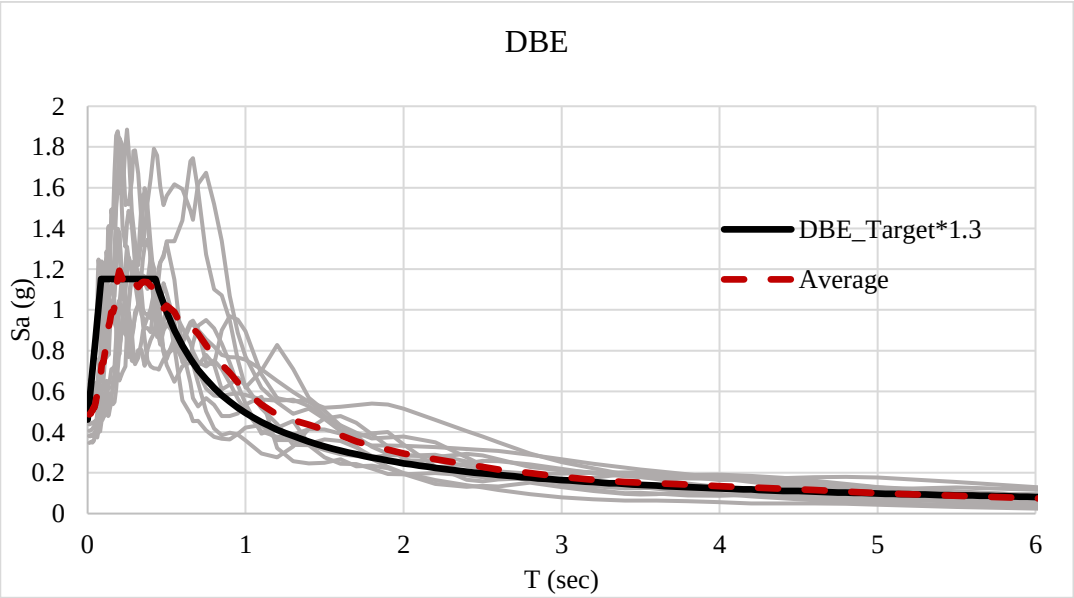


Figure 3.4. Target spectra and averaged spectra of eleven ground motions for DBE

Table 3.3 Eleven ground motions and scale factors for MCE and DBE

| Result ID | Record Seq. # | Tp-Pulse | Event | Year | Station | Magnitude | Mechanism | Vs30 (m/s) | MCE_SF | DBE_SF |
|---|---|---|---|---|---|---|---|---|---|---|
| 1 | 187 | - | "Imperial Valley-06" | 1979 | "Parachute Test Site" | 6.53 | strike slip | 348.7 | 3.892 | 2.404 |
| 2 | 316 | 4.389 | "Westmorland" | 1981 | "Parachute Test Site" | 5.9 | strike slip | 348.7 | 2.030 | 1.254 |
| 3 | 549 | - | "Chalfant Valley-02" | 1986 | "Bishop - LADWP South St" | 6.19 | strike slip | 303.5 | 2.826 | 1.746 |
| 4 | 558 | - | "Chalfant Valley-02" | 1986 | "Zack Brothers Ranch" | 6.19 | strike slip | 316.2 | 1.724 | 1.065 |
| 5 | 821 | - | "Erzican_ Turkey" | 1992 | "Erzincan" | 6.69 | strike slip | 352.1 | 1.125 | 0.695 |
| 6 | 850 | - | "Landers" | 1992 | "Desert Hot Springs" | 7.28 | strike slip | 359 | 3.530 | 2.180 |
| 7 | 1116 | - | "Kobe_ Japan" | 1995 | "Shin-Osaka" | 6.9 | strike slip | 256 | 2.487 | 1.536 |
| 8 | 1158 | - | "Kocaeli_ Turkey" | 1999 | "Duzce" | 7.51 | strike slip | 281.9 | 1.281 | 0.791 |
| 9 | 1605 | - | "Duzce_ Turkey" | 1999 | "Duzce" | 7.14 | strike slip | 281.9 | 0.947 | 0.585 |
| 10 | 2752 | - | "Chi-Chi_ Taiwan-04" | 1999 | "CHY101" | 6.2 | strike slip | 258.9 | 2.814 | 1.738 |
| 11 | 6893 | - | "Darfield_ New Zealand" | 2010 | "DFHS" | 7 | strike slip | 344 | 1.517 | 0.937 |

An illustration of orthogonal lateral components of unscaled ground motions are shown in Figure 3.5. Moreover, the unscaled ground motions with details and vertical components are given in Appendix A.

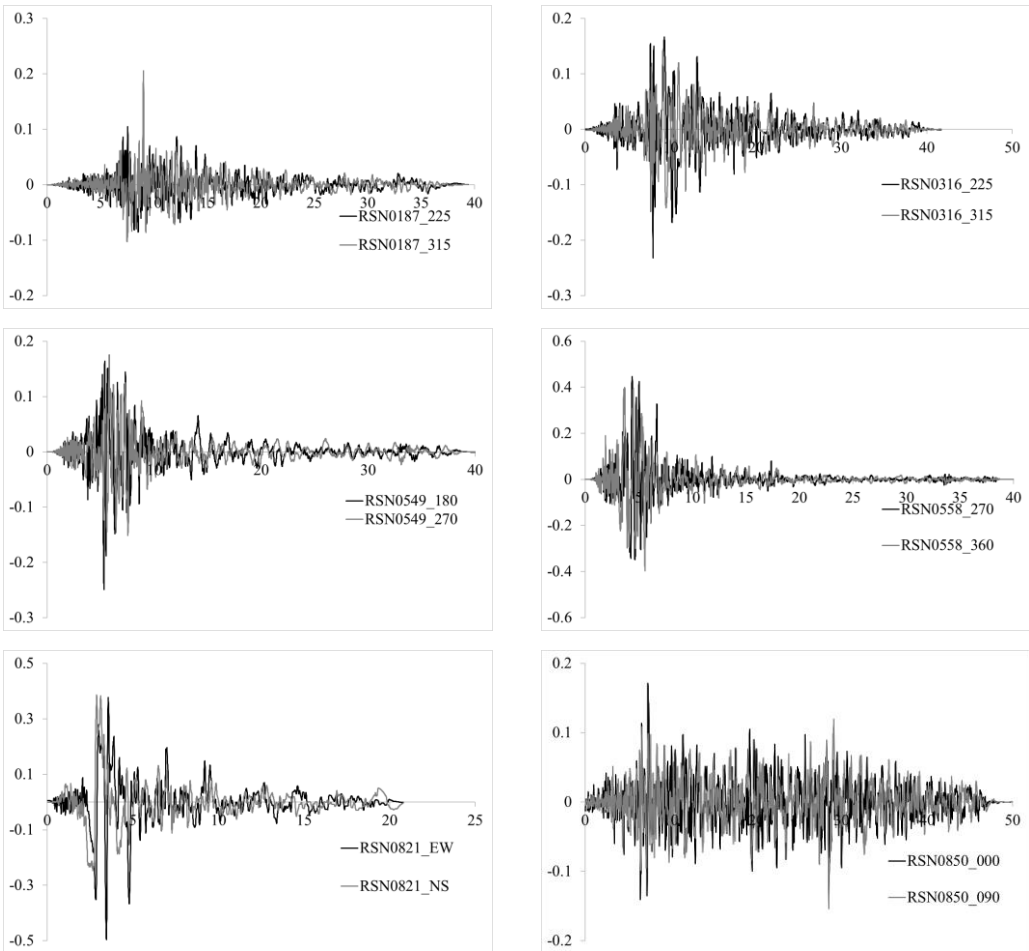

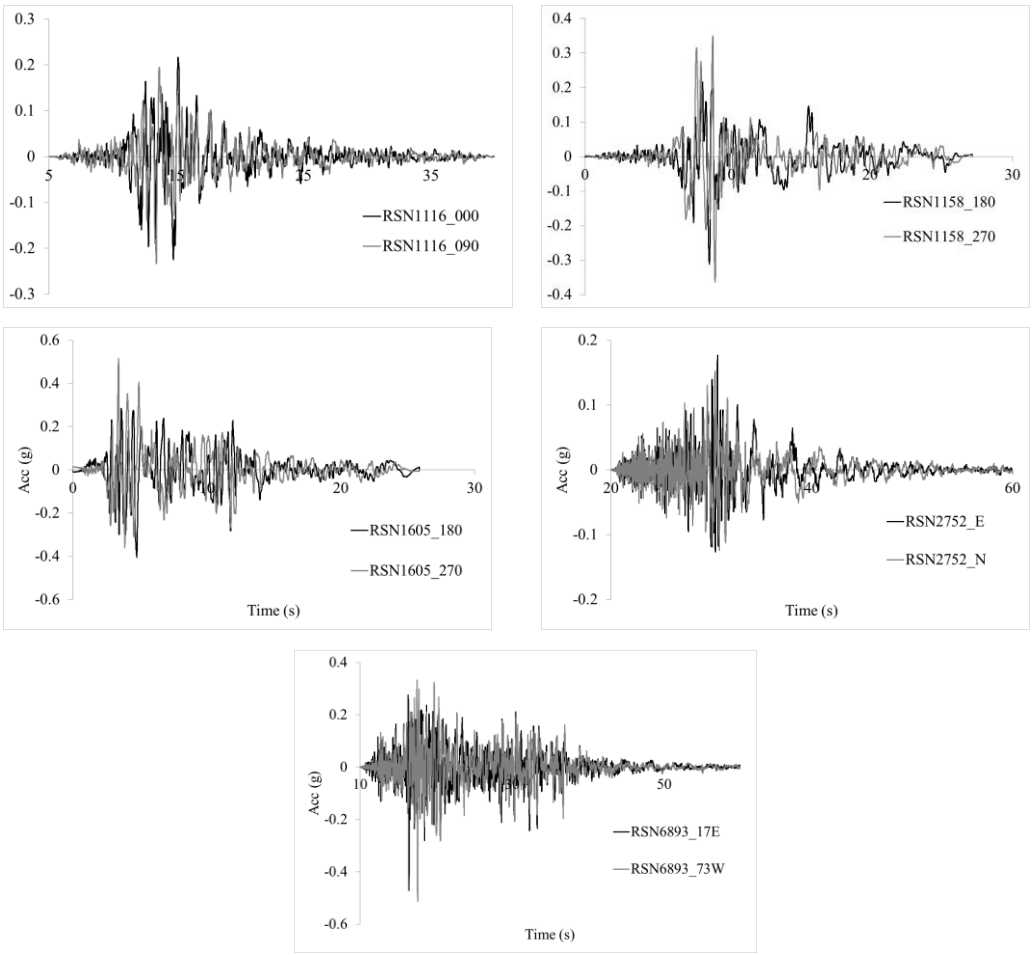


Figure 3.5. Unscaled horizontal components of 11 ground motions

## 3.3 Isolator Design and Nonlinear Models

High damping rubber bearing and friction pendulum system type isolators were designed for the structure to evaluate the rubber isolator performance. To assess the effect of the analytical models for FPS and HDRB, various isolator models used by researchers and designers were selected. First, the nonlinear time history analysis was conducted using more advanced types, called Friction Pendulum Isolator (FPI) and Deformation History Integral Type (DHI), respectively. Then, less accurate bilinear models called smoothed Bouc-Wen Model (BW) and sharp bilinear model (BL) were adopted for structural analyses.

TBDY2019 was used as the foremost guidelines during the design. Isolators to be designed based on three load combinatioıns given below:

$$1.4G + 1.6Q \tag{3.1}$$

$$1.2G + Q \pm E \tag{3.2}$$

$$0.9G \pm E \tag{3.3}$$

Where $G$ is the dead load, $Q$ is the live load, and $E$ is the effect of the earthquake, by considering the combination of three ground motion components. In this case, the earthquake loads were obtained by the average results of 11 ground motions from nonlinear time history analyses. Several types for FPS and HDRB were constructed according to their maximum compressive and tensile loads. The upper and lower bound isolator properties recommended by the manufacturer were used. Design criteria and stability checks in TBDY2019 (Section 14) were satisfied.

A preliminary design for the isolation system was conducted using Equivalent Lateral Force Procedure (ELFP) according to TBDY2019. The displacement at an earthquake level can be calculated by Eq (3.4). The subscript "$M$" stands for the MCE (DD-1) level earthquake, and thus, the equation could also be used for DBE (DD-2) level earthquake by substituting the corresponding parameters.

$$D_M = 1.3\left(\frac{g}{4\pi^2}\right) T_M^2 \eta_M S_{ae}^{MCE}(T_M) \tag{3.4}$$

Where, $S_{ae}^{MCE}(T_M)$ is the spectral acceleration for the corresponding effective period, $T_M$ is the effective period of the structure and $\eta_M$ is the damping scale factor and $\xi$ is the damping ratio for the corresponding maximum displacement and calculated by Eq (3.5) and Eq (3.6), respectively.

$$T_M = 2\pi\sqrt{\frac{W}{gK_M}} \tag{3.5}$$

$$\eta_M = \sqrt{\frac{10}{5+\xi}} \tag{3.6}$$

Evaluation of the damping ratio ($\xi$) often requires the target displacement of the isolator. Therefore, since Eq (3.4) becomes an implicit equation, a step by step iteration procedure was conducted by assuming an initial effective period and damping ratio for each isolator type.

The maximum displacements should be increased, as shown in Eq (3.7), because of the torsional movement of the isolation system. The movement, including torsion ($D_{TM}$) shall not be less than the $1.1D_M$.

$$D_{TM} = D_M\left[1 + y\frac{12e}{b^2+d^2}\right] \geq 1.1D_M \tag{3.7}$$

Where $e$ is the distance between the center of mass and the center of stiffness of the isolation system, b and d are the two most extended dimensions of the structure.

The forces transferred to the superstructure can be calculated by Eq (3.8),

$$V_M = \frac{S_{ae}^{MCE}(T_M)W\eta_M}{R} \tag{3.8}$$

Where $W$ is the structural weight (G+0.3Q), and $R$ is the structural behavior factor (taken as equal to one) affecting the ductility demand on the superstructure. More realistic structural forces can also be obtained by using the ELFP in ASCE7-16, which removes the weight of the isolation slab from the superstructure and can redistribute the lateral forces to the superstructure. In the end, higher superstructural forces were obtained when ASCE7-16 is used.

### 3.3.1 Design of High Damping Rubber Bearings

The preliminary isolation system design, having a target period of 3 s and damping ratio of 20%, was conducted according to the equivalent lateral force procedure (ELFP) (TBDY2019 Section14.14.2 ). The lower and upper bounds were taken as 0.9 and 1.45 respectively, recommended by Bridgestone and applied in the analysis according to TBDY2019 (Section 14.12). The summary table for the ELFP using both MCE and DBE level earthquakes with nominal, upper, and lower bound properties is shown in Table 3.4. The isolation system yielded 416 mm maximum displacement in MCE level ground motion with LB properties. Also, the forces, 11.4% and 12.4% of seismic weight, are transferred to the superstructure in DBE UB properties in TBDY2019 and ASCE7-16.

Table 3.4 Equivalent lateral force procedure for HDRB

| **Analysis Type** | | *MCE-LB* | *MCE-Nom* | *MCE-UB* | *DBE-LB* | *DBE-Nom* | *DBE-UB* |
|---|---|---|---|---|---|---|---|
| **Seismic Weight (kN)** | $W$ | | | 499727 | | | |
| **Effective Period (s)** | $T_M$ | 2.942 | 2.765 | 2.208 | 2.510 | 2.326 | 1.774 |
| **Damping Ratio %** | $\xi$ | 22% | 22% | 23% | 24% | 24% | 24% |
| **Total Effective Stiffness (kN/m)** | $K_M$ | 232429 | 263189 | 412514 | 319363 | 371929 | 639180 |
| **Damping Scale Factor** | $\eta_M$ | 0.610 | 0.606 | 0.594 | 0.587 | 0.587 | 0.535 |
| **Spectral Acc. (g)** | $S_{ae}(T_M$ | 0.222 | 0.236 | 0.295 | 0.151 | 0.163 | 0.214 |
| **Max. Displ. (m)** | $D_M$ | 0.378 | 0.353 | 0.276 | 0.181 | 0.167 | 0.116 |
| **Max. Disp. w/ Torsion (m)** | $D_{TM}$ | **0.416** | 0.388 | 0.304 | 0.199 | 0.184 | 0.128 |
| **TBDY2019 Base Shear ($V_m$/W)** | | 0.135 | 0.143 | 0.175 | 0.089 | 0.096 | **0.114** |
| **ASCE7-16 Base Shear ($V_m$/W)** | | 0.143 | 0.152 | 0.186 | 0.095 | 0.102 | **0.124** |

In a collaborative research project with Bridgestone Corporation (Japan), four types of HDRB (Bridgestone Seismic Isolation Product Line-up, 2017) were selected for the building. According to their maximum earthquake compressive loads (Eq (3.1)), the isolators were grouped into four categories. The tensile capacity recommended by Bridgestone and other papers (Mano & Mangerig, 2018; EN15129, 2009, Pietra & Park, 2017), 1 MPa was adopted. Isolators that exceeded the tensile capacity were moved into the greater size to reduce the stresses.

The design was conducted based on an isolation system having a maximum of 200% shear strain displacements, dictated by TBDY2019, under maximum earthquake level (MCE); despite the fact that it was observed HDRB isolators could undergo higher strain limits up to 300% shear strains without any significant deterioration in hysteresis loops (Kikuchi & Aiken, 1997; Masaki et al., 2017). Therefore, isolator total rubber height is selected as 200 mm, which corresponds nearly 210% shear strain. The code limitation is exceeded by a little in this situation. However, HDRB has a increasing nonlinear stiffness at shear strains higher than 200-250%, and hysteresis loops of some ground motions with higher shear strains can now be observable.

It should be noted that the periods DBE-UB and DBE-Nom conditions are close to the fixed base structure period. Therefore, relatively higher superstructural response might be expected when the evaluation is conducted.

A table including HDRB properties and design loads is presented in Table 3.5. The vertical compression stiffnesses of the isolators were calculated according to TBDY2019 (Appendix 14A).

Table 3.5 HDRB isolator design loads and properties

| | | Type 1 | Type 2 | Type 3 | Type 4 |
|---|---|---|---|---|---|
| **# of isolator** | **#** | **57** | **36** | **25** | **17** |
| **Average Seismic Weight (kN)** | **G+0.3Qave** | 1649 | 4036 | 6099 | 6352 |
| **Maximum Static Load (kN)** | **1.4G+1.6Qmax** | 6646 | 9777 | 12024 | 12362 |
| **Maximum Earthquake Load (kN)** | **1.2G+Q+Emax** | 9000 | 12000 | 15000 | 17174 |
| **Minimum Eathquake Load (Tension) (kN)** | **0.9-Emax** | 580 | 737 | 915 | 958 |
| **Shear Modulus (kPa)** | **Gv** | 620 | 620 | 620 | 620 |
| **Elastic Modulus (4*Gv) (kPa)** | **E0** | 2480 | 2480 | 2480 | 2480 |
| **Coefficient on Hardness** | **k** | 0.6 | 0.6 | 0.6 | 0.6 |
| **Comp. Modulus (kPa)** | **Ec** | 4003547 | 3702695 | 3711696 | 3812646 |
| **Bulk Modulus (kPa)** | **K** | 2000000 | 2000000 | 2000000 | 2000000 |
| **Vertical Rigidity Modulus (kPa)** | **Ev** | 1333727 | 1298577 | 1299683 | 1311845 |
| **Vertical Rigidity (kN/m)** | **Kv** | 4283139 | 5058781 | 6166376 | 7402727 |
| **Outer Diameter (m)** | **Do (B)** | 0.9 | 1 | 1.1 | 1.2 |
| **Inner Diameter (m)** | **Di (BL)** | 0.02 | 0.055 | 0.055 | 0.055 |
| **Effective Area ($m^2$)** | **Ar** | 0.6359 | 0.7830 | 0.9480 | 1.1286 |

Table 3.5 (Cont'd) HDRB isolator design loads and properties

| | | | | | |
|---|---|---|---|---|---|
| **Inner Area ($m^2$)** | **Ai** | 0.000 | 0.002 | 0.002 | 0.002 |
| **Rubber layer thickness (m)** | **tr** | 0.006 | 0.0067 | 0.0074 | 0.008 |
| **Number of Layers** | **n** | 33 | 30 | 27 | 25 |
| **Tot. Rubber Height (m)** | **H** | 0.198 | 0.201 | 0.200 | 0.200 |
| **Tot. Iso. Height (m)** | **Ht** | 0.4108 | 0.4006 | 0.3902 | 0.3856 |
| **First Shape Factor** | **S1** | 36.7 | 35.3 | 35.3 | 35.8 |
| **Second Shape Factor** | **S2** | 4.55 | 4.98 | 5.51 | 6.00 |
| **Max. Rubber Elong.** | **εb** | 5 | 5 | 5 | 5 |
| **Design Rotation Angle (rad)** | **θs** | 0.005 | 0.005 | 0.005 | 0.005 |

Using the mechanical characteristics in Table 3.4. the bilinear shear properties were obtained by the equations of Bridgestone recommendation. (Bridgestone Product Isolation Line-up, 2017). It was seen that the results from the Bridgestone equations are compatible with the equations used in TBDY2019 for rubber isolators. The equivalent shear modulus $G_{eq}$, damping ratio $H_{eq}$, and a function of a ratio of characteristic strength to the maximum force $u$ should be calculated first to obtain equivalent stiffness $K_{eq}$, initial stiffness $K_1$, post-yield stiffness $K_2$, and characteristic (yield) strength stiffness $Q_d$. The expressions for these parameters are shown from Eq (3.9) to Eq (3.15).

$$G_{eq}(\gamma) = 0.620(0.1364\gamma^4 - 1.016\gamma^3 + 2.903\gamma^2 - 3.878\gamma + 2.855) \quad (3.9)$$

$$H_{eq}(\gamma) = 0.240x(0.02902\gamma^3 - 0.1804\gamma^2 + 0.2364\gamma + 0.9150) \quad (3.10)$$

$$u(\gamma) = 0.408x(0.03421\gamma^3 - 0.2083\gamma^2 + 0.2711\gamma + 0.9028 \quad (3.11)$$

$$K_{eq} = G_{eq}A_r/H \quad (3.12)$$

$$K_2 = K_{eq}(1 - u) \quad (3.13)$$

$$K_1 = 10xK_2 \quad (3.14)$$

$$Q_d = uK_{eq}H\,\gamma \quad (3.15)$$

The corresponding shear properties of isolators were determined from the equations above for nominal properties. The secondary rigidity and characteristic strength are multiplied by LB or UB factors when necessary. The lateral shear properties of four isolator types for MCE and DBE conditions are given from Table 3.6 to Table 3.11.

Table 3.6 Isolator bilinear properties for MCE-LB condition

| | **Type 1** | **Type 2** | **Type 3** | **Type 4** |
|---|---|---|---|---|
| **γ** | 1.469 | 1.447 | 1.455 | 1.454 |
| $\boldsymbol{D_m}$ **(m)** | 0.291 | 0.291 | 0.291 | 0.291 |
| $\boldsymbol{G_{eq}}$ **(kPa)** | 519 | 522 | 521 | 521 |
| $\boldsymbol{H_{eq}}$ **(ξ) %** | 0.232 | 0.232 | 0.232 | 0.232 |
| $\boldsymbol{u}$ | 0.392 | 0.393 | 0.392 | 0.392 |
| $\boldsymbol{K_{eq}}$ **(kN/m)** | 1500 | 1830 | 2224 | 2646 |
| $\boldsymbol{K_2}$ **(kN/m)** | 913 | 1111 | 1351 | 1607 |
| $\boldsymbol{K_1}$ **(kN/m)** | 8787 | 10659 | 12982 | 15440 |
| $\boldsymbol{Q_d}$ **(kN)** | 192.5 | 237.0 | 286.9 | 341.6 |
| $\boldsymbol{F_{max}}$ **(kN)** | 524.6 | 646.1 | 782.2 | 931.2 |

Table 3.7 Isolator bilinear properties for MCE-Nom condition

| | **Type 1** | **Type 2** | **Type 3** | **Type 4** |
|---|---|---|---|---|
| $\gamma$ | 1.370 | 1.349 | 1.357 | 1.356 |
| $D_m$ **(m)** | 0.271 | 0.271 | 0.271 | 0.271 |
| $G_{eq}$ **(kPa)** | 533 | 536 | 534 | 535 |
| $H_{eq}$ **(ξ) %** | 0.234 | 0.234 | 0.234 | 0.234 |
| $u$ | 0.396 | 0.397 | 0.397 | 0.397 |
| $K_{eq}$ **(kN/m)** | 1710 | 2087 | 2535 | 3017 |
| $K_2$ **(kN/m)** | 1032 | 1258 | 1529 | 1819 |
| $K_1$ **(kN/m)** | 10324 | 12580 | 15293 | 18195 |
| $Q_d$ **(kN)** | 183.8 | 224.7 | 272.8 | 324.7 |
| $F_{max}$ **(kN)** | 463.7 | 565.9 | 687.5 | 818.1 |

Table 3.8 Isolator bilinear properties for MCE-UB condition

| | **Type 1** | **Type 2** | **Type 3** | **Type 4** |
|---|---|---|---|---|
| $\gamma$ | 1.072 | 1.056 | 1.063 | 1.062 |
| $D_m$ **(m)** | 0.212 | 0.212 | 0.212 | 0.212 |
| $G_{eq}$ **(kPa)** | 597 | 601 | 600 | 600 |
| $H_{eq}$ **(ξ) %** | 0.239 | 0.239 | 0.239 | 0.239 |
| $u$ | 0.406 | 0.407 | 0.407 | 0.407 |
| $K_{eq}$ **(kN/m)** | 2778 | 3398 | 4124 | 4908 |
| $K_2$ **(kN/m)** | 1649 | 2015 | 2447 | 2912 |
| $K_1$ **(kN/m)** | 16489 | 20154 | 24472 | 29121 |
| $Q_d$ **(kN)** | 239.7 | 293.4 | 356.1 | 423.8 |
| $F_{max}$ **(kN)** | 589.8 | 721.3 | 875.6 | 1042.0 |

Table 3.9 Isolator bilinear properties for DBE-LB condition

| | **Type 1** | **Type 2** | **Type 3** | **Type 4** |
|---|---|---|---|---|
| **γ** | 0.702 | 0.692 | 0.696 | 0.695 |
| $\boldsymbol{D_m}$ **(m)** | 0.139 | 0.139 | 0.139 | 0.139 |
| $\boldsymbol{G_{eq}}$ **(kPa)** | 772 | 779 | 776 | 777 |
| $\boldsymbol{H_{eq}}$ **(ξ) %** | 0.241 | 0.240 | 0.240 | 0.240 |
| $\boldsymbol{u}$ | 0.409 | 0.409 | 0.409 | 0.409 |
| $\boldsymbol{K_{eq}}$ **(kN/m)** | 2231 | 2731 | 3314 | 3944 |
| $\boldsymbol{K_2}$ **(kN/m)** | 1318 | 1615 | 1959 | 2332 |
| $\boldsymbol{K_1}$ **(kN/m)** | 13184 | 16148 | 19592 | 23317 |
| $\boldsymbol{Q_d}$ **(kN)** | 126.8 | 155.2 | 188.4 | 224.2 |
| $\boldsymbol{F_{max}}$ **(kN)** | 310.1 | 379.7 | 460.7 | 548.3 |

Table 3.10 Isolator bilinear properties for DBE-Nom condition

| | **Type 1** | **Type 2** | **Type 3** | **Type 4** |
|---|---|---|---|---|
| **γ** | 0.651 | 0.641 | 0.645 | 0.644 |
| $\boldsymbol{D_m}$ **(m)** | 0.129 | 0.129 | 0.129 | 0.129 |
| $\boldsymbol{G_{eq}}$ **(kPa)** | 809 | 817 | 814 | 814 |
| $\boldsymbol{H_{eq}}$ **(ξ) %** | 0.240 | 0.240 | 0.240 | 0.240 |
| $\boldsymbol{u}$ | 0.408 | 0.408 | 0.408 | 0.408 |
| $\boldsymbol{K_{eq}}$ **(kN/m)** | 2599 | 3182 | 3861 | 4595 |
| $\boldsymbol{K_2}$ **(kN/m)** | 1538 | 1884 | 2286 | 2720 |
| $\boldsymbol{K_1}$ **(kN/m)** | 15382 | 18839 | 22857 | 27202 |
| $\boldsymbol{Q_d}$ **(kN)** | 136.7 | 167.3 | 203.0 | 241.6 |
| $\boldsymbol{F_{max}}$ **(kN)** | 334.8 | 409.9 | 497.4 | 592.0 |

Table 3.11 Isolator bilinear properties for DBE-UB condition

| | **Type 1** | **Type 2** | **Type 3** | **Type 4** |
|---|---|---|---|---|
| $\gamma$ | 0.497 | 0.489 | 0.492 | 0.492 |
| $D_m$ **(m)** | 0.098 | 0.098 | 0.098 | 0.098 |
| $G_{eq}$ **(kPa)** | 948 | 956 | 953 | 953 |
| $H_{eq}$ **(ξ) %** | 0.238 | 0.238 | 0.238 | 0.238 |
| $u$ | 0.404 | 0.404 | 0.404 | 0.404 |
| $K_{eq}$ **(kN/m)** | 4415 | 5399 | 6554 | 7800 |
| $K_2$ **(kN/m)** | 2631 | 3219 | 3907 | 4650 |
| $K_1$ **(kN/m)** | 26310 | 32192 | 39073 | 46499 |
| $Q_d$ **(kN)** | 175.3 | 214.3 | 260.2 | 309.7 |
| $F_{max}$ **(kN)** | 434.0 | 530.8 | 644.4 | 766.8 |

#### 3.3.1.1 Deformation History Integral Type (DHI) Model

One elastic spring and two hysteretic springs were included in the DHI model. The concept is shown in Figure 3.6. The resulting hysteresis is the sum of all hysteretic springs in the model. This model is shear strain-dependent, and the stress-strain mathematical expression is given in Eq (3.16).

The two horizontal directions are coupled; therefore, the DHI model can capture a highly nonlinear response under bilateral excitations. The horizontal stiffness significantly increases after 200% shear strain for HDRB, contributing to the total system damping. This behavior cannot be accurately captured in other bilinear models unless comprehensive modifications are made.

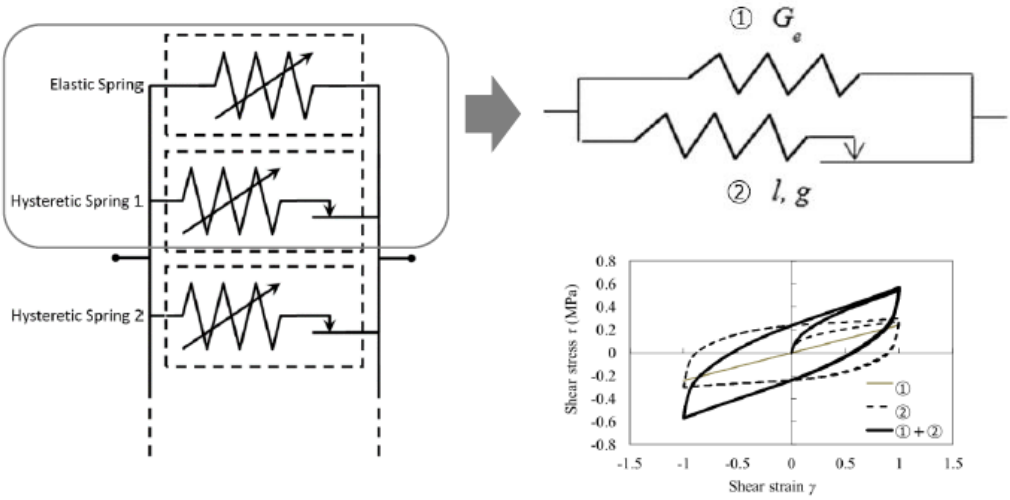


Figure 3.6. DHI model concept, elastic and hysteretic spring behavior (Eser et al. 2020)

$$\tau_x(\gamma_x,\gamma_y) = \Xi(t)G_e\gamma_x + \sum_i^n g_i \int_0^\Gamma e^{-(\Gamma-\Gamma')/l_i}\frac{d}{d\Gamma'}\left[\frac{1}{3}(\gamma_x'-\gamma_x)(\gamma_x'^2+\gamma_y'^2)+\gamma_x'\right]d\Gamma'$$

$$\tau_y(\gamma_x,\gamma_y) = \Xi(t)G_e\gamma_y + \sum_i^n g_i \int_0^\Gamma e^{-(\Gamma-\Gamma')/l_i}\frac{d}{d\Gamma'}\left[\frac{1}{3}(\gamma_y'-\gamma_y)(\gamma_x'^2+\gamma_y'^2)+\gamma_y'\right]d\Gamma' \qquad (3.16)$$

$$\Xi(t) = \theta + (1-\theta)\exp\left(-\frac{\gamma_m(t)}{\gamma_d}\right)$$

where,

$$\Gamma = \int_C \sqrt{d\gamma_x^2 + d\gamma_y^2}$$

$$\gamma_m(t) = \max_t\left[\sqrt{\gamma_x{}^2+\gamma_y{}^2}\right]$$

$\gamma_x, \gamma_y$ : shear strain in x, y direction

$\tau_x, \tau_y$ : shear stress in x, y direction

$\Gamma$ : curvilinear integral along the deformation orbit C on $\gamma_x$-$\gamma_y$ plane

$l_i, g_i, G_e, \theta, \gamma_d$ : material parameters

$\Xi(t)$ : damage function (degradation of stiffness by loading history)

Horizontal material hysteretic control parameters, recommended by Bridgestone are given in Table 3.12, and defined in ETABS in "High Damping Rubber Isolator" link property, separately for upper and lower bound analyses.

Please note that these parameters were constructed by using the test data and the "Added Elastic Stiffness, Ge" does not directly represents the the stiffness of the isolator but only have effect on the elastic term. Therefore the nominal value of Ge can be lower than the lower bound.

Table 3.12 Material input parameters for DHI model

| **Property** | **Nominal** | **UB** | **LB** |
|---|---|---|---|
| **Added Elastic Stiffness – $G_e$ (MPa)** | 0.5257 | 0.8136 | 0.5262 |
| **Control Strength 1 - $g_1$ (MPa)** | 2.468 | 3.364 | 1.999 |
| **Control Strength 2 - $g_2$ (MPa)** | 0.3564 | 0.4858 | 0.2887 |
| **Control Strain 1 - $l_1$** | 0.03591 | 0.03591 | 0.03591 |
| **Control Strain 2 - $l_2$** | 0.5 | 0.5 | 0.5 |
| **Resistance Ratio - $\theta$** | 0.4598 | 0.4598 | 0.4598 |
| **Damage Parameter – $\gamma_d$** | 0.4181 | 0.4181 | 0.4181 |

The axial behavior is only linear elastic in high damping rubber isolator link definition. Therefore, to account for different tensile and compressive behavior a Multilinear Elastic" link element (CSI Analysis Reference Manual, 2017), having only axial spring behavior definition, was also added in series to the horizontal springs. The tensile stiffness was taken as 1/30 times of the compression stiffness for all types (Pietra & Park, 2017). Axial force-displacement relationships for all four types are presented in Figure 3.7. If the axial displacements exceed the maximum displacement in the graph, a linear interpolation is applied in the model.

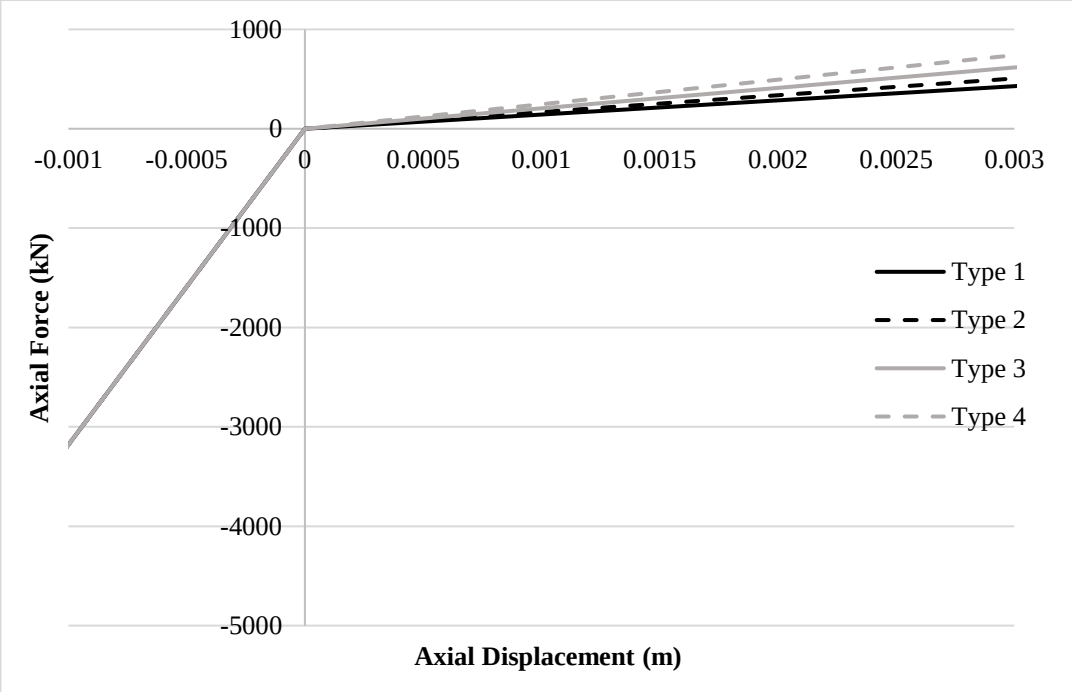


Figure 3.7. Axial force-displacement relationship of HDRB types

#### 3.3.1.2 Smoothed Bouc-Wen (BW) Model

In this model, biaxial excitation of isolation elements can be captured accurately. The axial and horizontal behaviors are uncoupled. The axial behavior is only linear elastic; therefore the same multilinear axial links were assigned as in the DHI model (Figure 3.7). For horizontal degrees of freedom, the biaxial diagram showing the plasticity model implemented in ETABS is shown in Figure 3.8. The nonlinear shear force-displacement behavior is governed by the relationships below for two directions ($d_{u2}$ and $d_{u3}$):

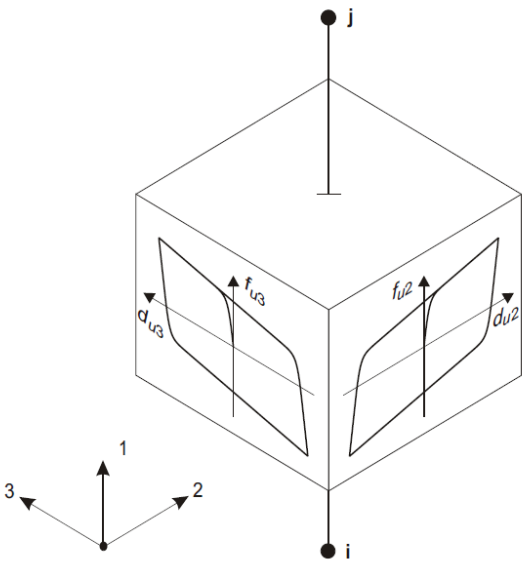


Figure 3.8. The isolator property definition for biaxial deformation (retrieved from CSI Analysis Reference Manual, 2017)

$$f_{u2} = ratio_2 k_2 d_{u2} + (1 - ratio_2) yield_2 z_2 \tag{3.17}$$

$$f_{u3} = ratio_3 k_3 d_{u3} + (1 - ratio_3) yield_3 z_3 \tag{3.18}$$

Where, $k_2$ and $k_3$ are the initial elastic stiffness, $ratio_2$ and $ratio_3$ are the ratio of post-yield stiffness to initial stiffness, $yield_2$ and $yield_3$ are the yield (characteristic) force of the isolator. $z_2$ and $z_3$are the internal hysteretic variables. The range of the variables are in the range of $\sqrt{z_2^2 + z_3^2} \leq 1$, outside of the yield region and $\sqrt{z_2^2 + z_3^2} = 1$, circular shape at the yield surface. The value of the hysteretic parameters are defined according to following implicit differential equations and having a zero value at initial conditions. The relation (Eq (3.19)) was constructed by using the dimensionless quantities that control the shape of the hysteresis in Park et al. (1986) with $A = 1$ and $\beta = \gamma = 0.5$.

$$\begin{Bmatrix} \dot{z_2} \\ \dot{z_3} \end{Bmatrix} = \begin{bmatrix} 1 - a_2 z_2^2 & -a_3 z_2 z_3 \\ -a_2 z_2 z_3 & 1 - a_3 z_3^2 \end{bmatrix} \begin{Bmatrix} \frac{k_2}{yield_2} \dot{d_{u2}} \\ \frac{k_3}{yield_3} \dot{d_{u3}} \end{Bmatrix} \tag{3.19}$$

Where,

$$a_2 = \begin{cases} 1 & if\ d_{u2} \dot{z_2} > 0 \\ 0 & otherwise \end{cases} \tag{3.20}$$

$$a_3 = \begin{cases} 1 & if\ d_{u3} \dot{z_3} > 0 \\ 0 & otherwise \end{cases} \tag{3.21}$$

According to Bridgestone recommendations, the bilinear hysteretic characteristics of HDRB isolators were calculated using mechanical isolator properties and presented in Table 3.6, Table 3.10 and Table 3.11. The rubber isolator input parameters were extracted from the bilinear shear properties of the isolators and are presented in Table 3.13 for MCE-LB, DBE-UB, and DBE-Nom analyses, that are used for structural response evaluation.

Table 3.13 Smoothed bilinear model input parameters

| | | **MCE-LB** | **DBE-Nom** | **DBE-UB** |
|---|---|---|---|---|
| **Type 1** | **keff2,3** | 1500 | 2599 | 4415 |
| | **k2,3** | 9127 | 15382 | 26310 |
| | **yield2,3** | 171 | 137 | 175 |
| | **ratio2,3** | 0.1 | | |
| **Type 2** | **keff2,3** | 1830 | 3182 | 5399 |
| | **k2,3** | 11110 | 18839 | 32192 |
| | **yield2,3** | 209 | 167 | 214 |
| | **ratio2,3** | 0.1 | | |
| **Type 3** | **keff2,3** | 2224 | 3861 | 6554 |
| | **k2,3** | 13512 | 22857 | 39073 |
| | **yield2,3** | 254 | 203 | 260 |
| | **ratio2,3** | 0.1 | | |
| **Type 4** | **keff2,3** | 2646 | 4595 | 7800 |
| | **k2,3** | 16075 | 27202 | 46499 |
| | **yield2,3** | 302 | 242 | 310 |
| | **ratio2,3** | 0.1 | | |

#### 3.3.1.3 Sharp Bilinear (BL) Model

In this model, all three degrees of freedom are uncoupled. The envelope curve of the nonlinear force-displacement relationship is directly the input parameter for axial and two shear deformations. This model is implemented in ETABS as the "Multilinear Plastic (MLP) Link" property, and the "Kinematic Hysteresis Model" was used as the energy dissipating mechanism. The concept of the model for each independent direction is shown in Figure 3.9.

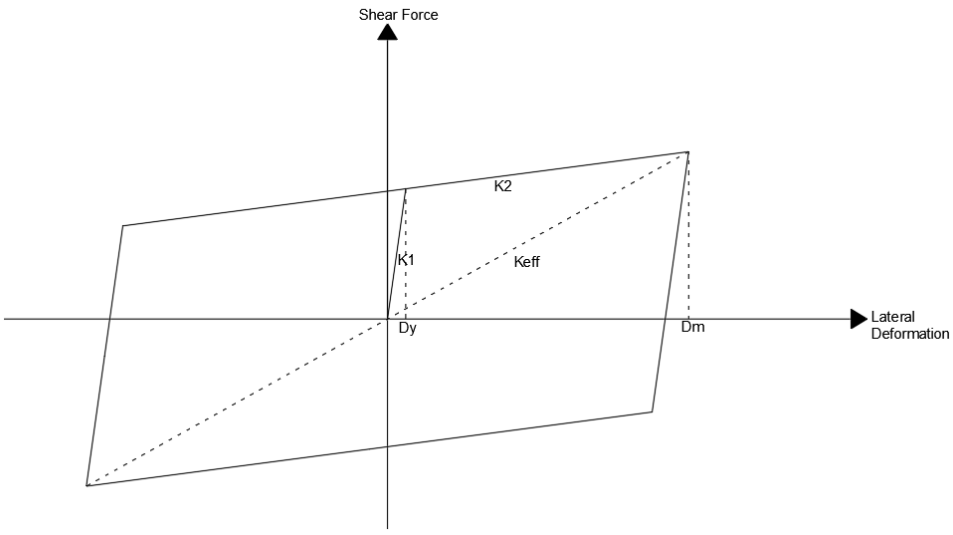


Figure 3.9. Sharp bilinear concept

The sharp bilinear characteristics were estimated from bilinear shear properties from Table 3.6, Table 3.10 and Table 3.11 and are shown in a graphical form from Figure 3.10 to Figure 3.12 for MCE-LB, DBE-Nom, and DBE-UB cases. The nonlinear axial behavior can be modeled similarly to the shear directions. Different compressive and tensile stiffnesses were assigned as in DHI model, Figure 3.7.

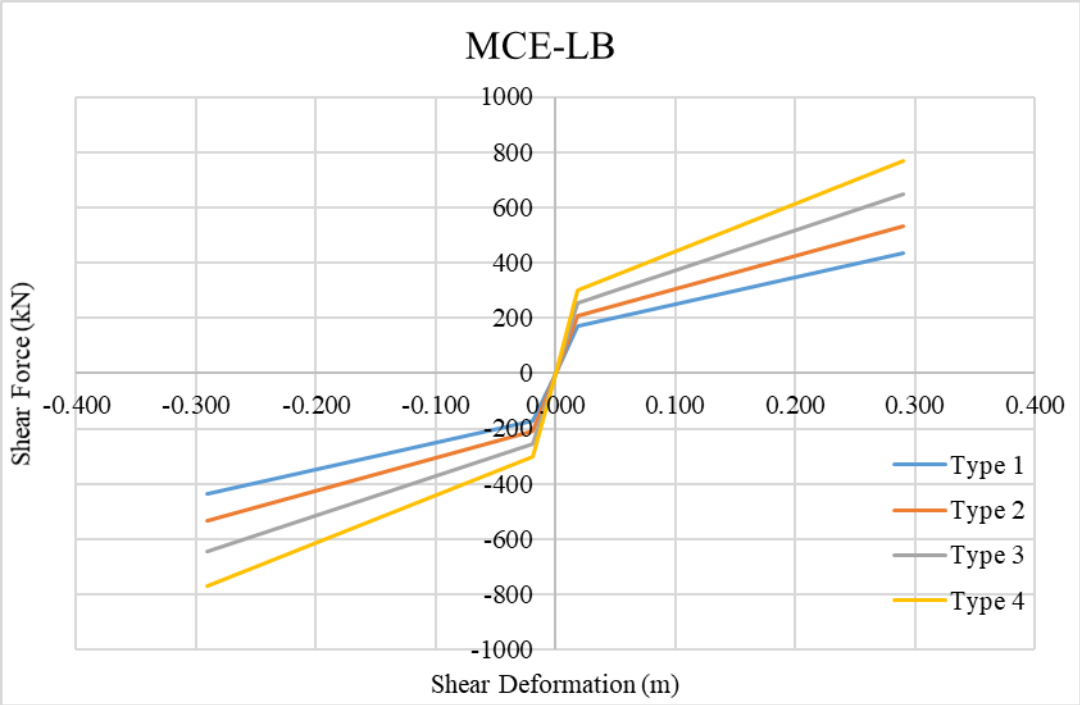


Figure 3.10. HDRB sharp bilinear envelope input for MCE-LB isolator properties

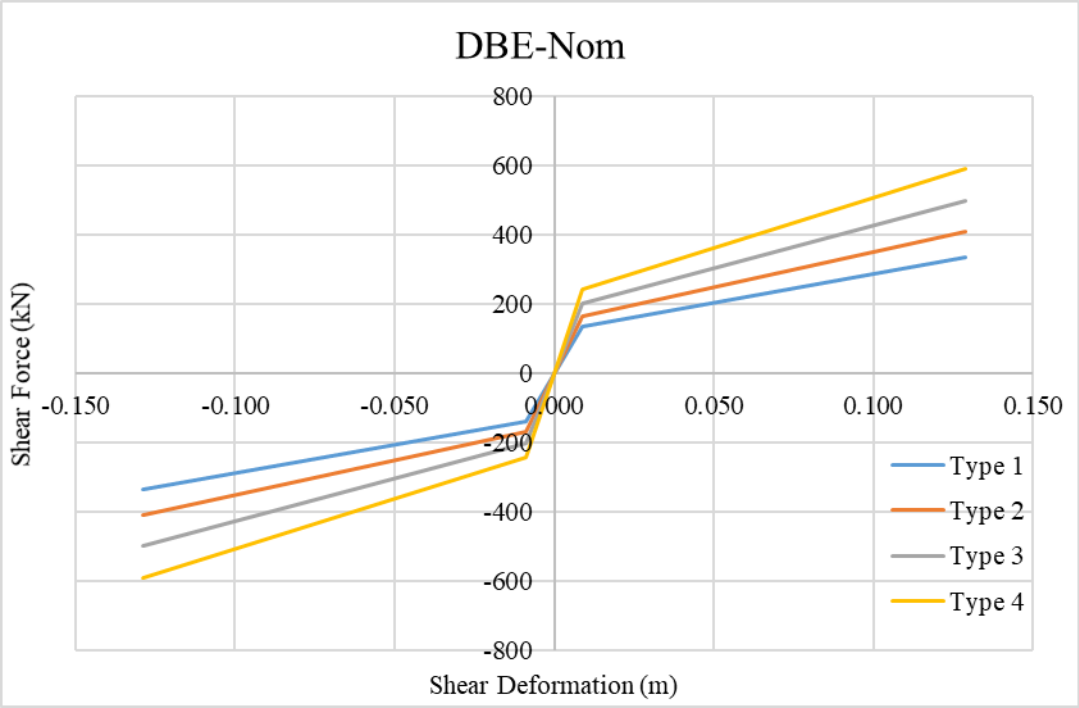


Figure 3.11. HDRB sharp bilinear envelope input for DBE-Nom isolator properties

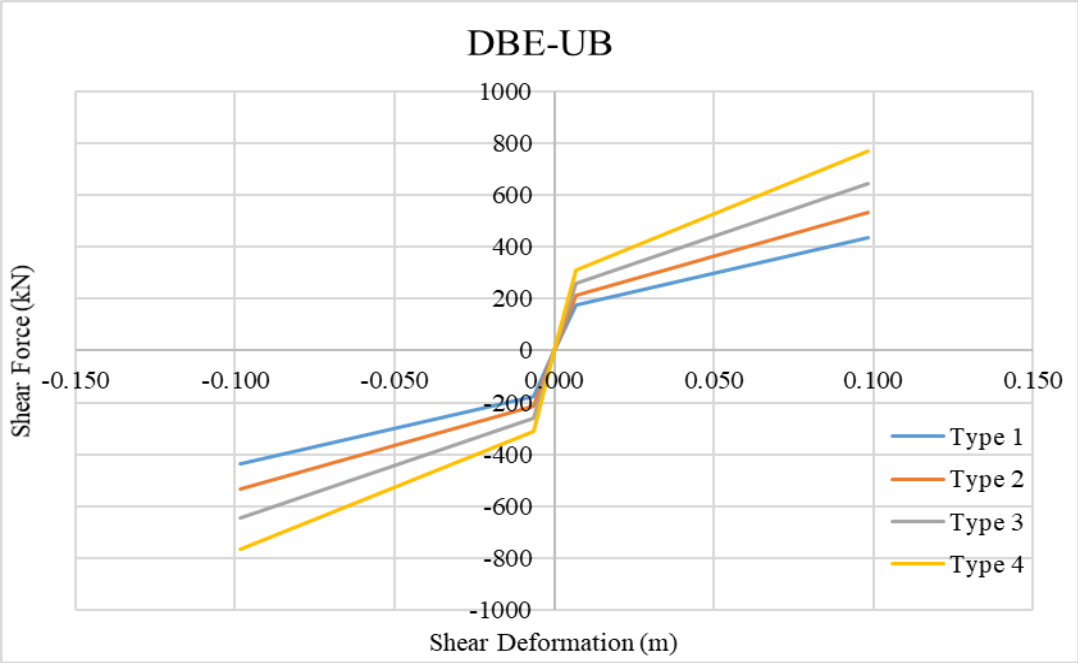


Figure 3.12. HDRB sharp bilinear envelope input for DBE-UB isolator properties

### 3.3.2 Design of Friction Pendulum System

Double curved surface frictional sliders may be used in the design of the building. The friction pendulum system consists of an articulated frictional disk that slides between concave plates. The damping is provided by the friction and the restoring stiffness is achieved by the curvature of the surfaces and the gravity. The friction is load-dependent and varies with the sliding velocity and temperature. During an earthquake, due to the variation of axial column loads, the restoring stiffness shows high nonlinearity, especially in locations with higher overturning moments and shear walls. In most cases, isolators located at the corner regions of buildings and shear walls exhibit uplift behavior due to the axial load variation. Since friction pendulum isolators do not have tensile carrying mechanisms, no frictional force is generated during the uplift.

The preliminary analysis with ELFP was conducted with a target period of 3.5 s and 20% damping in MCE level seismic input with lower bound isolator properties. Due to the variation in friction coefficient related to aging, testing and production

variation, the lower and upper bound parameters are taken as 0.9 and 1.56, respectively, and applied in the analysis according to TBDY2019 (Section 14.13). Maximum displacement with torsional effects was calculated as 0.502 m. The base shear forces were attained as 10.7% and 11.6% of superstructural weight for TBDY2019 and ASCE7-16, respectively. The summary table for ELFP analysis for all isolator properties is given in Table 3.14.

A friction pendulum system was designed according to TBDY2019 guidelines. Preliminarily, the isolators were grouped into three types depending on their maximum compressive loads. The nominal effective dynamic friction coefficient is selected as 5.5% and the radius of curvature as 4.5 m. The maximum uplift displacements will be examined in Chapter 5 and compared with the literature.

Table 3.14 Equivalent lateral force procedure for FPS

| **Analysis Type** | | *MCE-LB* | *MCE-Nom* | *MCE-UB* | *DBE-LB* | *DBE-Nom* | *DBE-UB* |
|---|---|---|---|---|---|---|---|
| **Seismic Weight (kN)** | $W$ | | | 499727 | | | |
| **Effective Period (s)** | $T_M$ | 3.488 | 3.378 | 2.874 | 2.883 | 2.459 | 1.897 |
| **Damping Ratio %** | $\xi$ | 21% | 24% | 30% | 30% | 30% | 30% |
| **Effective Stiffness (kN/m)** | $K_M$ | 165289 | 176202 | 243426 | 241936 | 332616 | 558692 |
| **Damping Scale Factor** | $\eta_M$ | 0.621 | 0.592 | 0.535 | 0.535 | 0.535 | 0.535 |
| **Spectral Acc. (g)** | $S_{ae}(T_l$ | 0.187 | 0.193 | 0.227 | 0.132 | 0.154 | 0.200 |
| **Max. Displ. (m)** | $D_M$ | 0.456 | 0.422 | 0.324 | 0.189 | 0.161 | 0.125 |
| **Max. Disp. w/ Torsion (m)** | $D_{TM}$ | **0.502** | 0.464 | 0.356 | 0.208 | 0.177 | 0.137 |
| **TBDY2018 Base Shear ($V_m$/W)** | | 0.116 | 0.114 | 0.121 | 0.070 | 0.083 | **0.107** |
| **ASCE7-16 Base Shear ($V_m$/W)** | | 0.123 | 0.122 | 0.131 | 0.076 | 0.089 | **0.116** |

The bilinear properties were obtained using the equations below, retrieved from TBDY2019 (Appendix 14B) and shown in Table 3.15 for MCE and Table 3.16 for DBE level seismic conditions.

$$F_Q = F_y = \mu_e P \tag{3.22}$$

$$k_2 = \frac{P}{R_c} \tag{3.23}$$

$$k_e = \frac{F}{D} = \frac{P}{R_c} + \frac{\mu_e P}{D} \tag{3.24}$$

$$\beta_e = \frac{1}{2\pi}\left[\frac{W_d}{FD}\right] = \frac{2}{\pi}\left[\frac{\mu_e}{\mu_e + D/R_C}\right] \tag{3.25}$$

Table 3.15 FPS isolator characteristics for MCE level seismic condition

| | | **MCE-LB** | **MCE-Nom** | **MCE-UB** |
|---|---|---|---|---|
| $\mu_e$ | | 0.0495 | 0.055 | 0.0858 |
| $R_C$ | m | 4.5 | 4.5 | 4.5 |
| $D$ | m | 0.351 | 0.325 | 0.249 |
| $F_{y,total}$ | kN | 24736 | 27485 | 42877 |
| $k_{2,total}$ | kN/m | 111050 | 111050 | 111050 |
| $k_{1,total} = 100k_2$ | kN/m | 11105044 | 11105044 | 11105044 |
| $k_{e,total}$ | kN/m | 181558 | 195747 | 283139 |
| $F_{max,total}$ | kN | 63697 | 63522 | 70545 |
| $\beta_e$ | % | 25% | 28% | 30% |
| $T_{eff}$ | s | 3.328 | 3.205 | 2.665 |
| $\omega$ | rad | 0.3005 | 0.3120 | 0.3752 |

Table 3.16 FPS isolator characteristics for DBE level seismic condition

| | | **DBE-LB** | **DBE-Nom** | **DBE-UB** |
|---|---|---|---|---|
| $\mu_e$ | | 0.0495 | 0.055 | 0.0858 |
| $R_C$ | m | 4.5 | 4.5 | 4.5 |
| $D$ | m | 0.145 | 0.124 | 0.096 |
| $F_{y,total}$ | kN | 24736 | 27485 | 42877 |
| $k_{2,total}$ | kN/m | 111050 | 111050 | 111050 |
| $k_{1,total} = 100k_2$ | kN/m | 11105044 | 11105044 | 11105044 |
| $k_{e,total}$ | kN/m | 281201 | 332620 | 558736 |
| $F_{max,total}$ | kN | 40881 | 41260 | 53512 |
| $\beta_e$ | % | 30% | 30% | 30% |
| $T_{eff}$ | s | 2.674 | 2.459 | 1.897 |
| $\omega$ | rad | 0.3739 | 0.4067 | 0.5271 |

#### 3.3.2.1 Friction Pendulum Isolator (FPI) Model

The plasticity model of Park et al. (1986) was adopted for the shear behavior, and the pendulum behavior is added by Zayas and Low (1990). The axial force is always nonlinear and have significant affects on the shear behavior (CSI Analysis Reference Manual, 2017).

The concept is shown in Figure 3.13. All three degrees of freedom are coupled. The nonlinear axial force-deformation behavior is defined with compression stiffness and zero tensile stiffness, Eq (3.26). The frictional and pendulum force deformation behavior are given in Eq (3.28) and Eq (3.29), respectively. Frictional behavior is highly affected by the variation in nonlinear axial load during an earthquake.

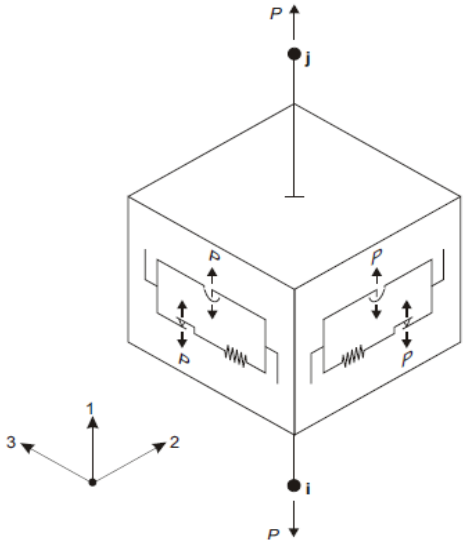


Figure 3.13. FPI model concept (retrieved from CSI Analysis Reference Manual, 2017)

$$f_{u1} = P = \begin{cases} \boldsymbol{k_1} d_{u1} & if\ d_{u1} < 0 \\ 0 & otherwise \end{cases} \tag{3.26}$$

$$f_{u2,3} = \underset{friction}{f_{u2,3f}} + \underset{pendulum}{f_{u2,3p}} \tag{3.27}$$

The frictional force-deformation relationship is given by:

$$f_{u2,3f} = -P\mu_{2,3} z_{2,3} \tag{3.28}$$

$$\mu_{2,3} = \boldsymbol{fast_{2,3}} - (\boldsymbol{fast_{2,3}} - \boldsymbol{slow_{2,3}})e^{-rv} \tag{3.29}$$

The comma notation is used to separate the directions in the terms in order not to show the same equations again. Where, $slow2,3$ are the friction coefficients at zero velocity, and $fast2,3$ are the friction coefficients at fast velocities in corresponding horizontal direction (2 or 3). The friction coefficient is normally increases with sliding velocity for Teflon-steel materials (Nagarajaiah et al,1991). The resultant velocity is denoted as $v$. The $r$ is an effective inverse velocity and characterized by inverse of characteristic sliding velocities, $rate_{2,3}$.

$$v = \sqrt{\dot{d}_{u2,3}^2 + \dot{d}_{u3,2}^2}$$

$$r = \frac{\boldsymbol{rate_{2,3}}\, \dot{d}_{u2,3}^2 + \boldsymbol{rate_{3,2}} \dot{d}_{u3,2}^2}{v^2}$$

$z_{2,3}$ are the internal hysteretic variables. The range of the variables was in the range of $\sqrt{z_2^2 + z_3^2} \leq 1$ outside of the yield region, and $\sqrt{z_2^2 + z_3^2} = 1$, circular shape at the yield surface. The value of the hysteretic parameters are defined according to following implicit differential equations and having a zero value at initial conditions. The relation (Eq (3.30)) were constructed by using the dimensionless quantities that control the shape of the hysteresis in Park et al. (1986) with $A = 1$ and $\beta = \gamma = 0.5$.

$$\begin{Bmatrix} \dot{z_2} \\ \dot{z_3} \end{Bmatrix} = \begin{bmatrix} 1 - a_2 z_2^2 & -a_3 z_2 z_3 \\ -a_2 z_2 z_3 & 1 - a_3 z_3^2 \end{bmatrix} \begin{Bmatrix} \dfrac{\boldsymbol{k_2}}{P\mu_{u2}} \dot{d_{u2}} \\ \dfrac{\boldsymbol{k_3}}{\mu_{u2}} \dot{d_{u3}} \end{Bmatrix} \tag{3.30}$$

Where, $k_2$ and $k_3$ are the initial elastic shear stiffnesses and,

$$a_2 = \begin{cases} 1 & if\ d_{u2}\dot{z_2} > 0 \\ 0 & otherwise \end{cases}$$

$$a_3 = \begin{cases} 1 & if\ d_{u3}\dot{z_3} > 0 \\ 0 & otherwise \end{cases}$$

The pendulum force-deformation relationship is given below. $\boldsymbol{radius_2}$ and $\boldsymbol{radius_3}$ are the effective radius of curvature (pendulum length) of the sliding surface. Generally, the radius of curvature and friction coefficients are the same for both shear directions.

$$f_{u2,3p} = -P \frac{d_{u2,3}}{\boldsymbol{radius_{2,3}}}$$

The input parameters that are bolded in previous equations were introduced to the analysis program. These are axial compression stiffness, elastic shear stiffness, friction coefficients at zero and fast velocities, rate parameter and pendulum radius. Used parameters are given in Table 3.17, Table 3.18 and Table 3.19, for MCE-LB, DBE-Nom, and DBE-UB level analyses.

Table 3.17 FPI model input parameters for MCE-LB

| | *Type 1* | *Type 2* | *Type 3* |
|---|---|---|---|
| k2,3 | 40872 | 113327 | 141448 |
| slow2,3 | 0.0396 | 0.0396 | 0.0396 |
| fast2,3 | 0.0495 | 0.0495 | 0.0495 |
| rate2,3 | | 1 | |
| radius2,3 | | 4.5 | |

Table 3.18 FPI model input parameters for DBE-Nom

| | *Type 1* | *Type 2* | *Type 3* |
|---|---|---|---|
| k2,3 | 40872 | 113327 | 141448 |
| slow2,3 | 0.0440 | 0.0440 | 0.0440 |
| fast2,3 | 0.0550 | 0.0550 | 0.0550 |
| rate2,3 | | 1 | |
| radius2,3 | | 4.5 | |

Table 3.19 FPI model input parameters for DBE-UB

| | *Type 1* | *Type 2* | *Type 3* |
|---|---|---|---|
| k2,3 | 40872 | 113327 | 141448 |
| slow2,3 | 0.0686 | 0.0686 | 0.0686 |
| fast2,3 | 0.0858 | 0.0858 | 0.0858 |
| rate2,3 | | 40872 | |
| radius2,3 | | 4.5 | |

#### 3.3.2.2 Sharp Bilinear (BL) Model

The same sharp bilinear model used as Section 3.3.1.3 was also adopted for FPS isolators. This is a model used by many engineers who are inexperienced of the nonlinear concept of the nonlinear frictional behavior of sliding isolators. Although, FPS has coupled degrees of freedom in all directions, in BL model all three directions are independent from each other.

The bilinear concept is presented in Figure 3.14. Bilinear properties were obtained from Table 3.15, and Table 3.16, and hysteresis envelope input are constructued and shown from Figure 3.15, Figure 3.16, and Figure 3.17. The axial force-deformation relationship of each type is shown in Figure 3.18.

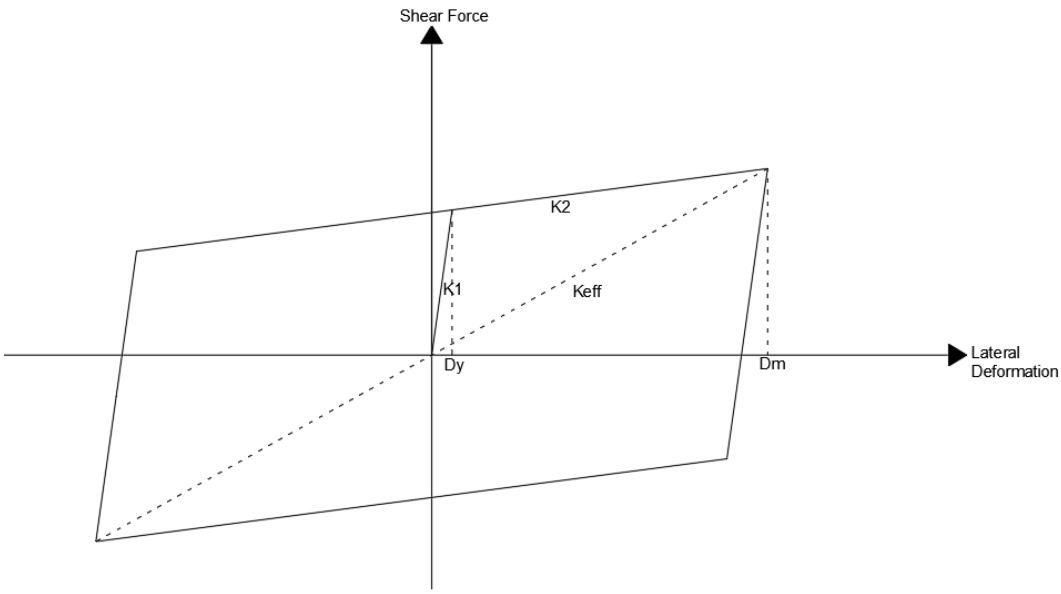


Figure 3.14. Sharp bilinear concept

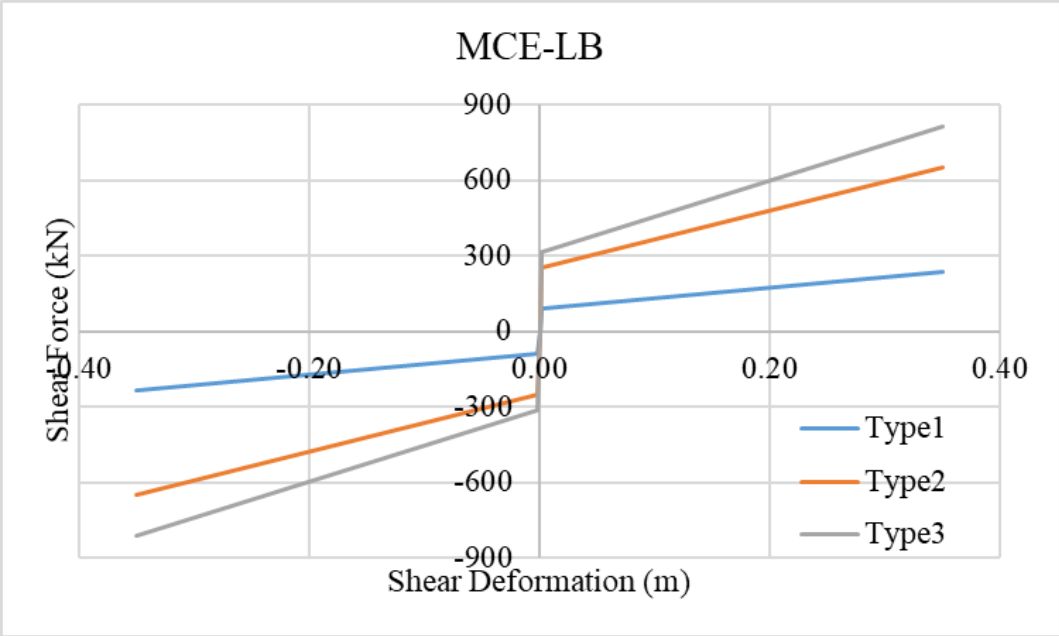


Figure 3.15. FPS sharp bilinear envelope input for MCE-LB isolator properties

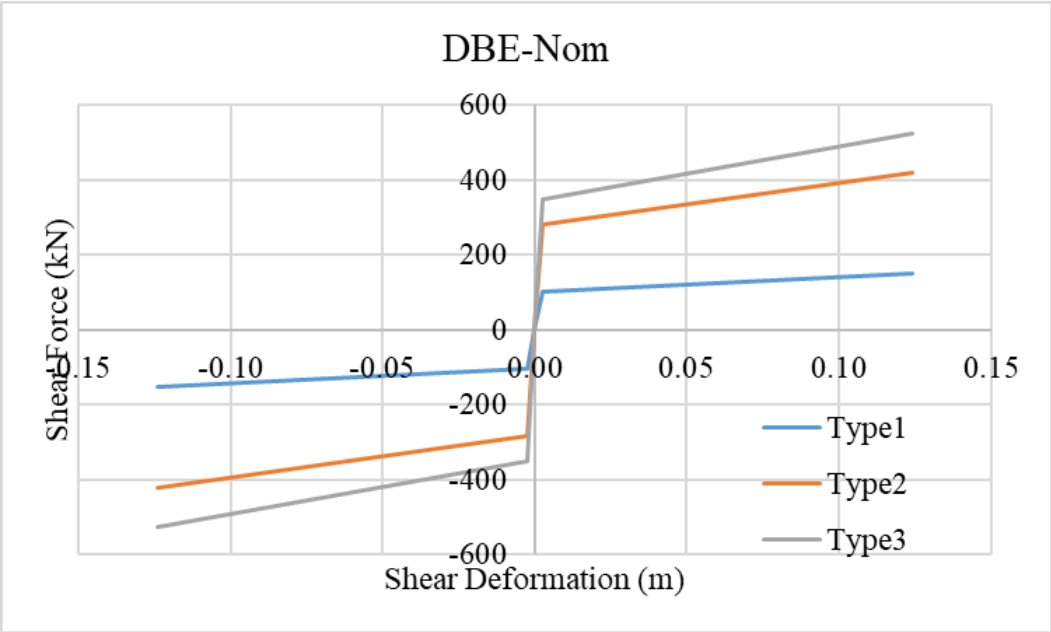


Figure 3.16. FPS sharp bilinear envelope input for DBE-Nom isolator properties

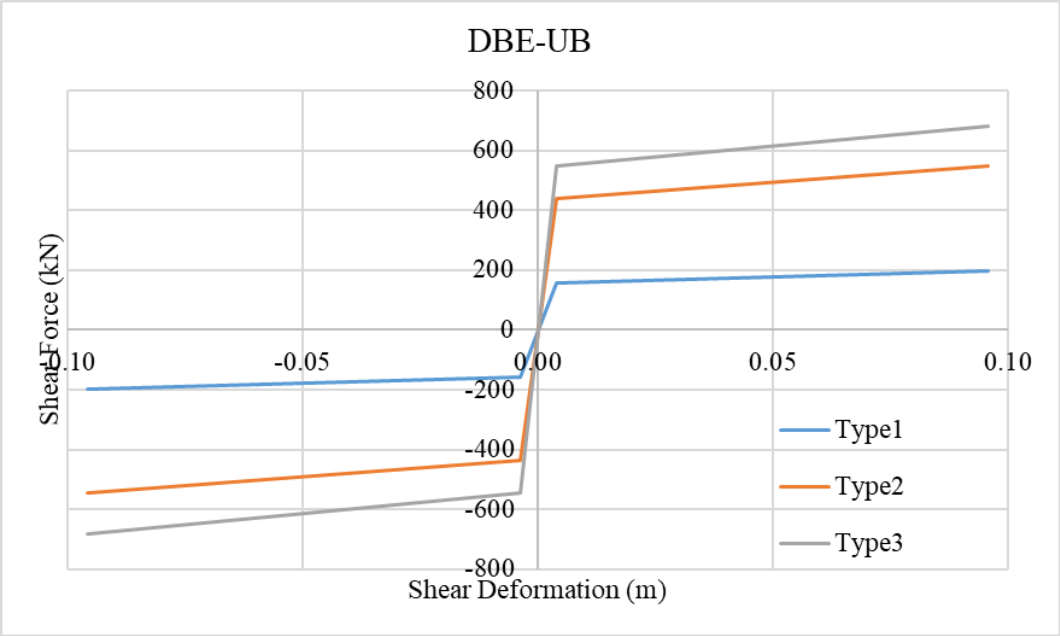


Figure 3.17. FPS sharp bilinear envelope input for DBE-UB isolator properties

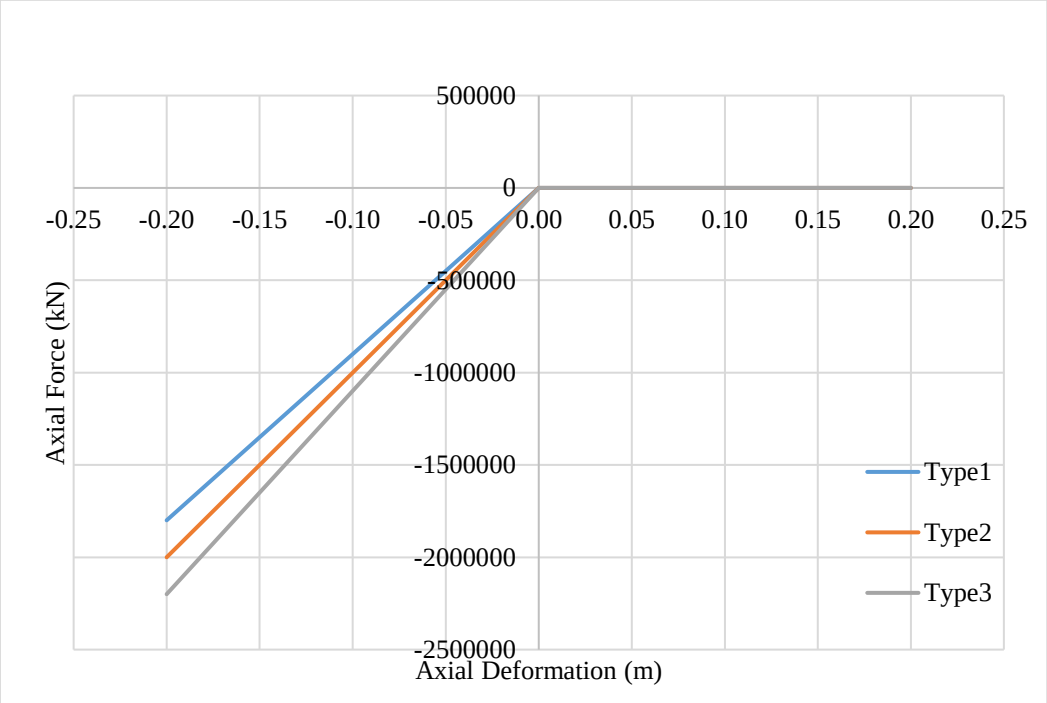


Figure 3.18. FPS sharp bilinear axial load-deformation input

# CHAPTER 3

# NONLINEAR TIME HISTORY ANALYSIS

This chapter covers nonlinear time-history analysis, which was used to assess the structural performance of selected isolator models under selected seismic excitations. Fast Nonlinear Analysis (FNA), i.e., Nonlinear Modal Time-History Analysis (Ibrahimbegovic & Wilson, 1989; Wilson, 1993), was chosen due to its efficiency compared to the Direct Integration method. The method is implemented in ETABS. First, the theoretical background of the FNA method is discussed. Later, ETABS load case implementation and selected analysis options for eleven ground motions are explained.

## 4.1 Fast Nonlinear Analysis (FNA)

The response of structures under considerable dynamic input shows significant nonlinear behavior. These nonlinearities generally include P-delta effects and nonlinear material properties. For the response history analysis of linear and nonlinear systems, N. M. Newmark (1959) developed a family of methods, known as “direct time-integration methods”. In the direct integration method, the complete equilibrium equations are formed and solved at each time step. Solving the nonlinear behavior of elements throughout the structure using the direct integration method may require enormous analysis time, in the magnitudes of hours/days, especially for relatively larger real-scale buildings.

E. L. Wilson (2000) proposed an analysis method for structures having a limited number of nonlinear elements, such as base isolators, dampers and gap elements. This new method is called Fast Nonlinear Analysis (FNA) and can reduce analysis duration significantly.

In FNA method, fundamental equations of mechanics (equilibrium, force-deformation and compatibility) are satisfied. The matrix equation of motion at time (t) is given in Eq (4.1),

$$\mathbf{M}\ddot{\boldsymbol{u}}(t) + \boldsymbol{C}\dot{\boldsymbol{u}}(t) + \boldsymbol{K}_L\boldsymbol{u}(t) + \boldsymbol{R}(t)_{NL} = \boldsymbol{R}(t) \qquad (4.1)$$

Where $\mathbf{M}$, $\boldsymbol{C}$, and $\boldsymbol{K_L}$ are the mass, damping and the linear effective stiffness matrices, respectively. The size of the matrices is equal to the number of degrees of freedom for the corresponding node. $\ddot{\boldsymbol{u}}(t)$, $\dot{\boldsymbol{u}}(t)$, $\boldsymbol{u}(t)$ and $\boldsymbol{R}(t)$ are the nodal point acceleration, velocity, displacement, and externally applied load (seismic excitation), respectively. $\boldsymbol{R}(t)_{NL}$ is the vectorial sum of the forces in nonlinear elements and is computed by iteration at each step.

There are cases when the computer model becomes unstable without the nonlinear elements. In this case, the linear effective stiffness, $\boldsymbol{K_{NL}}$ of the nonlinear elements can be added, and Eq (4.1) can be rewritten as the following equation.

$$\mathbf{M}\ddot{\boldsymbol{u}}(t) + \boldsymbol{C}\dot{\boldsymbol{u}}(t) + (\boldsymbol{K_L} + \boldsymbol{K_{NL}})\boldsymbol{u}(t) = \boldsymbol{R}(t) - \boldsymbol{R}_{NL}(t) + \boldsymbol{K_{NL}}\boldsymbol{u}(t) \qquad (4.2)$$

The effective stiffness at nonlinear degrees of freedom ($\boldsymbol{K_{NL}}$) is arbitrary; however, it varies between zero and maximum nonlinear stiffness of the corresponding degree of freedom. Also, the exact dynamic equilibrium equations for the model can be written as:

$$\mathbf{M}\ddot{\boldsymbol{u}}(t) + \boldsymbol{C}\dot{\boldsymbol{u}}(t) + \boldsymbol{K}\boldsymbol{u}(t) = \bar{\boldsymbol{R}}(t) \qquad (4.3)$$

Where $\boldsymbol{K}$ is the elastic stiffness matrix and is equal to $\boldsymbol{K_L} + \boldsymbol{K_{NL}}$. The effective external load $\bar{\boldsymbol{R}}(t)$ is equal to $\boldsymbol{R}(t) - \boldsymbol{R}(t)_N + \boldsymbol{K_N}\boldsymbol{u}(t)$, and evaluated by iteration. The convergence rate of the solution can be increased by a reasonable estimation of the effective elastic stiffness.

Modal analysis is conducted using the stiffness matrix $\boldsymbol{K}$. and the mass matrix $\mathbf{M}$. The ritz vector method for the solution of the modal equations is recommended by CSI (CSI Analysis Reference Manual, 2017).

The equilibrium equations are written in modal form as:

$$\Omega^2\mathbf{a}(\mathrm{t}) + \Lambda\dot{\mathbf{a}}(\mathrm{t}) + \boldsymbol{I}\ddot{\mathbf{a}}(\mathrm{t}) = \boldsymbol{q}(t) - \boldsymbol{q}_e(t) \tag{4.4}$$

The modal equations are shown from Eq (4.5) to Eq (4.10). Where, $\Omega^2$ is the diagonal matrix of squared structural frequencies. $\Lambda$ is the modal damping matrix which is diagonal. $\boldsymbol{I}$ is the identity matrix which satisfies Eq (4.7), $\boldsymbol{q}(t)$ is the vector of modal applied loads, and $\boldsymbol{q}_N(t)$ is the vector of modal forces from nonlinear elements (links), and $\mathrm{a}(\mathrm{t})$ is the amplitude of modal deformations.

$$\Omega^2 = \Phi^{\mathrm{T}}\boldsymbol{K}\Phi \tag{4.5}$$

$$\Lambda = \Phi^{\mathrm{T}}\boldsymbol{C}\,\Phi \tag{4.6}$$

$$\boldsymbol{I} = \Phi^{\mathrm{T}}\boldsymbol{M}\Phi \tag{4.7}$$

$$\boldsymbol{q}(t) = \Phi^{\mathrm{T}}\boldsymbol{R}(t) \tag{4.8}$$

$$\boldsymbol{q_N}(t) = \Phi^{\mathrm{T}}[\boldsymbol{R}_{NL}(t) - \boldsymbol{K}_N\boldsymbol{u}(t)] \tag{4.9}$$

$$\boldsymbol{u}(t) = \Phi\mathbf{a}(\mathrm{t}) \tag{4.10}$$

In the above equations, $\Phi$ is the mode shape. It should be noted that since $\boldsymbol{q_N}(t)$ is a function of modal amplitude $\mathbf{a}(\mathrm{t})$, unlike linear dynamic analysis, the modal equations are coupled. In Ritz vector modal analysis, 500 modes were used and, 100% mass participation in each direction were achieved.

Knowing the damping ratio in the structural system is also crucial to construct the damping matrix. In a 3-D analysis, the nonlinear behavior of the isolators will include hysteretic damping during the lateral deformation for the corresponding first three modes and the superstructure will remain linear elastic with no energy dissipation. Also, it is widely accepted that reinforced concrete structures have a damping ratio of 5% during a seismic motion (Chopra, 2012; Pant et al., 2013). Therefore, since additional damping is not desired in the isolation system's dominant modes, a small damping ratio 0.5% is assigned to the first three modes for all load cases. Zero damping ratio is avoided to prevent numerical problems. Damping in all other modes (superstructural modes) is kept constant at 5% for the RC structure.

Since the inter-story drifts of the building were yielded close to 0.5%, no cracking is expected in the concrete. Therefore 5% damping might not be satisfied in base-isolated cases. For this reason, a comparison of superstructural response for 5% and 2% damping is given in Appendix D. as an additional analysis. For the 2% damping case, higher accelerations are obtained while inter-story drifts remain similar.

As a validation for the FNA analysis, additional analyses using Newmark's DI method for specified earthquakes were conducted and compared in terms of hysteresis curves and superstructural response. The results are given in Appendix E. The hysteresis response is compatible with both methods. However, Higher superstructural responses (accelerations and story drifts) up to 10% were obtained with selected DHI and MLP modeling approaches, except enormously amplified accelerations at Floor 2 are observed when the DI method is used. The convergence of the solution could not be satisfied when the FPI model is analyzed by the direct integration method due to the negative and zero stiffnesses during the uplift movements (CSI Analysis Reference Manual, 2017).

## 4.2 Load Case Implementation

Load case definitions for 3-D nonlinear time-history analyses were constructed for 11 ground motions, presented in Section 0, separately with the scale factors for DBE and MCE level earthquakes. The FNA method is selected for the solution. All three components of the ground motions were assigned according to guidelines in TBDY2019.

To account for the static loading conditions before the earthquake excitation, the structural weight (G+0.3Q) was applied as the nonlinear initial condition for all load cases. The seismic weight was administered with a ramp-shaped loading function that reached a total unity amplitude with a 20 s duration. This is important, especially for frictional sliding isolators. If there is zero compression load on the isolator as an initial condition, no initial horizontal stiffness is generated; therefore, the convergence of the solution cannot be achieved at the beginning of the analysis. The structural stiffness is recomputed after the application of the service loads, and tridirectional seismic excitation begins with modified stiffnesses.

Two orthogonal horizontal components of the ground motions were introduced in the analysis program with the same scale factors. For each ground motion, two sets of load cases were defined by interchanging the orthogonal components of the acceleration history. A total of 22 load cases were used in the analysis. The results of each ground motion are obtained by considering the maximum response in each set. The final structural response was evaluated by taking the average of the related parameter of 11 ground motions.

The vertical component was also included in each load case since the period of the dominant vertical mode (0.149 s) was found to be more than 0.1 s (TBDY2019). The scale factor was used the same as the lateral ones.

# CHAPTER 4

# RESPONSE OF ISOLATED HOSPITAL BUILDING

In this chapter, the response of both the isolation system and the superstructure is assessed. The evaluation of response is conducted by obtaining the average results of eleven ground motions. The hysteresis curves and the axial response of the links were considered separately for several ground motions. The isolation system and structural performance was evaluated according to maximum displacements, structural forces and base shear coefficient, floor accelerations, inter-story drifts, and hysteretic curves.

## 5.1 Maximum Isolation Displacements

Time history displacement response in both lateral directions was obtained for each MCE ground motion with lower bound parameters. The horizontal displacements were directionally combined at each time step. The average results of the eleven ground motions were used to determine maximum displacement. Maximum displacements were increased by %10, the minimum value, in this case, to account for additional rotational effects.

A rigid first-floor slab, i.e., isolation mat, acts as a constraint for the top isolator nodes; therefore, no relative lateral displacements are expected during a translational displacement. However, due to the asymmetric plan of the building rotational movements are present. Therefore, three different locations, which are the center of the building, right-wing corner, and bottom wing corner, on the isolation system were selected to observe the relative displacements throughout the structure. The location of the isolators is shown on the isolator layout in Figure 5.1.

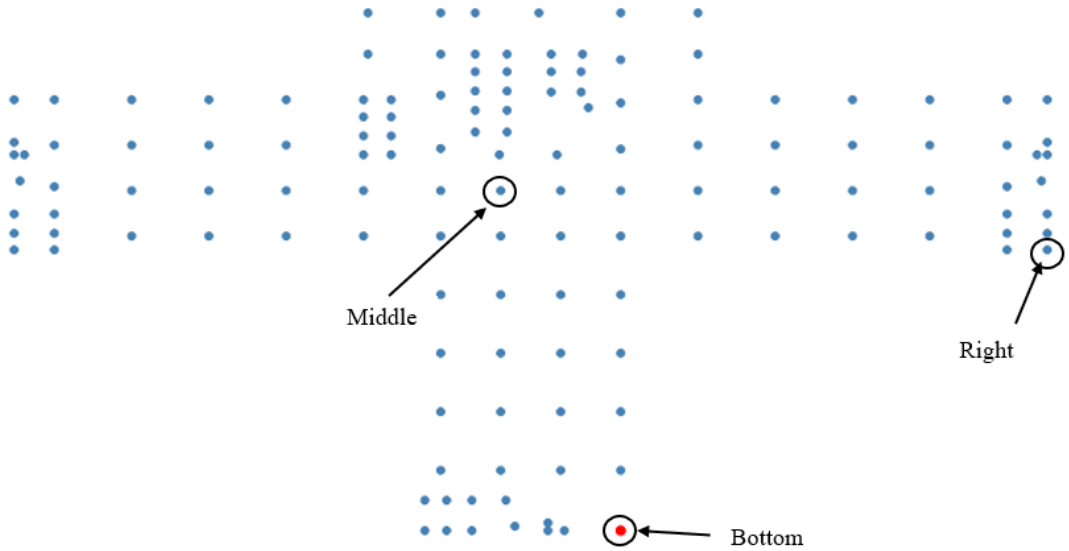


Figure 5.1. Selected isolator locations for system displacement response (the isolator layout is retrieved from ETABS plugin by Ulker Eng.)

The orbital displacement response of each selected location is evaluated for each HDRB model, and the average of maximum displacements from eleven ground motions are plotted on the graphs. Also, maximum values of three selected locations are given to assess additional displacements due to torsion.

Ux-Uy displacement response of all ground motions for the HDRB models are shown from Figure 5.2 to Figure 5.4. Also, the maximum direction displacement of each ground motion and their average are presented in Table 5.1. Average maximum combined displacements for the DHI, smoothed BW, and sharp BL models were gathered as 36.3, 36.2, and 35.0 cm, respectively. When the displacements are increased by 10% for torsional effects, they are obtained as 39.9, 39.8, and 38.5 cm. The ELFP method yielded maximum displacements as 37.8 and 41.6 cm with and without torsion, respectively. The least displacements were obtained from sharp BL models, with an 8% decrease from the preliminary ELFP analysis.

Excessive deformations are observed in the ground motions RSN316 (Westmorland, 1981) and RSN821 (Erzincan, 1992), which have pulse-like behavior and near-fault effects in the records. In ground motion, RSN316, 61.3, 61.2, and 64.8 cm

displacements are observed for DHI, BW, and BL models, respectively. In this case, the BL model yielded the maximum deformations. Furthermore, the displacements are obtained very close to each other for different models in RSN850. Therefore, there is no regular pattern in isolation system displacements for different HDRB modeling approaches. Although the average displacements are close to each other, the displacement response could be underestimated or overestimated with bilinear models when the ground motions are evaluated separately. The deformation response of the system is highly dependent also on the seismic input characteristics.

Table 5.1 Maximum displacements of HDRB models (units are in cm)

| | **DHI Model** | | | **BW Model** | | | **BL Model** | | |
|---|---|---|---|---|---|---|---|---|---|
| **Eq ID** | **Bottom** | **Middle** | **Right** | **Bottom** | **Middle** | **Right** | **Bottom** | **Middle** | **Right** |
| **RSN0187** | 37.61 | 36.91 | 41.51 | 37.51 | 36.82 | 41.47 | 43.85 | 42.86 | 45.09 |
| **RSN0316** | 58.23 | 58.36 | 61.32 | 57.97 | 58.13 | 61.22 | 64.07 | 64.09 | 64.79 |
| **RSN0549** | 24.73 | 23.28 | 25.68 | 24.63 | 23.20 | 25.63 | 18.21 | 17.95 | 20.23 |
| **RSN0558** | 20.28 | 19.69 | 20.02 | 20.22 | 19.64 | 19.99 | 18.66 | 17.79 | 18.05 |
| **RSN0821** | 47.16 | 48.07 | 47.44 | 47.00 | 47.93 | 47.35 | 54.12 | 53.95 | 55.21 |
| **RSN0850** | 21.34 | 20.56 | 20.45 | 21.25 | 20.48 | 20.41 | 21.17 | 20.85 | 20.80 |
| **RSN1116** | 31.32 | 31.33 | 31.25 | 31.17 | 31.20 | 31.21 | 28.57 | 28.41 | 26.50 |
| **RSN1158** | 41.24 | 40.54 | 42.63 | 41.04 | 40.38 | 42.55 | 36.73 | 36.39 | 38.09 |
| **RSN1605** | 44.27 | 44.54 | 44.58 | 44.11 | 44.40 | 44.51 | 38.93 | 40.02 | 40.35 |
| **RSN2752** | 33.50 | 33.04 | 33.02 | 33.36 | 32.92 | 32.94 | 35.30 | 35.52 | 35.52 |
| **RSN6893** | 29.69 | 30.03 | 31.23 | 29.59 | 29.94 | 31.20 | 19.36 | 19.45 | 20.44 |
| **AVE** | 35.40 | 35.12 | 36.28 | 35.26 | 35.00 | 36.22 | 34.45 | 34.30 | 35.01 |
| **Dm** | 36.28 | | | 36.22 | | | 35.01 | | |
| **Dtm** | 39.91 | | | 39.84 | | | 38.51 | | |

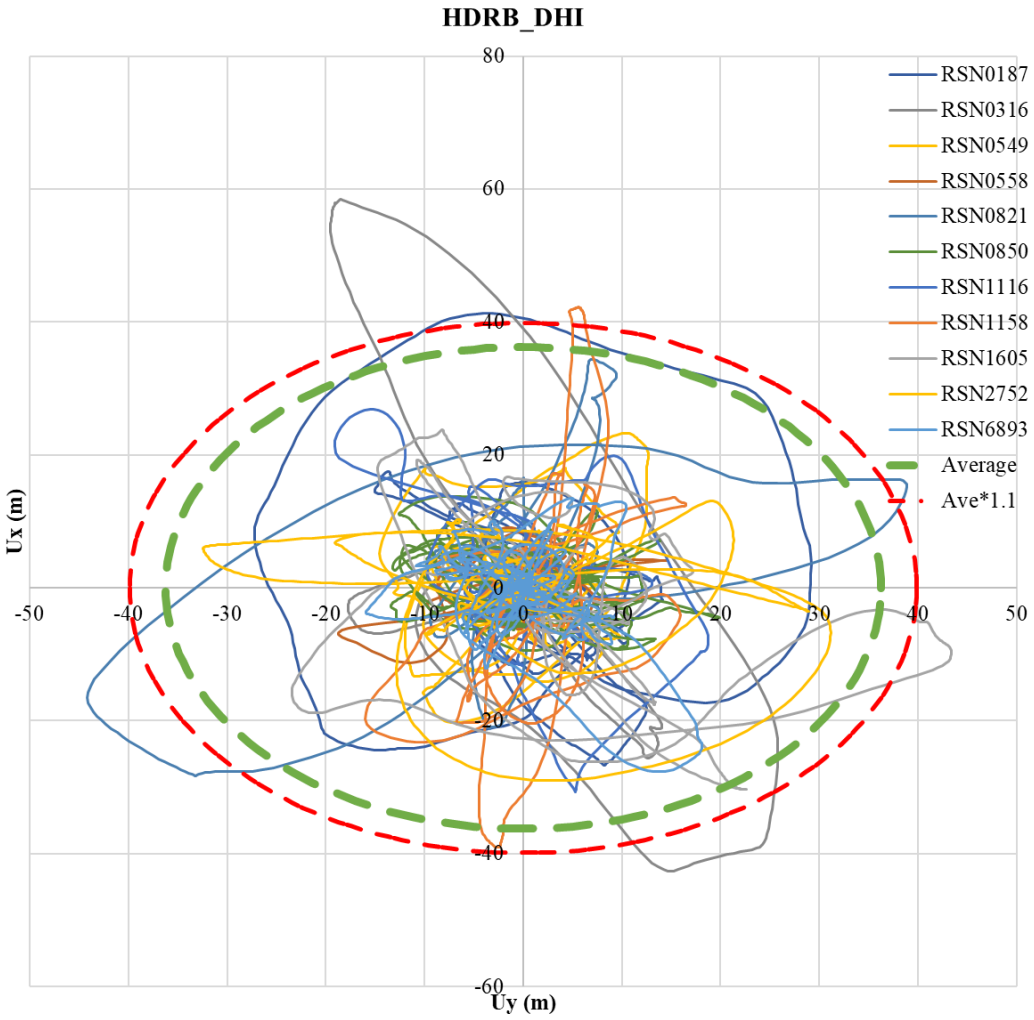


Figure 5.2. Orbital displacement response of HDRB-DHI model

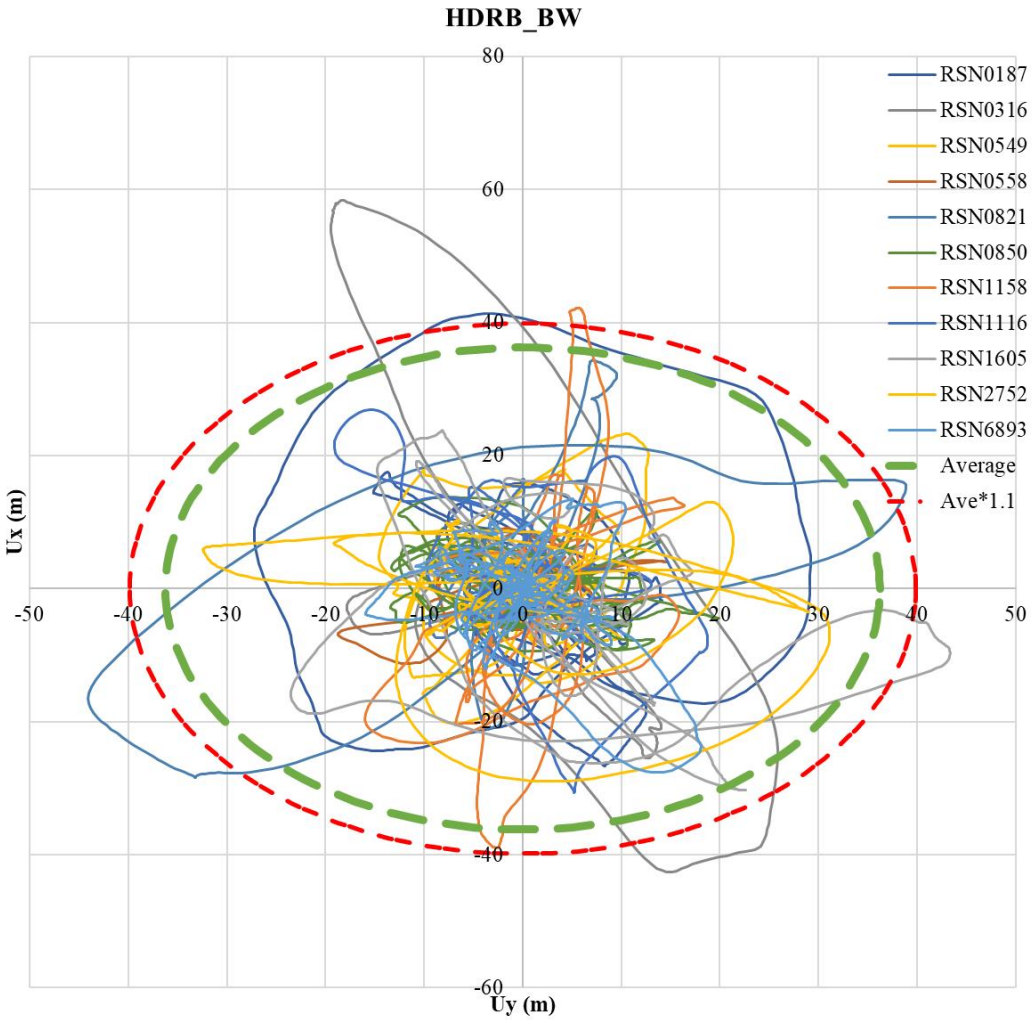


Figure 5.3. Orbital displacement response of HDRB-BW model

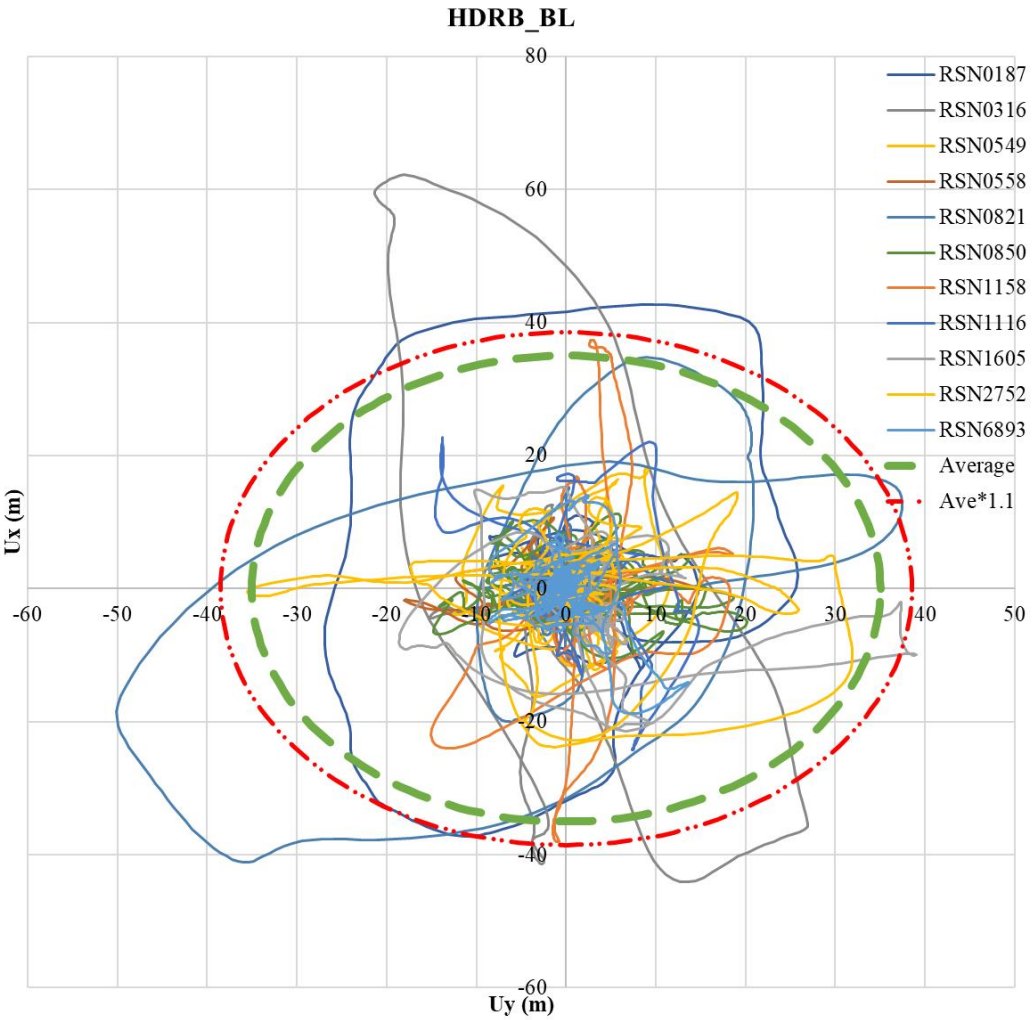


Figure 5.4. Orbital displacement response of HDRB-BL model

The displacement responses of FPS models are shown in Figure 5.5 and Figure 5.6 for FPI and BL cases. Also, the maximum direction displacement of each ground motion and their average are presented in Table 5.2. The tables showed average maximum direction displacements for FPI and sharp BL models as 42.4 and 35.9 cm, respectively. When increased by torsion, 46.6 and 39.5 cm displacements were obtained.

Table 5.2 Maximum displacement comparison of FPS models (units are in cm)

| | **FPI Model** | | | **BL Model** | | |
|---|---|---|---|---|---|---|
| **Eq ID** | **Bottom** | **Middle** | **Right** | **Bottom** | **Middle** | **Right** |
| **RSN0187** | 48.10 | 46.80 | 47.70 | 46.71 | 45.54 | 47.19 |
| **RSN0316** | 81.80 | 81.94 | 83.42 | 66.62 | 66.86 | 62.50 |
| **RSN0549** | 22.43 | 22.34 | 22.66 | 17.35 | 16.52 | 15.05 |
| **RSN0558** | 16.88 | 17.22 | 17.05 | 16.58 | 16.47 | 16.53 |
| **RSN0821** | 48.84 | 49.23 | 48.91 | 51.86 | 50.19 | 51.90 |
| **RSN0850** | 20.30 | 19.74 | 20.05 | 17.29 | 15.16 | 15.05 |
| **RSN1116** | 31.24 | 31.13 | 30.89 | 28.38 | 27.97 | 26.67 |
| **RSN1158** | 50.47 | 50.62 | 50.28 | 44.63 | 44.57 | 44.94 |
| **RSN1605** | 62.63 | 61.91 | 61.42 | 43.31 | 43.87 | 43.97 |
| **RSN2752** | 49.88 | 50.17 | 50.32 | 39.78 | 38.67 | 38.55 |
| **RSN6893** | 32.10 | 32.48 | 33.37 | 22.08 | 22.47 | 23.30 |
| **AVE** | 42.24 | 42.14 | 42.37 | 35.87 | 35.30 | 35.06 |
| **Dm** | 42.37 | | | 35.87 | | |
| **Dm*1.1** | 46.61 | | | 39.46 | | |

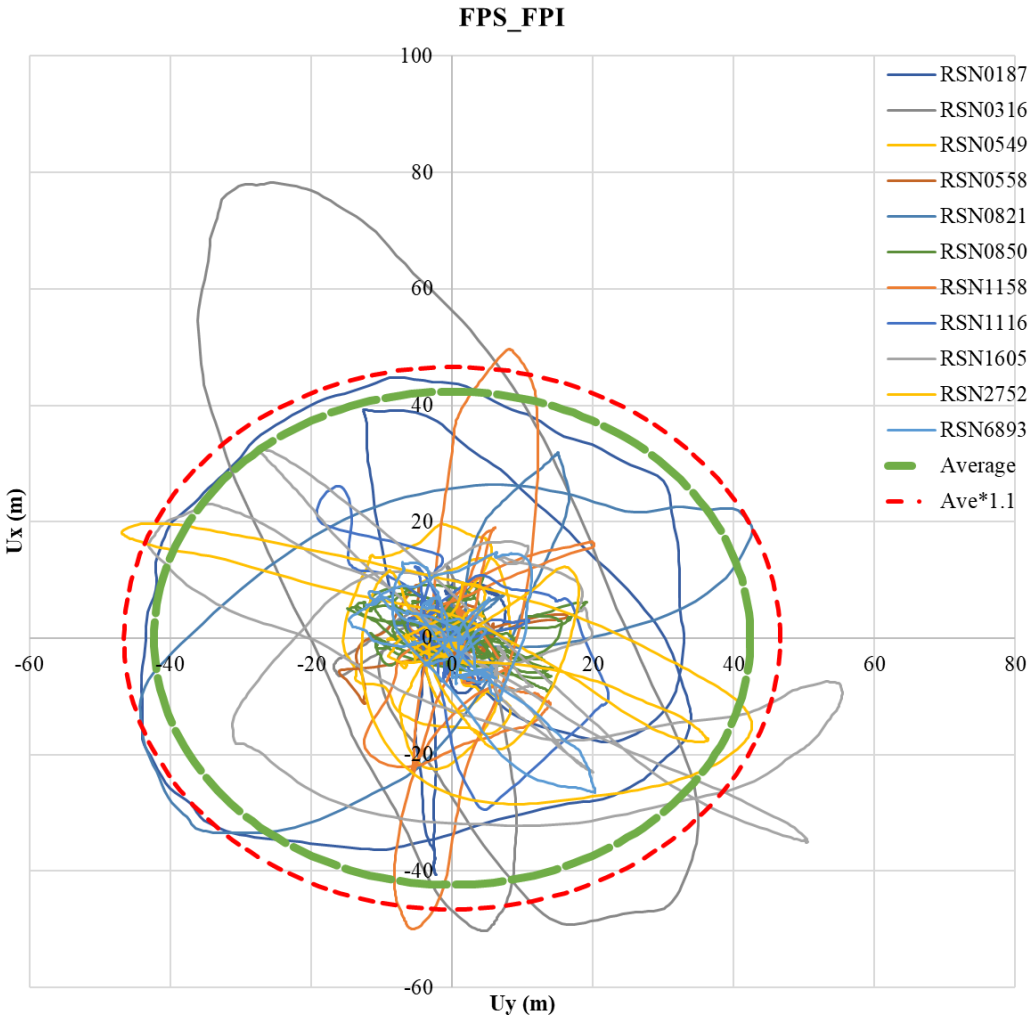


Figure 5.5. Orbital displacement response of FPS-FPI model

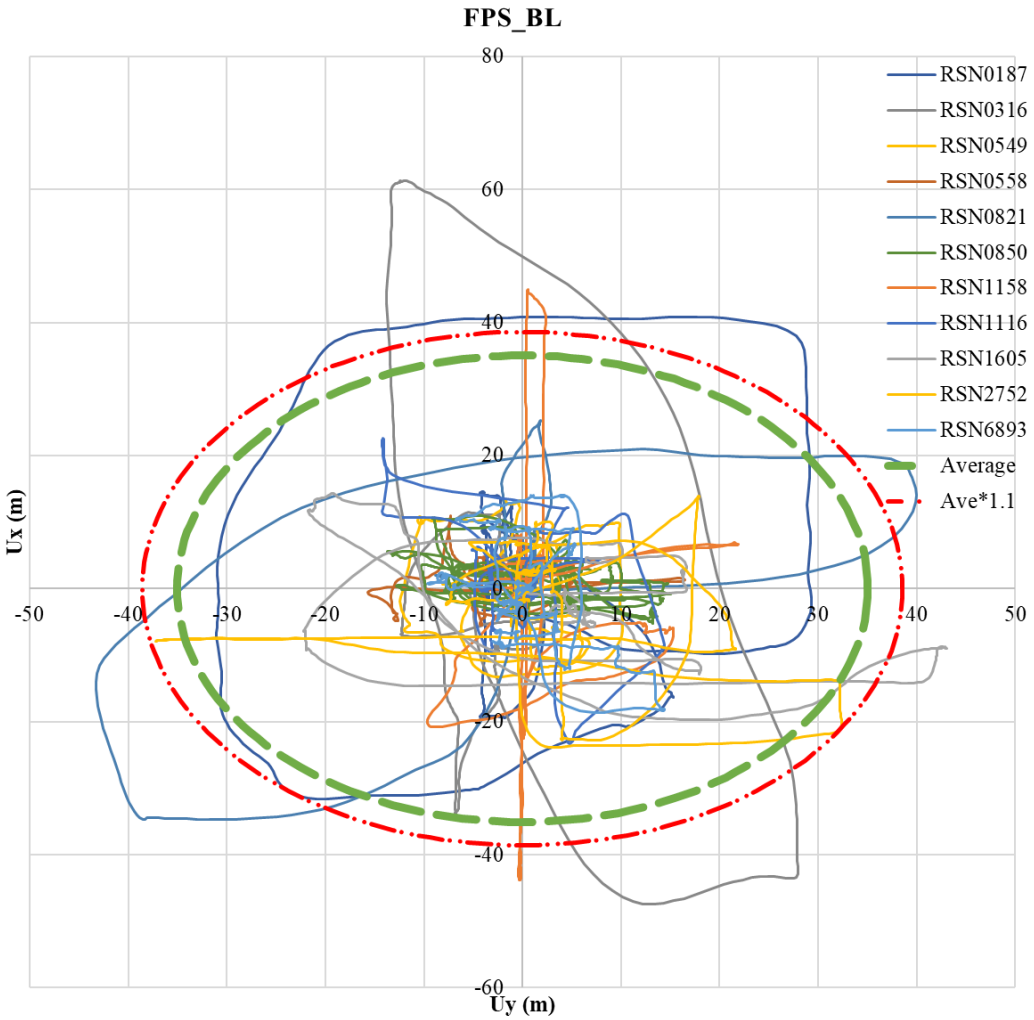


Figure 5.6. Orbital displacement response of FPS-BL model

The energy damping and nonlinear stiffness properties are prone to change during uplift movements in an ideal condition, especially for sliding isolators. Also, in the models which can account for biaxial excitation of the ground motion, displacements in one direction affect the other degree of freedom. Since the sharp BL model always follows the specified path and does not compute biaxial excitation, there is no variation of stiffnesses or displacements due to the previous comments. This might lead to maximum displacements that are less or higher than more realistic models. The characteristics of the ground motion is also significant. These results are suitable with the findings of Mavronicola and Komodromos (2014).

There is a small difference, a maximum of %7, in the displacement response of different parts of the structure. Depending on the ground motion Bottom, Middle, or Right locations showed higher or similar results than others with no pattern.

## 5.2 Structural Forces

The story forces and base shear reaction above the isolation layer are evaluated in this section. The story forces at the bottom of the floors were obtained for each isolator model in DBE seismic level with upper bound isolator properties. The average forces for the eleven ground motions were calculated. Then the forces were normalized with the structural weight. The story force distribution is plotted on the graphs separately for HDRB and FPS designs. In the charts, floor numbers are defined in the Y-axis. Floor -1 is the basement floor. The isolators are located at Floor 0, and the first floor just above the isolation mat is Floor 1. The results show that story forces are generally increased when the smooth BW and sharp BL models were used instead of more accurate nonlinear models such as DHI and FPI.

For HDRB isolators, the average story force distributions in X and Y directions are shown in Figure 5.7 and Figure 5.8, respectively. These results are observed to be increased in X direction when bilinear models are used. The BW model showed slightly lower story shear forces in the first four floors in Y direction. Among the

models, the sharp BL model yielded significantly higher demands for the structure. Smoothed BW model was shown more compatibility with the DHI model, especially at the higher floors.

When the average forces for MCE level earthquake is assessed in Figure 5.9 and Figure 5.10, the BW model yielded slightly lower forces than DHI, especially for the first floors. Therefore, the estimation of the BW model might change when different earthquake level is applied. The reason might be attributed to the stiffness increase after 200% shear strain for the DHI model, resulting in higher forces. On the other hand, the BL model always results in the highest response. However, the difference are more insignificant compared to the results with DBE level analysis.

The force demands showing the distribution for each earthquake are given from Figure 5.11 to Figure 5.16 for the HDRB models for in both directions. There is an amplification of the forces in the DHI models in Floor 1, especially for earthquakes with higher scale factors or pulse-like characteristics. Similar graphs can also be drawn for BL and BW models.

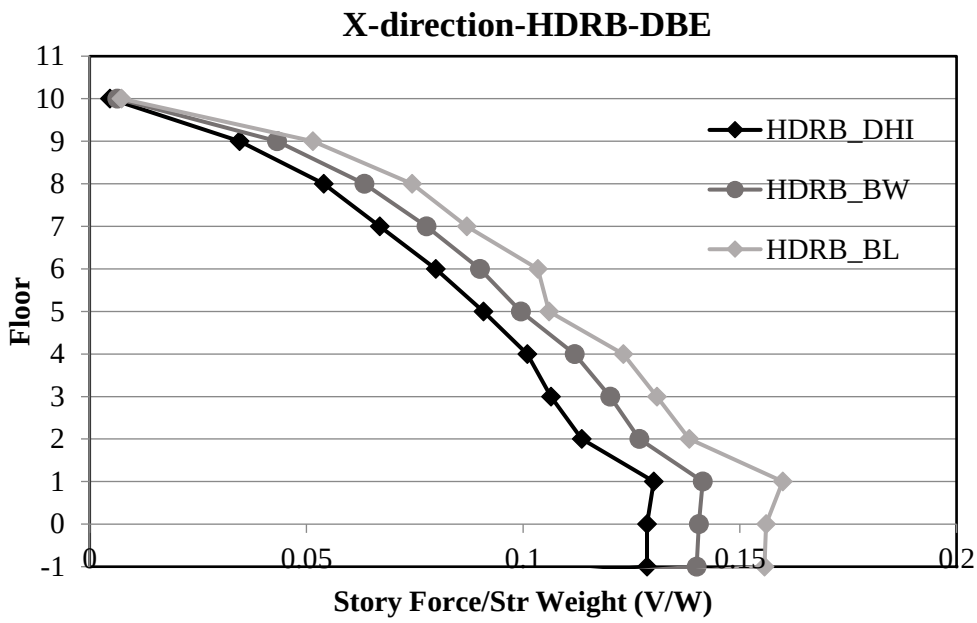


Figure 5.7. Story forces for HDRB models in the X direction with DBE-UB parameters

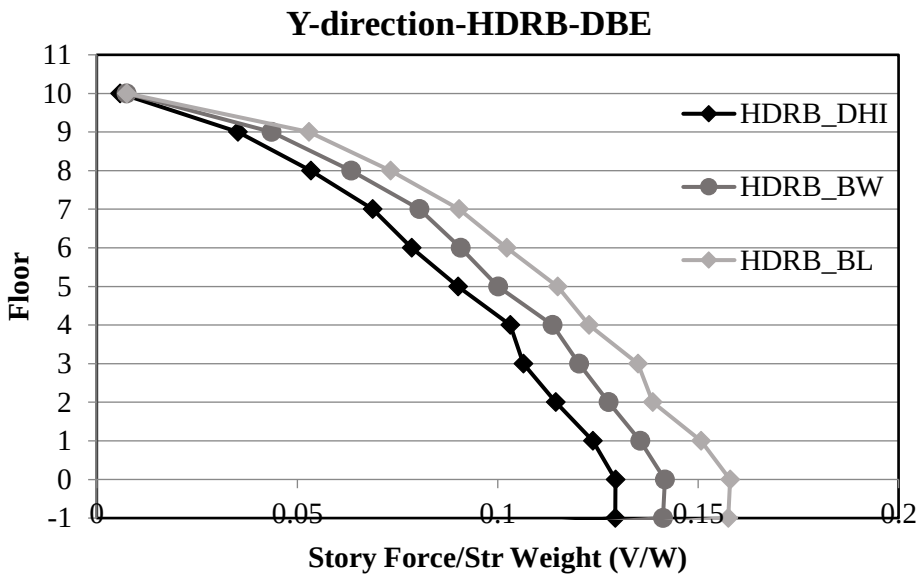


Figure 5.8. Story forces for HDRB models in the Y direction with DBE-UB parameters

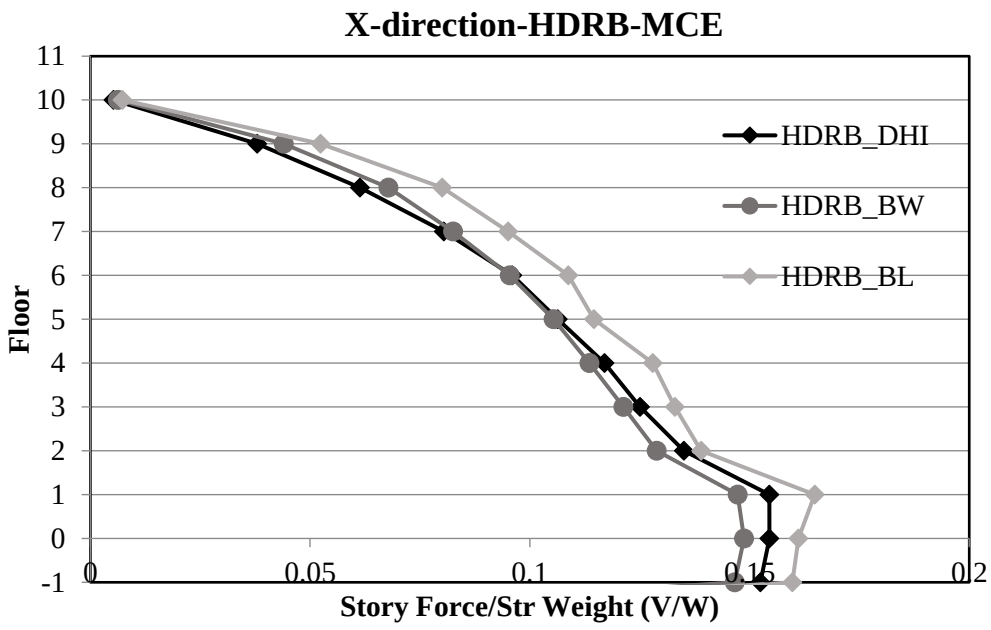


Figure 5.9. Story forces for HDRB models in X direction with MCE-LB parameters

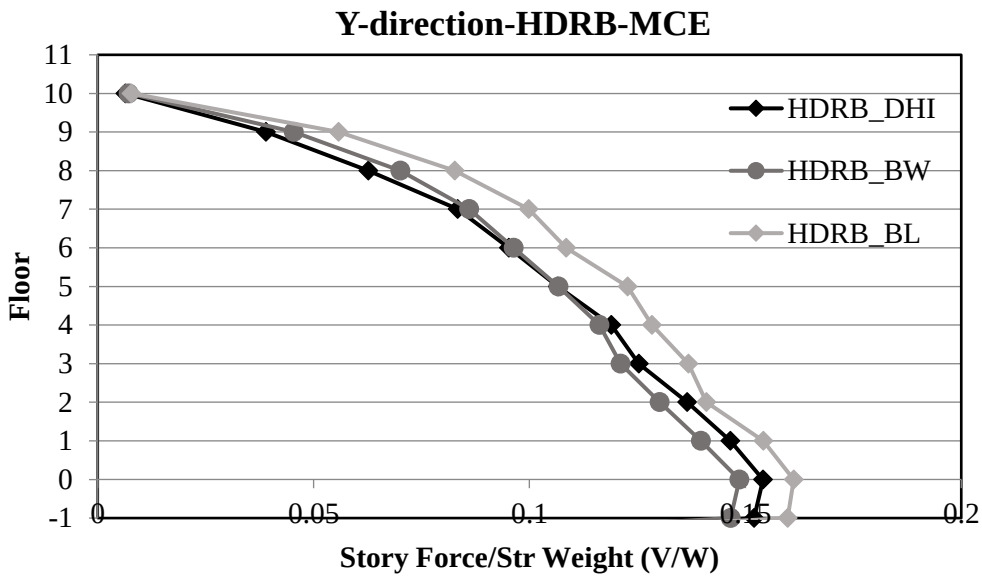


Figure 5.10. Story forces for HDRB models in Y direction with MCE-LB parameters

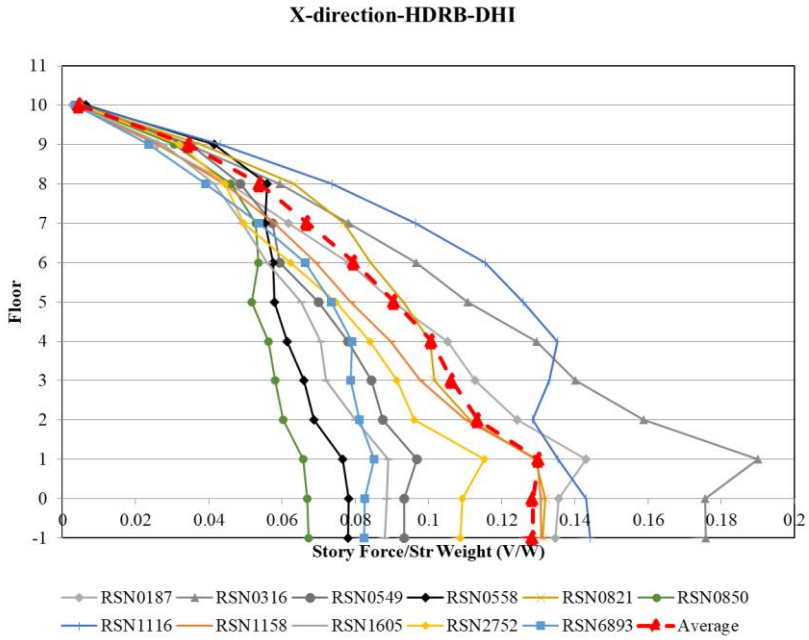


Figure 5.11. Story forces of each motion for HDRB-DHI model in X direction with DBE-UB parameters

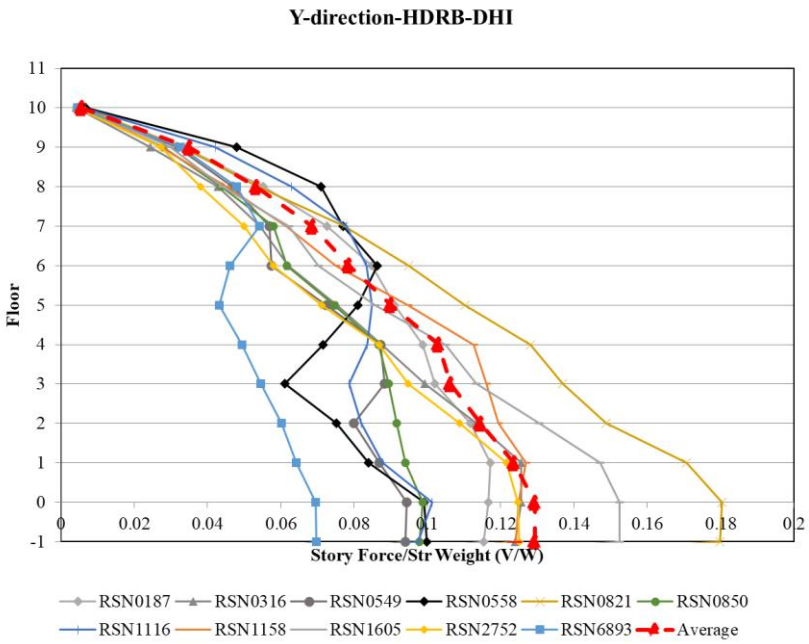


Figure 5.12. Story forces of each motion for HDRB-DHI model in Y direction with DBE-UB parameters

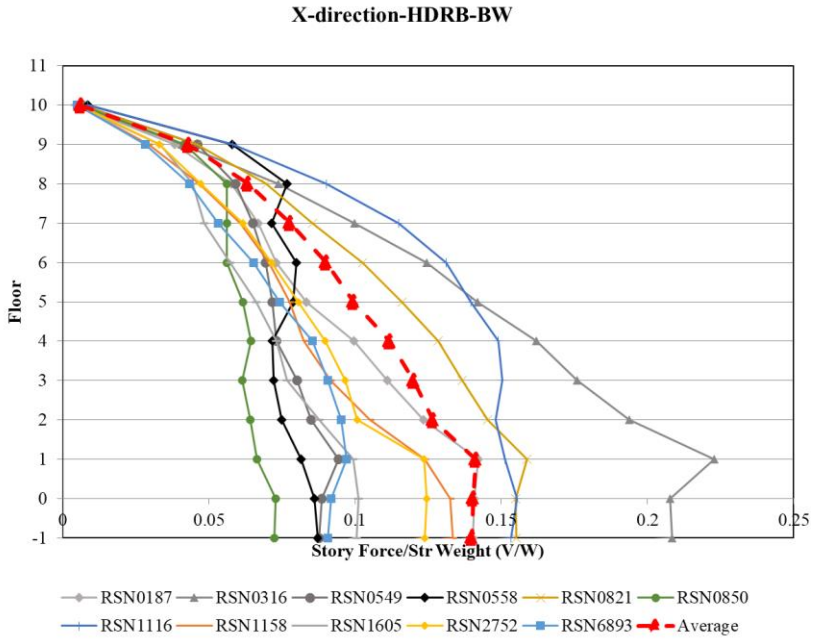


Figure 5.13. Story forces of each motion for HDRB-BW model in X direction with DBE-UB parameters

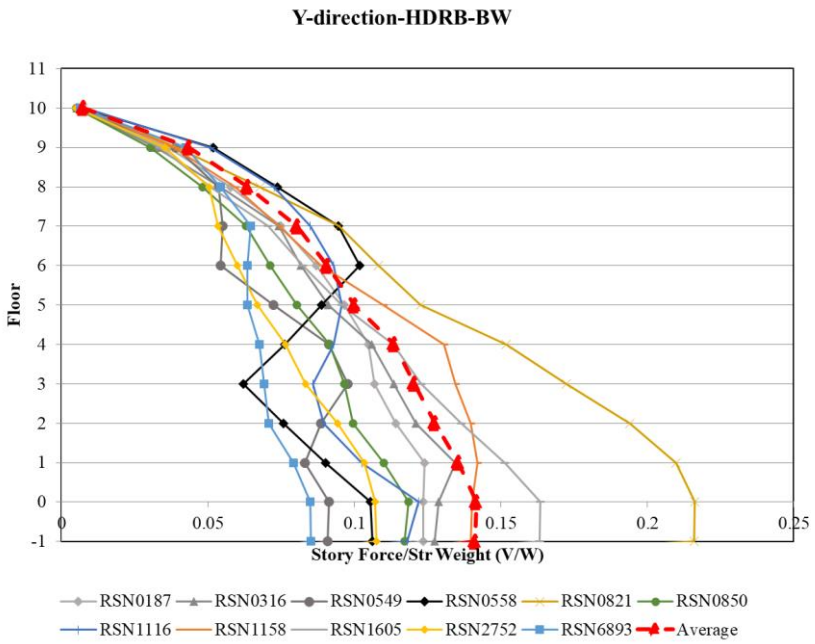


Figure 5.14. Story forces of each motion for HDRB-BW model in Y direction with DBE-UB parameters

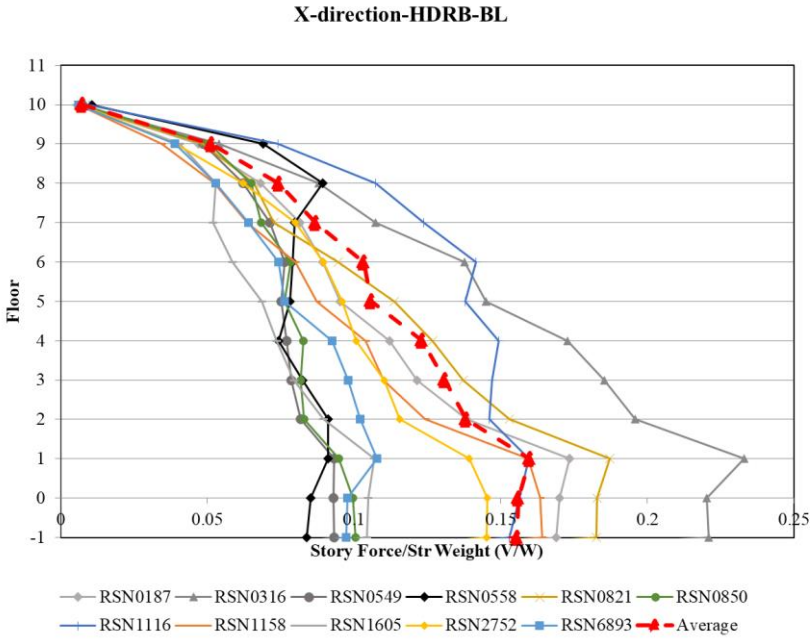


Figure 5.15. Story forces of each motion for HDRB-BL model in X direction with DBE-UB parameters

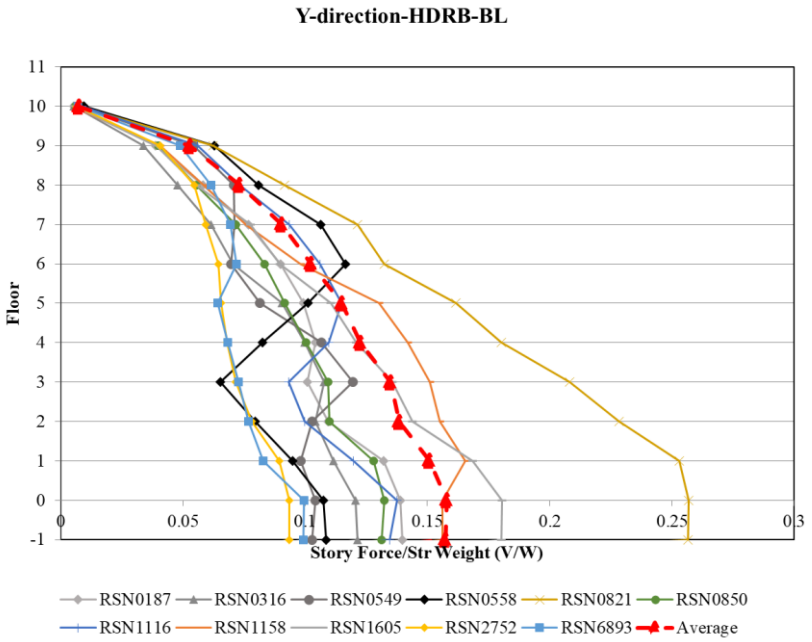


Figure 5.16. Story forces of each motion for HDRB-BL model in Y direction with DBE-UB parameters

For FPS isolators, the average story force distributions in X and Y directions are shown in Figure 5.17 and Figure 5.18, respectively. There is significant overestimation of the response when sharp BL model is used. The force distribution for each earthquake is given from Figure 5.21 to Figure 5.34 for the FPS models for DBE-UB conditions. In some of the ground motions, amplification of the forces at Floor 1 is significant for both models, especially in the X direction.

The average forces for MCE level earthquake is assessed in Figure 5.19 and Figure 5.20. This time, lower demands are attained from BL for the first three stories, and higher for the upper stories. During a seismic motion for the FPI model, shear forces on the isolators, located nearby the shear walls, increases enormously for small amount of time due to the high axial load dependency. It might have effects on the absolute peak response. This phenomenon cannot be observed in the BL model since axial and lateral degrees of freedom are not coupled.

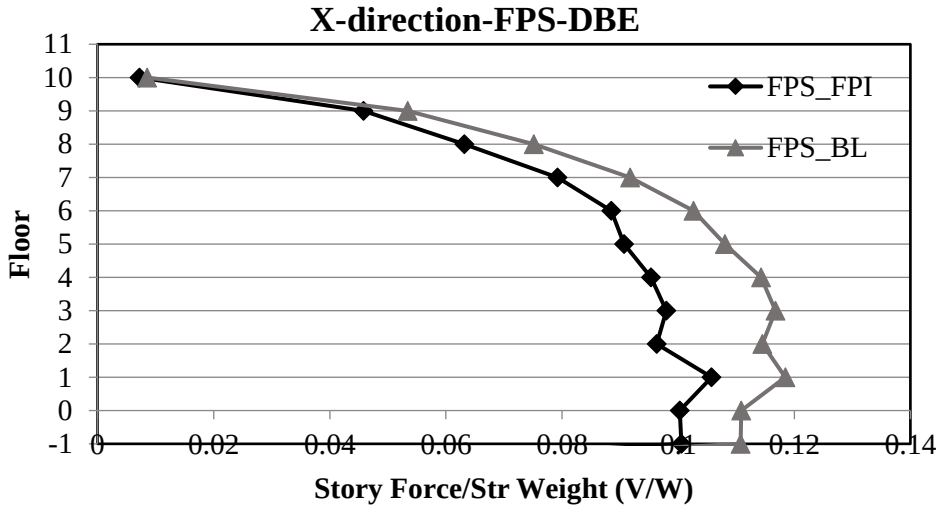


Figure 5.17. Story forces of each motion for FPS models in the X direction with DBE-UB parameters

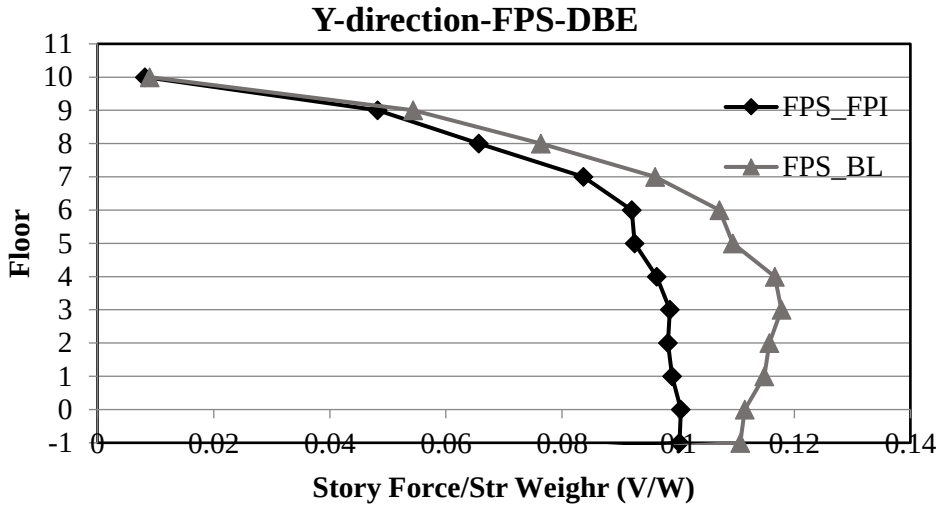


Figure 5.18. Story forces of each motion for FPS models in the Y direction with DBE-UB parameters

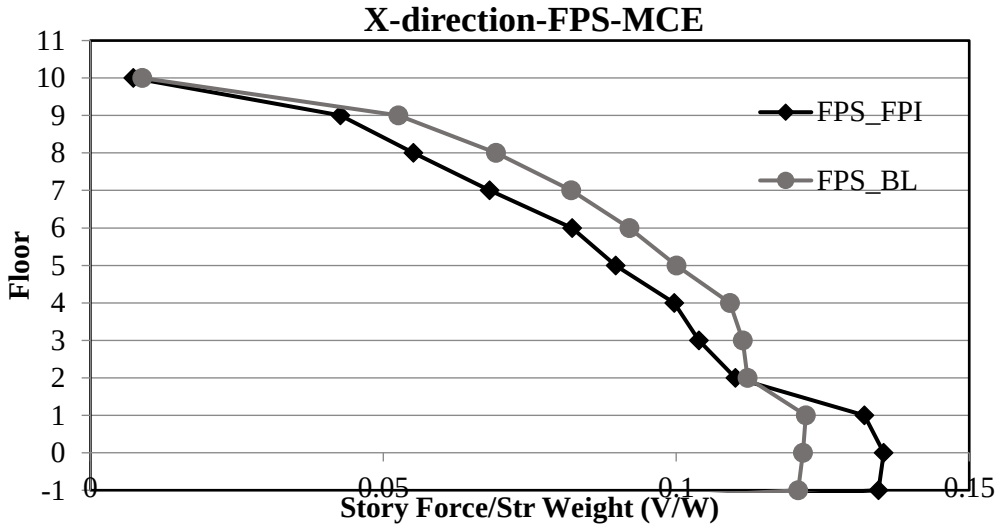


Figure 5.19. Story forces of each motion for FPS models in the X direction with MCE-LB parameters

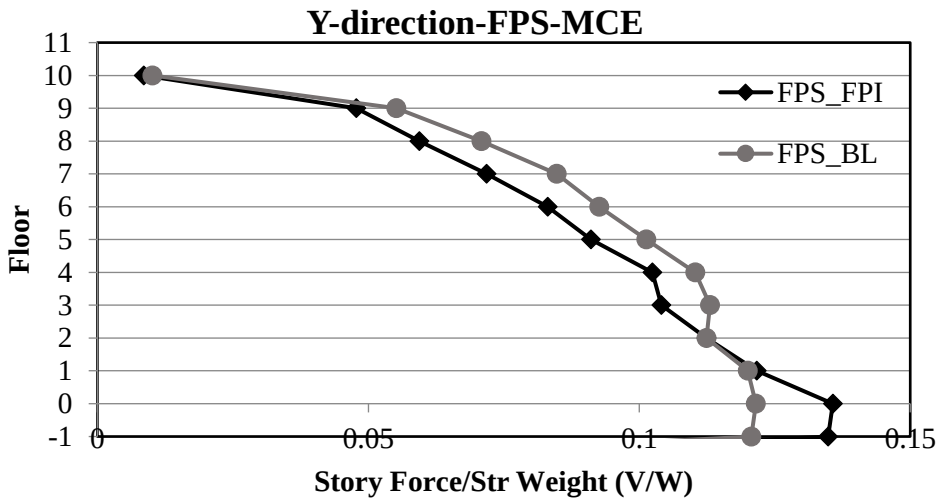


Figure 5.20. Story forces of each motion for FPS models in the Y direction with MCE-LB parameters

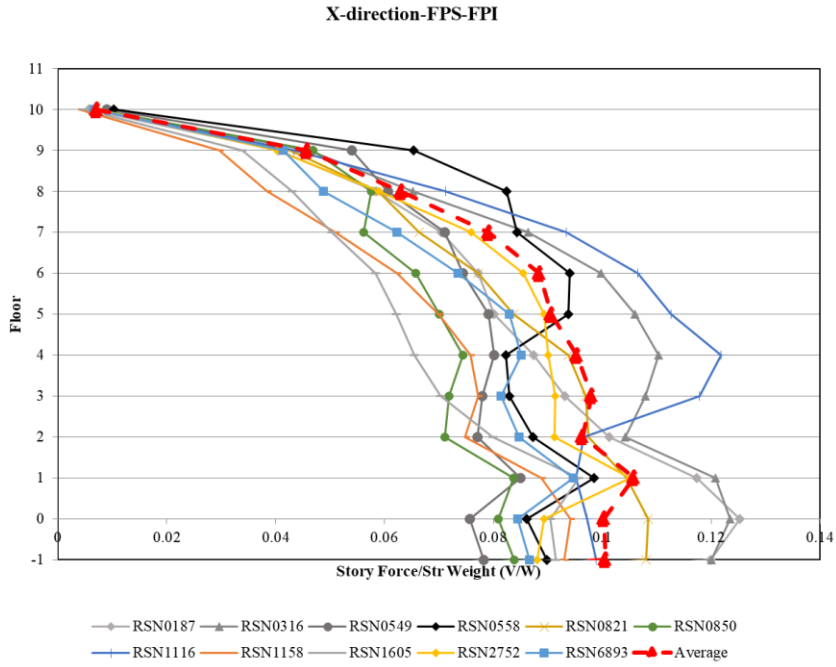


Figure 5.21. Story forces of each motion for FPS-FPI model in the X direction with DBE-UB parameters

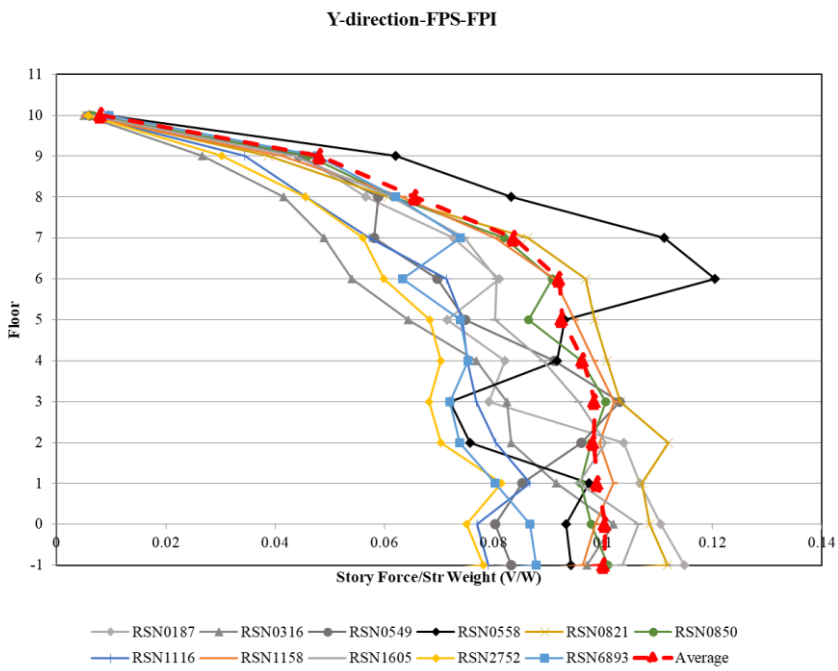


Figure 5.22. Story forces of each motion for FPS-FPI model in Y direction with DBE-UB parameters

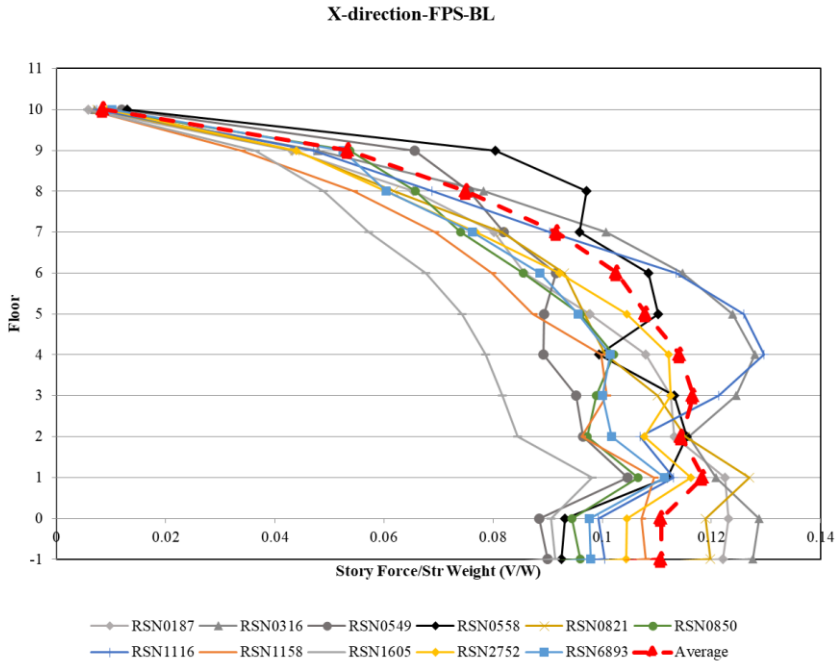


Figure 5.23. Story forces of each motion for FPS-BL model in X direction with DBE-UB parameters

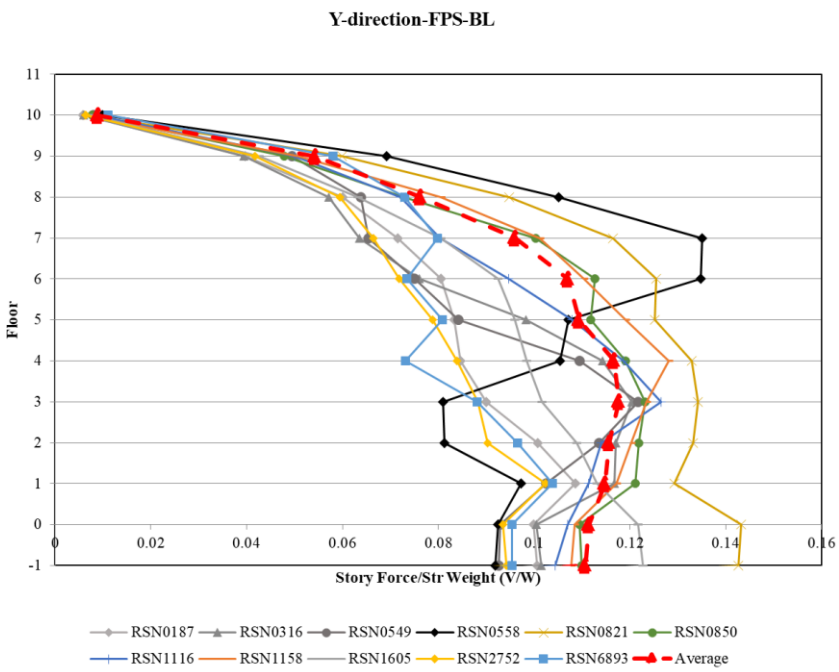


Figure 5.24. Story forces of each motion for FPS-BL model in Y direction with DBE-UB parameters

The average base shear coefficients (V/W) for HDRB models under DBE-UB parameters are compared in Table 5.3. From the bottom of the first floor, the shear forces transferred to the superstructure (V/W) are 13.0% and 12.4% of the structural weight for the DHI model for X and Y directions, respectively. When the bilinear models are used, the results are overestimated by approximately 10% and 20% for BW and BL models, respectively.

The average base shear coefficients for FPS models are compared in Table 5.4. The forces transferred to the superstructure are obtained as 10.6% and 9.9% of the structural weight for the FPI model for the two directions, respectively. The corresponding results were overestimated and obtained as 11.8% and 11.5% by the BL model.

Table 5.3 Average base shear coefficient comparison of HDRB models

| W=499727 | **Vx/W** | **Vy/W** |
|---|---|---|
| **DHI** | 0.130 | 0.124 |
| **BW** | 0.141 | 0.136 |
| **BL** | 0.160 | 0.151 |

Table 5.4 Average base shear coefficient comparison of FPS models in X-dir

| W=499727 | **Vx/W** | **Vy/W** |
|---|---|---|
| **FPI** | 0.106 | 0.099 |
| **BL** | 0.118 | 0.115 |

## 5.3 Story Accelerations

The maximum floor accelerations for each earthquake were obtained from the analysis program, and the average of 11 ground motions was calculated. As specified in TBDY2019, the resulting accelerations were evaluated from the design basis earthquake (DBE) results with nominal isolator properties. The results are shown in graphical forms. First floor is located at 0.00 elevation in the figures, and the isolation level is at -4.5 m. The basement floor where pedestal columns are present is located at -4.50 m elevation. The average of the peak ground accelerations of eleven ground motions is approximately observed on the basement floor.

Due to the contribution of the higher modes, it was observed that the accelerations could significantly increase in the upper floors. Özdemir (2010) and Erdik et al. (2018) states that relatively tall and flexible structures on the isolators may experience relatively higher floor accelerations.

Figure 5.25 and Figure 5.26 compare the average of maximum floor accelerations of 11 ground motions for HDRB models in the X and Y directions, respectively. The DHI model yielded the lowest accelerations. Nearly 0.2 g until Floor 8 and 0.27 on Floors 9 and 10. Therefore the results of the DHI model are less than 0.3 g on all floors and satisfy the performance criteria. It is followed by the smooth BW model of up to 30% higher response than the DHI. The sharp BL model yields the highest response and shows significant amplification on the isolation floor.

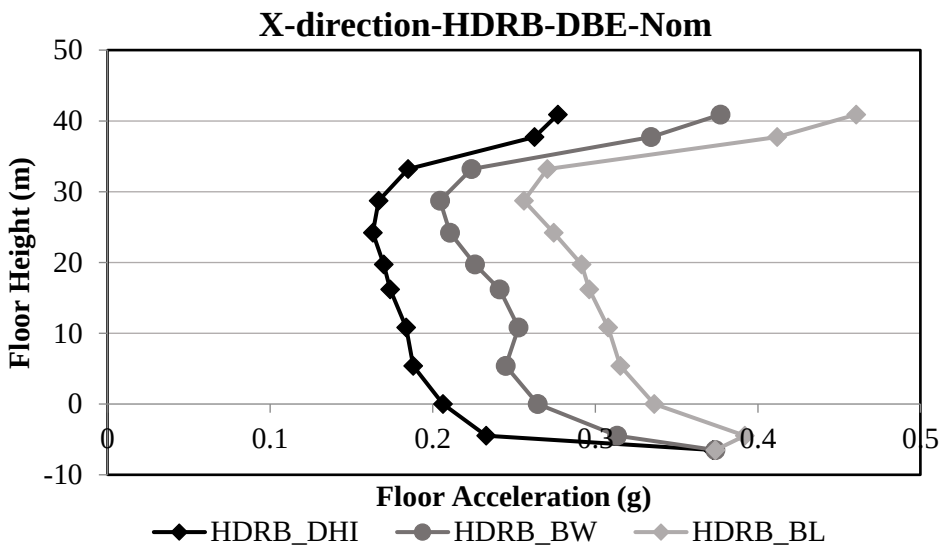


Figure 5.25. Ave. floor accelerations of eleven motions for HDRB in X direction

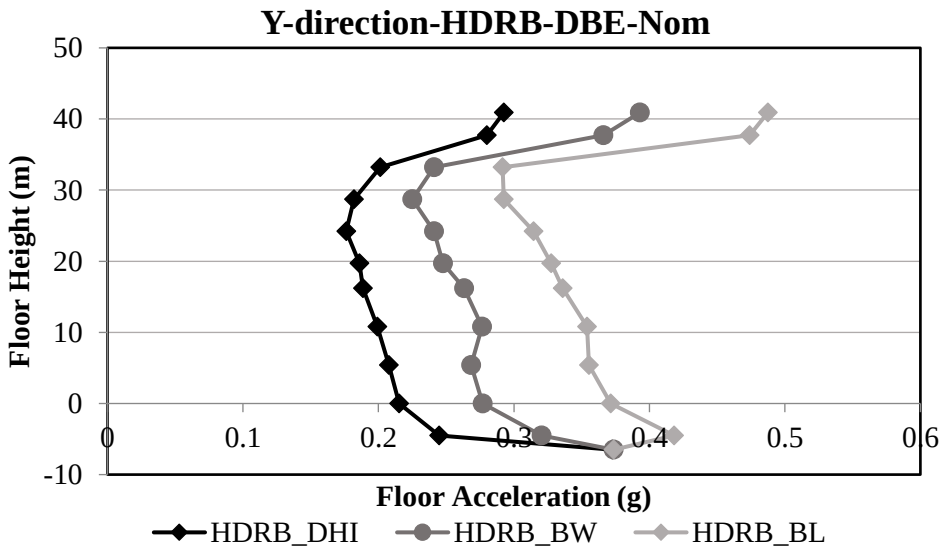


Figure 5.26. Ave. floor accelerations of eleven motions for HDRB in Y direction

Figure 5.27 and Figure 5.28 compare the average of maximum floor accelerations of 11 ground motions for FPS models in the X and Y directions, respectively. The FPI model resulted in accelerations between 0.27 g and 0.37 g in the first nine floors and increased to 0.44 g on the top floor. Moreover, the sharp BL model showed results up to 40% higher than the FPI model. Similar to the HDRB-BL model, acceleration

amplification was observed on -4.5 m elevation (isolation floor) in most ground motions.

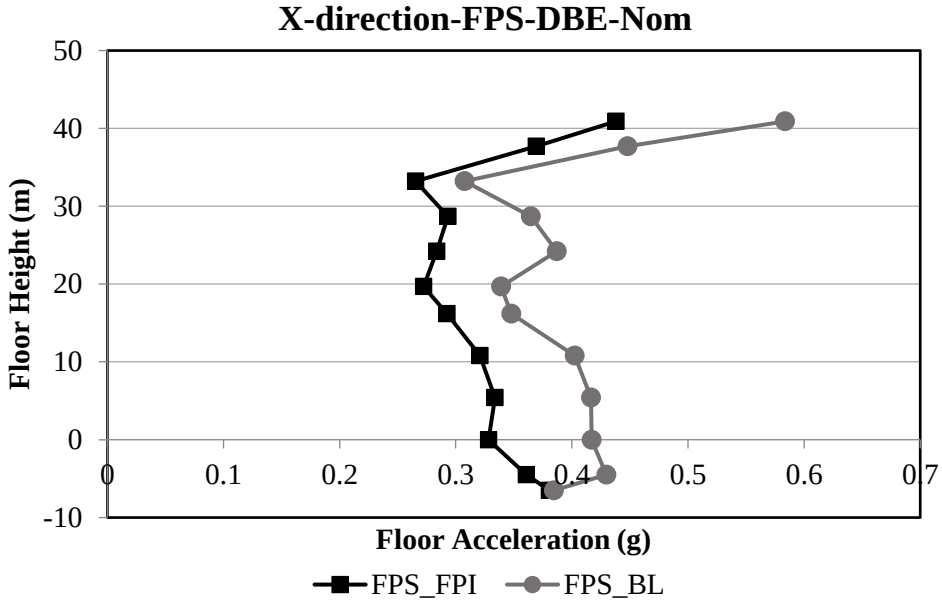


Figure 5.27. Ave. floor accelerations of eleven motions for FPS in X direction

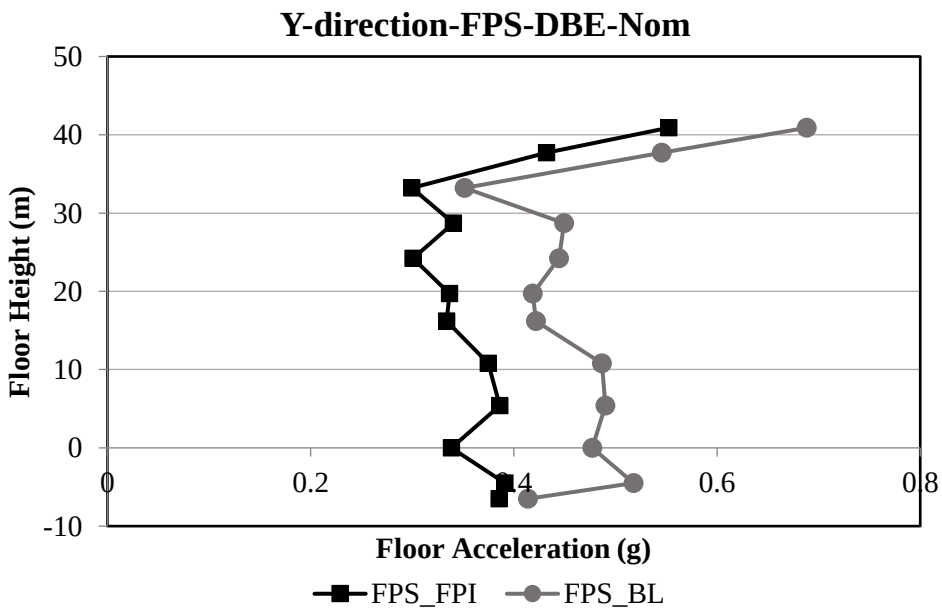


Figure 5.28. Ave. floor accelerations of eleven motions for HDRB in Y direction

The differences in the acceleration results are noticeable when idealized bilinear models are adopted instead of more accurate nonlinear models. As an additional example, analysis results of MCE level earthquakes with lower bound isolator parameters are investigated. The average acceleration results from MCE-LB are presented in Figure 5.29 and Figure 5.30 for both directions. Accelerations on the isolation level decrease in MCE analysis as one expects from an isolation system. However, the sharp BL model still shows significantly higher responses.

For this building, relatively high accelerations are obtained. In an isolated building, one can expect isolation floor accelerations are closer to the base shear coefficient, i.e. 10-12% in this study. However, there is more than one reason for this problem. First, DBE isolator periods of both designs are close to the fixed-based period. Optimization in the FPS design could allow the isolation system to be flexible and to obtain a less structural response. On the other hand, the shear strain and uplift limitations for HDRB isolators reduce the design alternatives and might result in a costly rubber isolation system.

Second, especially for FPS isolators, a higher damping ratio in DBE conditions might be associated with activation of the higher modes which yields higher superstructural response (Warn & Ryan, 2012). These can also be combined with the sharp stiffness transitions in BL models, also activating the higher modes (Mavronicola, 2017).

Another reason is that the structure is not symmetrical and more slender at the corner locations and prone to significant demands under bilateral excitation. It is investigated in a previous study with the same model but different earthquakes. Three different locations from the building were selected and average accelerations of 7 ground motions are compared under a DHI-DBE-Nom model with the maximum results. The results are given in Appendix B. The locations far from the structural center and at more slender regions experience higher accelerations and become dominant when the peak accelerations are obtained from the software.

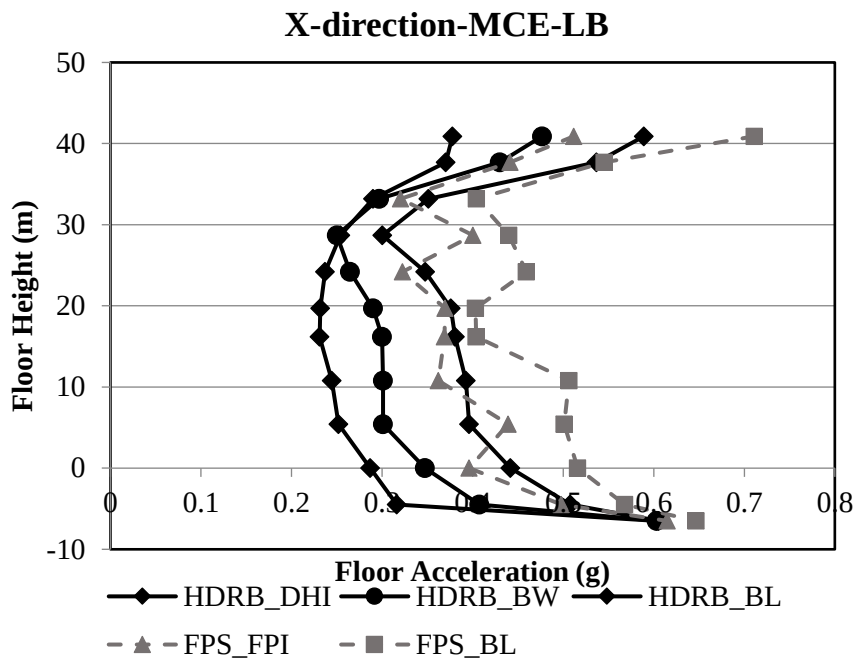


Figure 5.29. Ave. floor accelerations of eleven motions for MCE in X direction

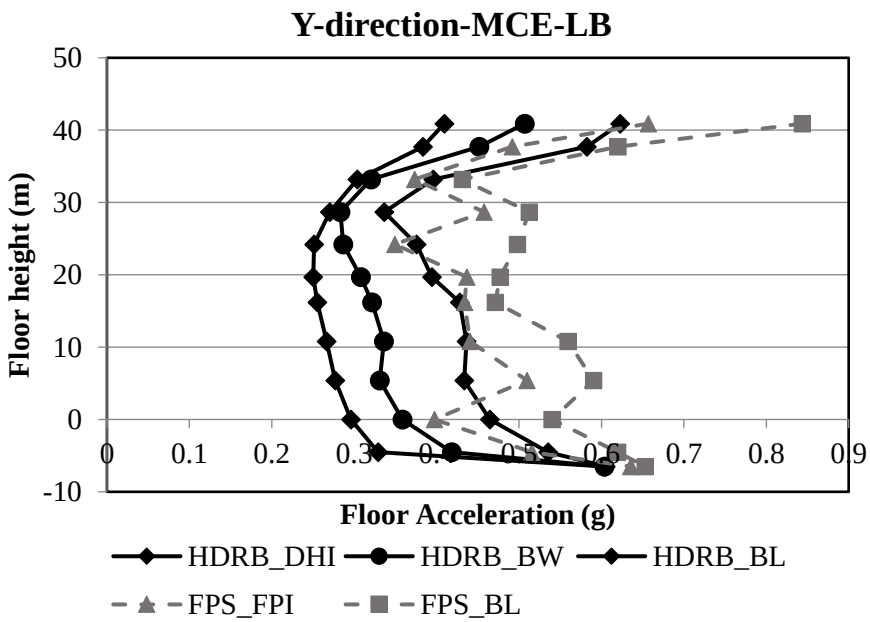


Figure 5.30. Ave. floor accelerations of eleven motions for MCE in Y direction

Average accelerations from different elevations of the building are compared. The top floor, isolation floor and peak ground accelerations (PGA) of HDRB models are given in Table 5.5. The BW model estimates the accelerations approximately %35 higher than the DHI model. On the other hand, the increase in BL model is between 65-70% when compared the DHI model. On the isolation floor, the sharp BL model yielded values higher than the PGA.

Table 5.5 Ave. accelerations of the top floor, isolation floor, and the PGA for HDRB

| **Average Acc (g)** | **DHI** | | **BW** | | **BL** | |
|---|---|---|---|---|---|---|
| | **X** | **Y** | **X** | **Y** | **X** | **Y** |
| **Top floor** | 0.277 | 0.293 | 0.377 | 0.393 | 0.461 | 0.487 |
| **Iso floor** | 0.233 | 0.245 | 0.313 | 0.320 | 0.392 | 0.418 |
| **PGA** | 0.380 | | | | | |

The top floor, isolation floor and peak ground accelerations of FPS models are shown in Table 5.6. The sharp BL model shows increased accelerations by 20- 30% when compared to the FPI model. The FPI model yields accelerations that are close to the PGA in both top and isolation floors.

Table 5.6 Ave. accelerations of the top floor, isolation floor, and the PGA for FPS

| **Average Acc (g)** | **FPI** | | **BL** | |
|---|---|---|---|---|
| | **X** | **Y** | **X** | **Y** |
| **Top floor** | 0.438 | 0.553 | 0.583 | 0.688 |
| **Iso floor** | 0.361 | 0.391 | 0.430 | 0.518 |
| **PGA** | 0.380 | | | |

## 5.4 Inter-story Drifts

To compare the inter-story drifts, maximum story drifts were obtained under DBE seismic level with nominal isolator properties. The average of the maximum values for each floor was calculated to assess according to the TBDY2019. In the code, the superstructural drifts shall be below 0.005 drift ratio for non-structural damage limitation.

For each HDRB model, the average inter-story drift ratio is shown in Figure 5.31 and Figure 5.32, for X and Y directions, respectively. The DHI model resulted in least drifts less than 0.55 % for all stories. Furthermore, there is an approximately 10% higher story drift in the BW when compared to the DHI model. Also, the highest drifts were attained in BL model, nearly 20% higher than the DHI. From the figures, it can be seen that the bilinear models could overestimate the response significantly.

For the selected FPS isolator models, the superstructural drift response is introduced in Figure 5.33 and Figure 5.34 for X and Y directions, respectively. Similar to the HDRB case, the isolator model that induces higher nonlinearity in the hysteresis of FPI brought lower response. When the sharp BL model is used, an overestimation in the response is observed in all floors.

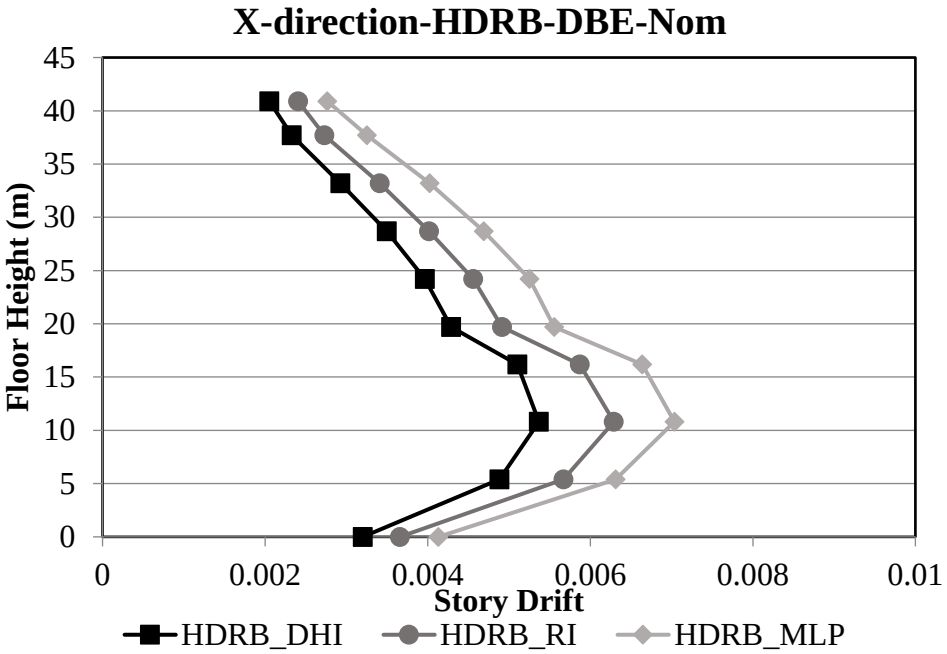


Figure 5.31. Ave. story drifts of eleven motions for FPS in X direction

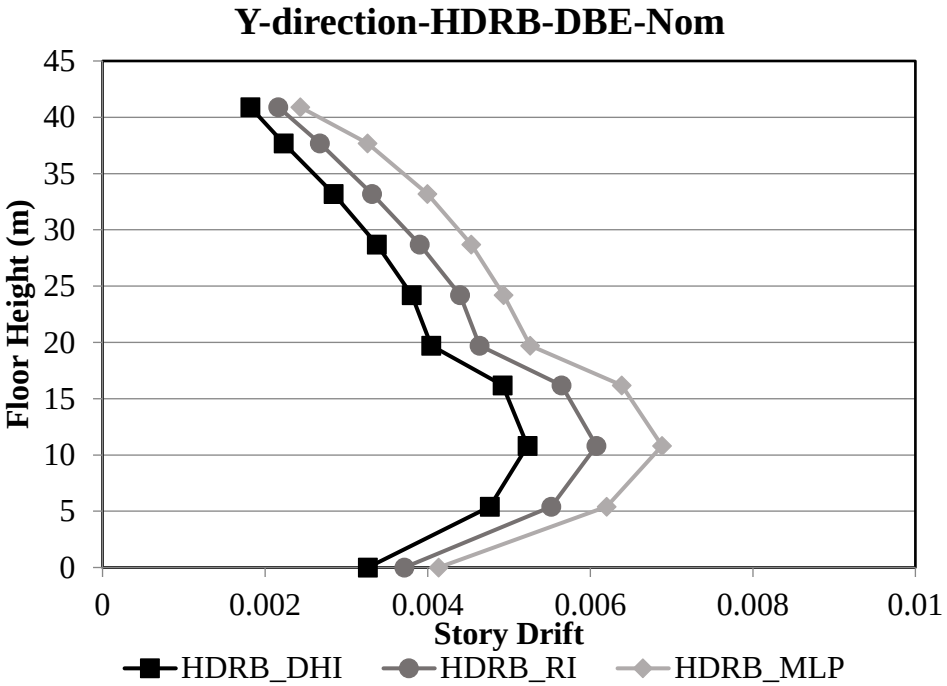


Figure 5.32. Ave. story drifts of eleven motions for HDRB in Y direction

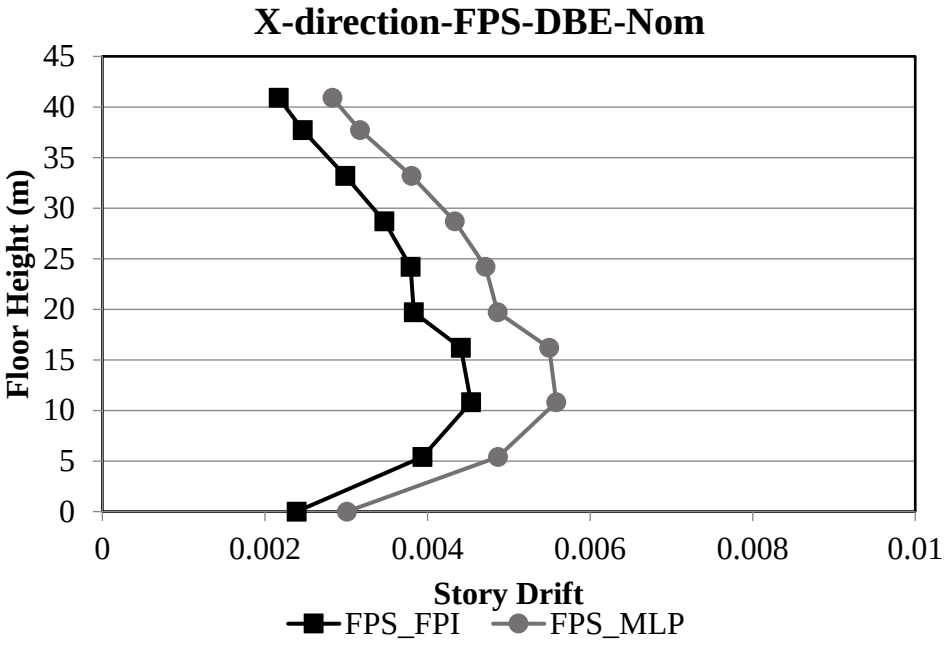


Figure 5.33. Ave. story drifts of eleven motions for FPS in the X direction

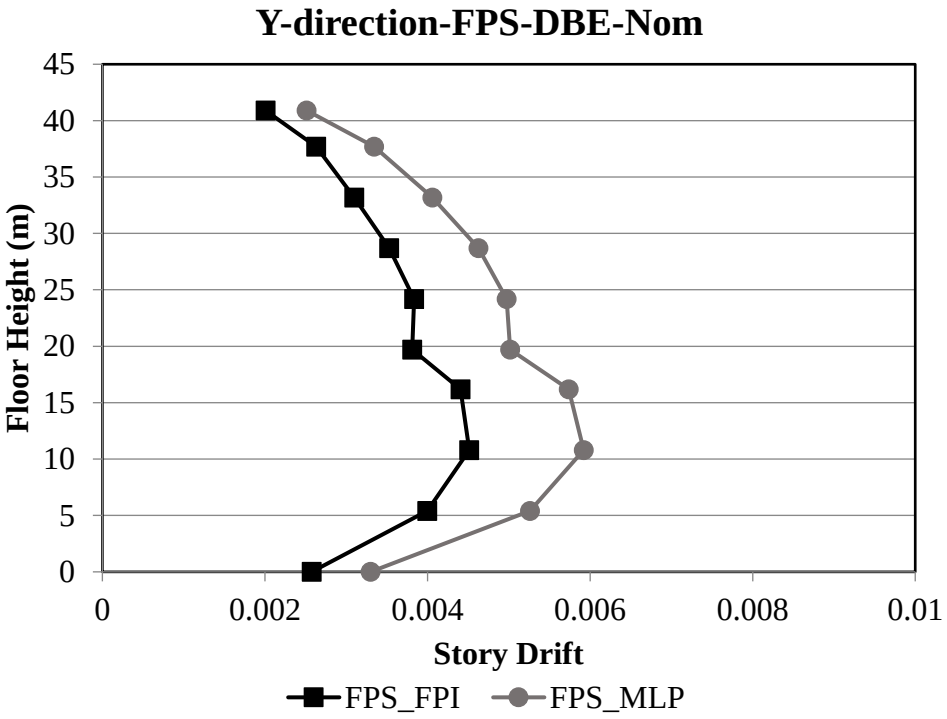


Figure 5.34. Ave. story drifts of eleven motions for FPS in the Y direction

## 5.5 Isolator Hysteresis Curves

The fundamental difference between various isolator models is the hysteresis behavior that they will follow. Almost all performance parameters are affected by the characteristics of the hysteresis curves. Adequacy of the bilinear models is evaluated by comparing the hysteresis response for selected isolators and under MCE seismic level with LB isolator properties. Isolators were chosen according to their axial load variations and locations. The rotational effects of the isolators far from the stiffness center are more significant, and the coupled directional behavior of isolators is visible.

Behavior of the DHI model is shear strain dependent. Therefore, the nonlinear stiffness is recalculated at each time step and continuously varies throughout the seismic motion. There is also a considerable stiffness increase when the shear strain exceeds 200%, which adds damping and diverges from a bilinear behavior. However, the smoothed BW and sharp BL models' hysteresis behavior were constructed using the preliminary analysis by Equivalent Lateral Force Procedure (ELFP). The same comments can be made for FPS modeling approaches as there is no coupling of axial and horizontal degrees of freedoms in the BL model, unlike the FPI model. The idealized stiffnesses and the maximum displacement limit the nonlinear behavior. Thus, these bilinear models cannot accurately capture the behavior when the peak displacement for a specified ground motion is well below or above the design displacement obtained by ELFP. To evaluate this phenomenon, the hysteresis behaviors of isolators are compared using several ground motions, which yield different maximum displacements. In this section, the ground motions which result in closer displacements to the design value are investigated. The HDRB and FPS designs are examined under the ground motions RSN2752 (Chi-Chi_Taiwan-04, 1999) and RSN1158 (Kocaeli_Turkey, 1999), respectively. Furthermore, the hysteretic response under RSN316 (Westmorland, 1981) and RSN558 (Chalfant Valley-02, 1986), which show the highest and the lowest displacement responses,

respectively, are shown in Appendix C, and the differences between the DHI and bilinear models are more observable.

Three isolators were chosen to compare the hysteresis curves of different models. The selected isolators are shown on the isolation layout in Figure 5.35. In the figure, the Iso1 is located under a column, close to the structural center and far from the shear walls; therefore, the high axial load variation is not observed, and bidirectional effects are minimized. The Iso2 is located under a column, right side of the bottom edge of the building; thus, the effect of overturning moments in the X direction (i.e., aspect ratio) due to seismic excitation is apparent in the hysteresis curves. Finally, the Iso3 is positioned under a shear wall at the right corner; therefore, the response is affected by the rocking motion of the shear wall.

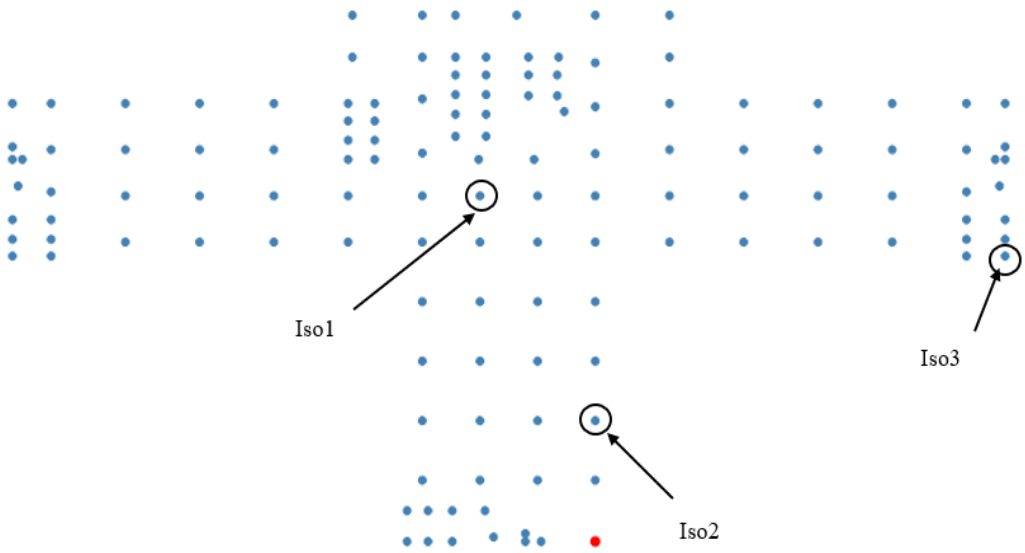


Figure 5.35. The selected isolator locations to compare hysteretic response (the isolator layout is retrieved from ETABS plugin by Ulker Eng.)

The comparison for HDRB models is conducted for Chi-Chi_Taiwan-04 (RSN2752) ground motion. Figure 5.36 and Figure 5.37 present the comparison for the Iso1 in X and Y directions, respectively. All models show a stable hysteresis loop in the X direction, and each model's compatibility is almost achieved. On the other hand, the effect of bidirectional coupling is more noticeable in the Y direction. Therefore, DHI and BW models yield a significant degredation in the hysteresis curves and less energy dissipation in the positive direction. When the isolators are moving in the positive direction, bidirectional effects excites forces in the opposite direction. This results in a reduced horizontal demands in the DHI and BW models and disagreement in the response for each model is observed. The maximum forces and the least displacements are obtained from the BL approach in both directions as there is no change in the hysteretic parameters until the peak force for each cycle is achieved and no coupling of the degrees of freedom. Similar conclusions can be drawn for Iso2 and Iso3, given from Figure 5.38 to Figure 5.41, with only minor changes in forces and displacements.

It should be noted that the axial and horizontal degrees of freedom are uncoupled in all HDRB models considered. Therefore the effect of the axial force variation due to the shear walls and vertical ground motion components are not reflected in the results. However, the isolators were designed to bear the maximum compression and tensile stresses. Furthermore, the uplift displacements are investigated in Section 5.6 and the stability of the bearings is satisfied by the limits from the literature.

The figures in Appendix C are also assessed and show that the DHI model shows increasing stiffness and energy dissipation after 200% shear strain (0.4 m displacement) under a high earthquake intensity (Westmorland, 1981). It results in disagreement with the idealized bilinear models. Furthermore, although the bilinear BW and BL models could accurately capture the displacement response, they overpredict the forces when compared to the DHI model in the earthquake with the lowest maximum displacement (Chalfant_Valley_02, 1986).

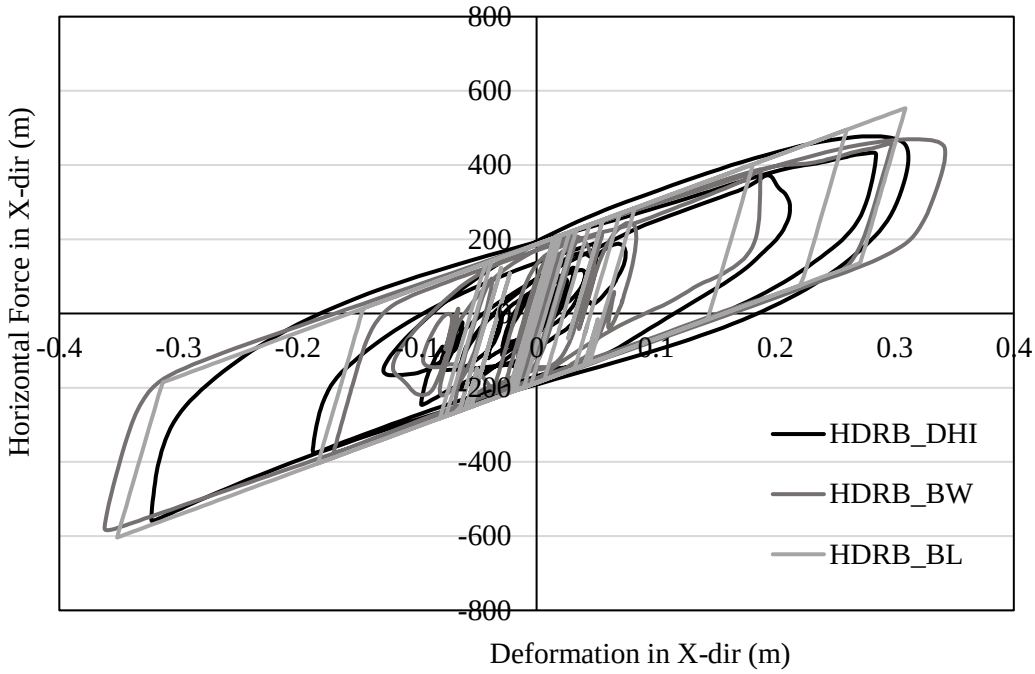


Figure 5.36. Hysteresis of Iso1 links for ChiChi2752 ground motion for X direction

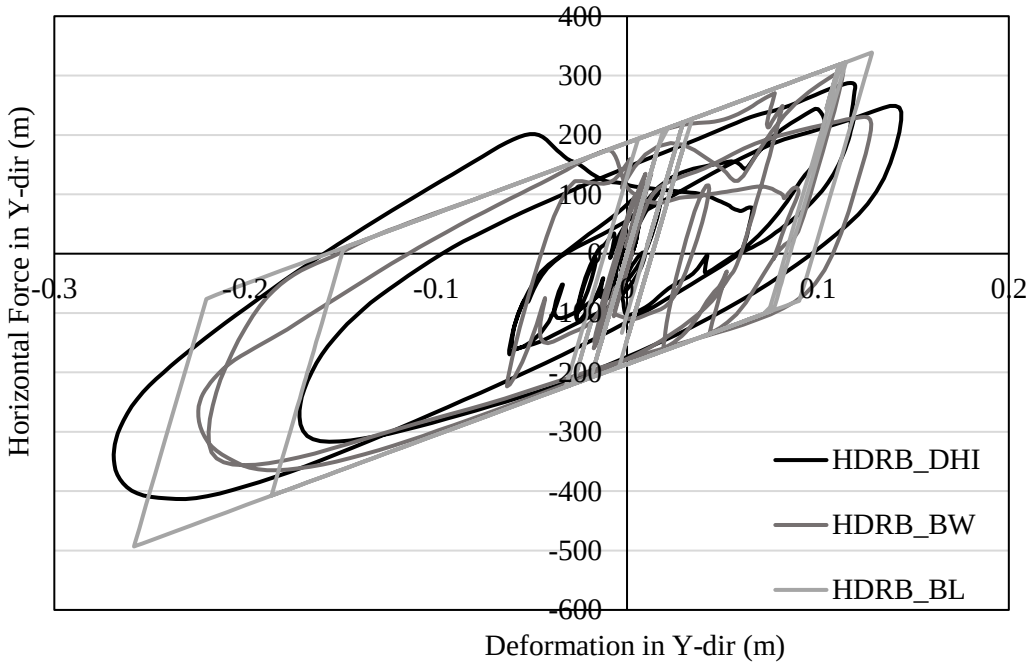


Figure 5.37. Hysteresis of Iso1 link for ChiChi2752 ground motion for Y direction

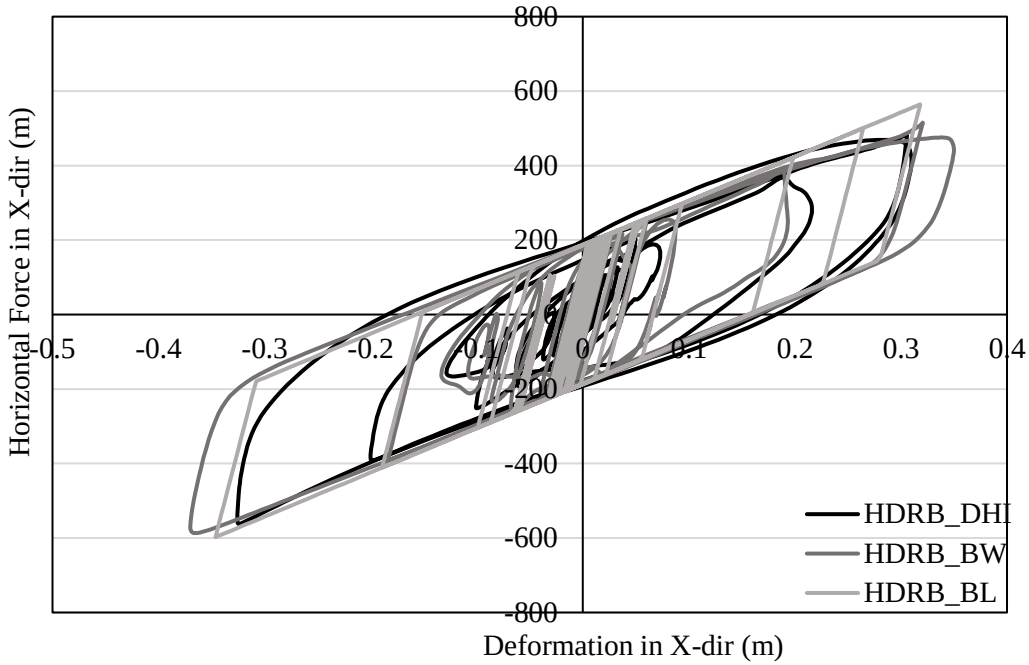


Figure 5.38. Hysteresis of Iso2 link for ChiChi2752 ground motion for X direction

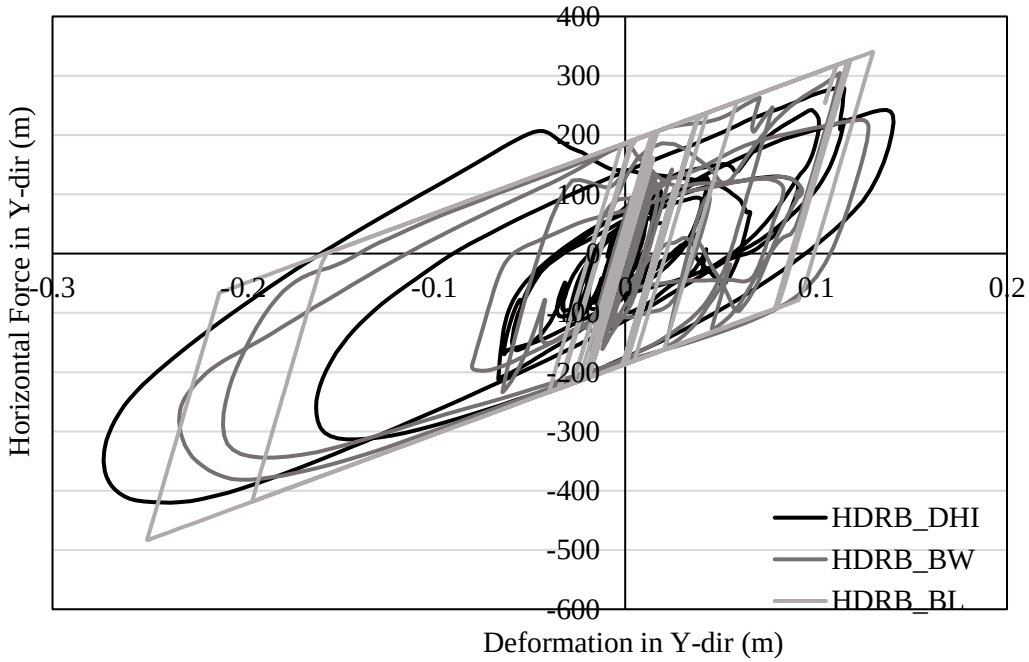


Figure 5.39. Hysteresis of Iso2 link for ChiChi2752 ground motion for Y direction

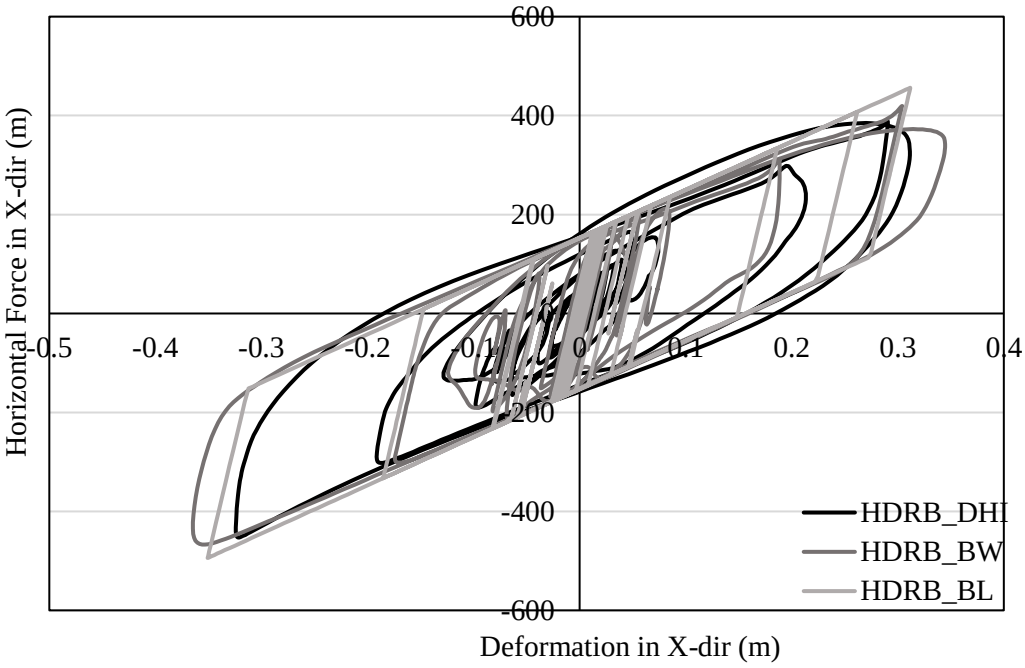


Figure 5.40. Hysteresis of Iso3 link for ChiChi2752 ground motion for X direction

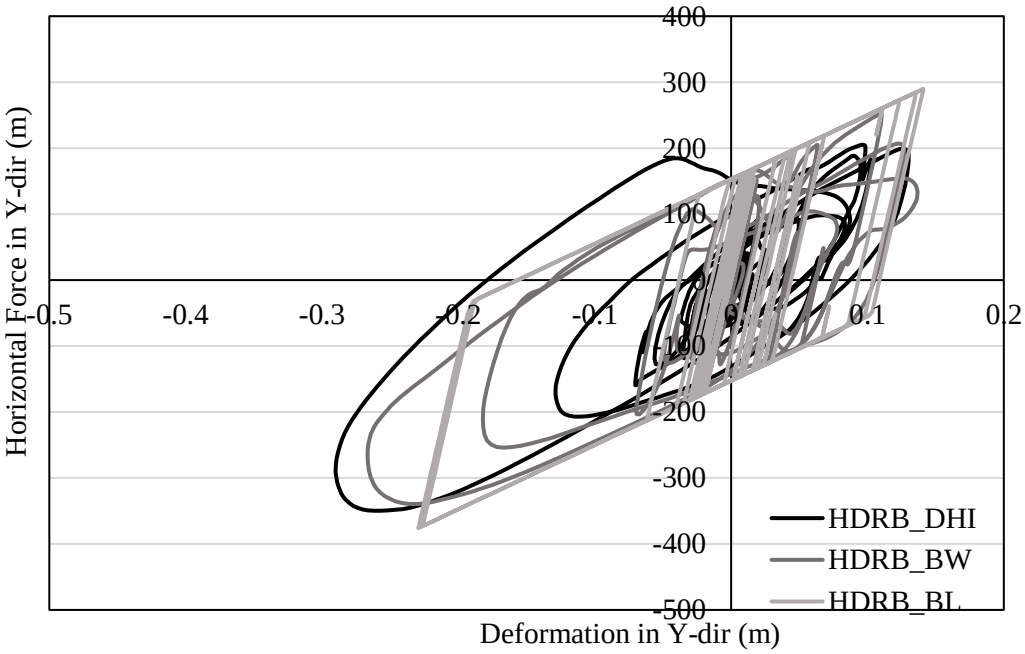


Figure 5.41. Hysteresis of Iso3 link for ChiChi2752 ground motion for Y direction

The comparison for FPS models is conducted for Kocaeli, 1999 (RSN1158) ground motion. The axial load histories of selected links are shown in Figure 5.42 for only the FPI model; therefore, the uplift behavior can be explicit for the reader. The Iso1 and Iso2 did not experience any uplift, unlike the Iso3, which undergoes uplifting many times under a shear wall during the seismic motion. Since the Iso2 is located at the edge of the building, it is subjected to considerable overturning moments. Thus, the axial load variation of this link is high compared to Iso1. Furthermore, the effect of the vertical ground motion component should not be forgotten since it also contributes to the variability of the axial loads. Since the vertical and horizontal behavior are not coupled in the sharp BL model, the axial load history graph is not presented here. However, the behavior is similar to the FPI model, with only small increases in the amplitudes.

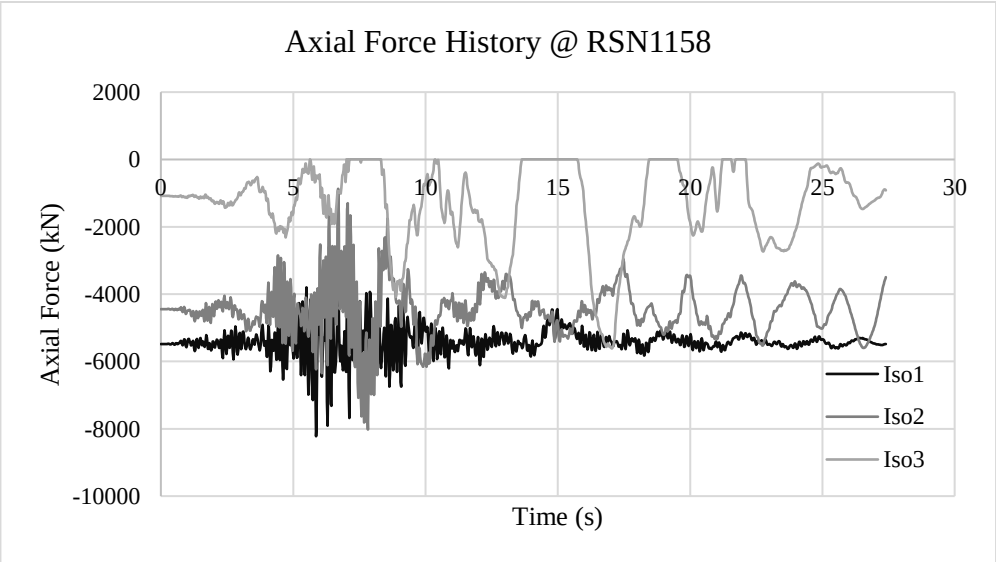


Figure 5.42. Axial load history of selected isolators for Kocaeli1158 ground motion

The horizontal hysteretic responses of the Iso1 are presented in Figure 5.43 and Figure 5.44, for X and Y directions, respectively. Although it is an isolator located close to the stiffness center, the hysteresis curve of the FPI model is shrinking where the model's bidirectional effects are present, especially in the X direction. In the Y direction, a more stable hysteresis is observed. Also, the vertical earthquake component induces oscillations in the nonlinear stiffness in both X and Y directions

since frictional and pendulum resistance is highly dependent on the compressive stresses in the FPI approach. The sharp BL approach can predict the overall response; however there are differences due to its lack of ability to catch the highly nonlinear response.

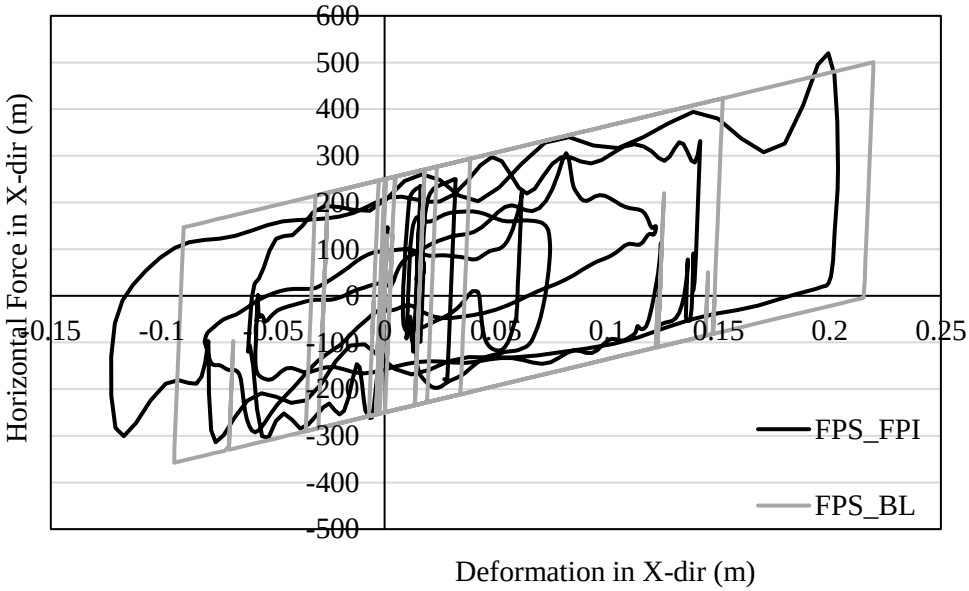


Figure 5.43. Hysteresis of Iso1 link for Kocaeli1158 ground motion for X direction

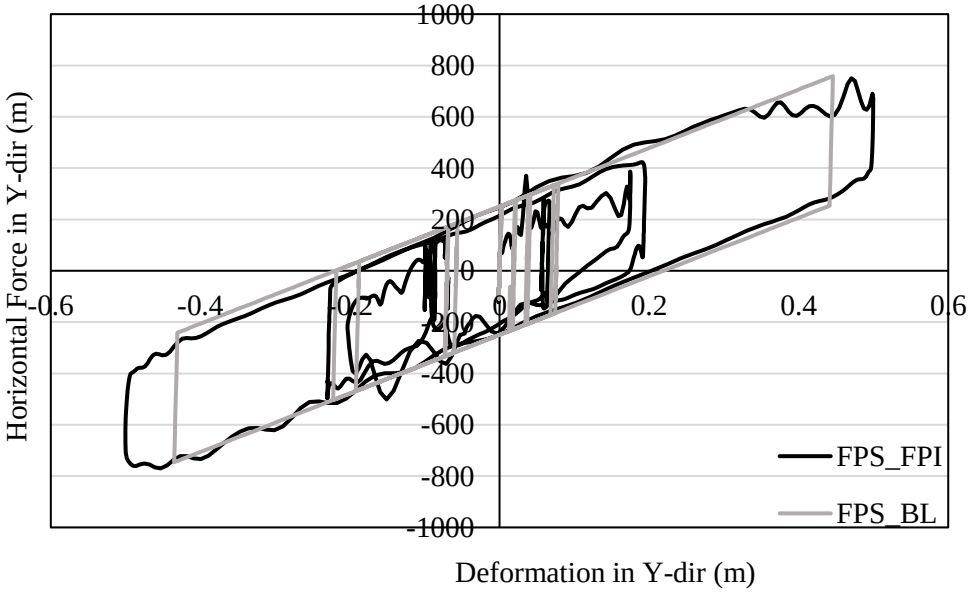


Figure 5.44. Hysteresis of Iso1 link for Kocaeli1158 ground motion for Y direction

The horizontal cyclic force-displacement responses for Iso2, which is located at the edge, are given in Figure 5.45 and Figure 5.46 for X and Y directions, respectively. The bottom extension of the T-shaped building plan sustains relatively higher overturning moments when a seismic excitation in the X direction is applied. In the positive X direction, overturning moments increases compressive stresses on the isolator, and uplift effects for the negative X direction. The product can be seen in Figure 5.45. The hysteresis curve is broader in the positive X direction, when compared to the curve shrinking in the negative direction, decreasing hysteretic damping. It means that higher compressive forces present in the positive direction, increasing the hysteretic damping in this region. As a result, the BL model underpredicts the forces in positive and overpredicts in negative X direction. On the other hand, the directional coupling is higher for the isolator in the Y direction. The BL model's displacement results are considerably lower due to the uncoupled lateral degrees of freedom in the maximum cycle, and the BL model cannot capture the behavior accurately.

In the X and Y directions, the hysteretic responses of Iso3 are given in Figure 5.47 and Figure 5.48. This isolator is placed at the corner of a shear wall, extending in the Y direction and experiencing high tensile and compressive loads (Figure 5.42) due to the rocking motion of the shear wall. Therefore, the seismic action excites tensile forces in the positive Y direction and high compressive demands in the negative Y direction. Because of the significant tensile forces in the axial loads, unstable lateral hysteresis curves were obtained for the FPI model. The sharp BL model results is not comparable with the FPI model for the Iso3.

When the figures given in Appendix C are assessed, there are significant oscillation in the stiffness of the FPI behavior and the BL model cannot capture the behavior under Westmoreland316 earthquake. Similar conclusions can be drawn for the low intensity earthquake. There are also numerical problems observed in the FPI model due to high axial load variability and negative stiffnesses. Iso3, located under the shear wall, experience uplifts with long durations.

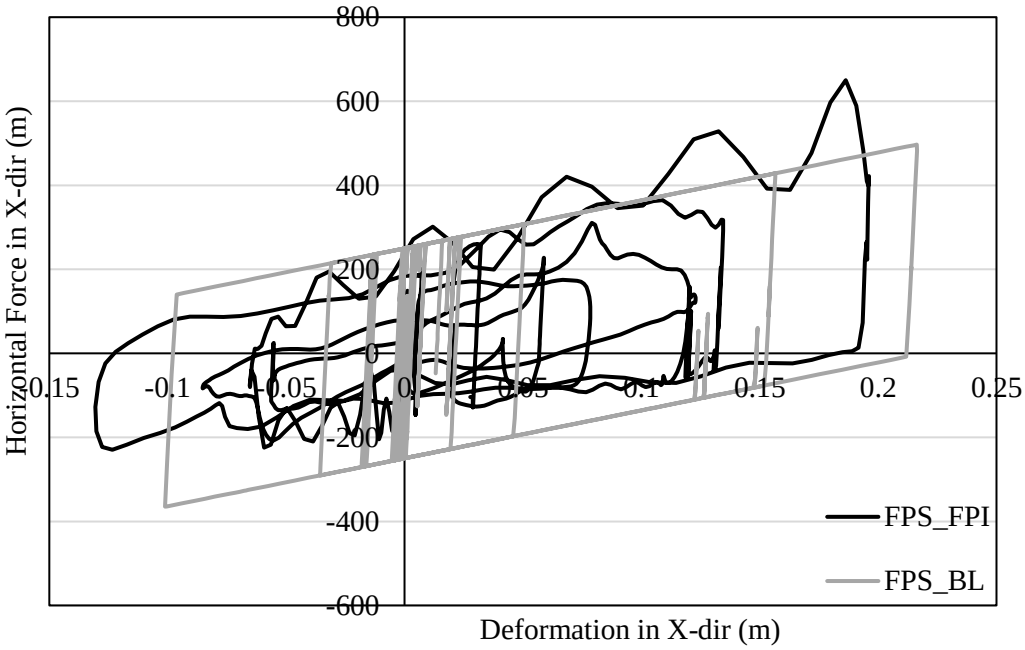


Figure 5.45. Hysteresis of Iso2 link for Kocaeli1158 ground motion for X direction

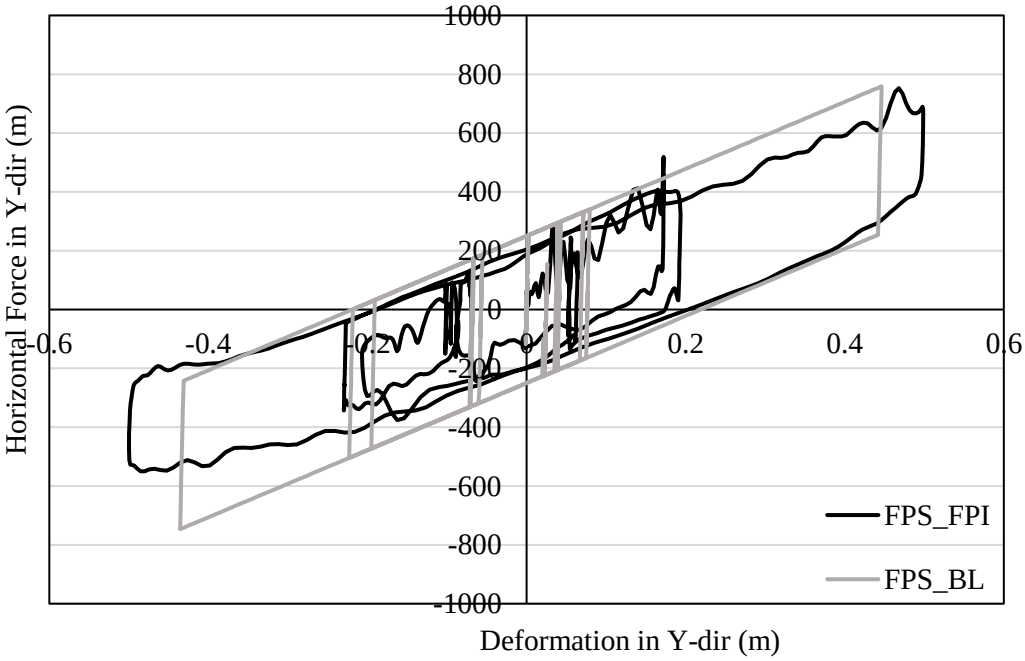


Figure 5.46. Hysteresis of Iso2 link for Kocaeli1158 ground motion for Y direction

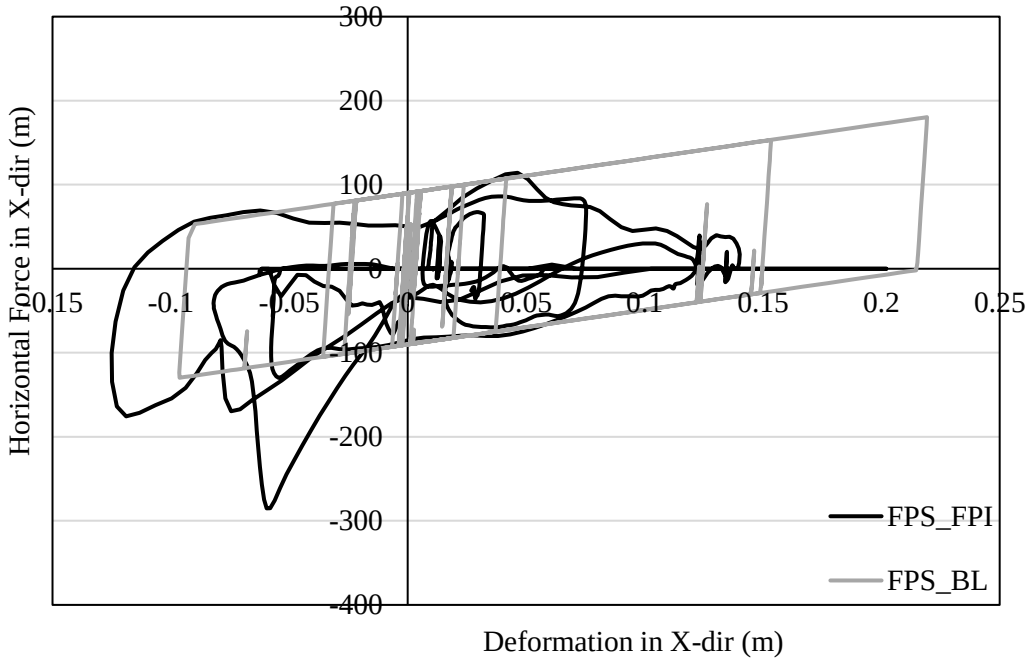


Figure 5.47. Hysteresis of Iso3 link for Kocaeli1158 ground motion for X direction

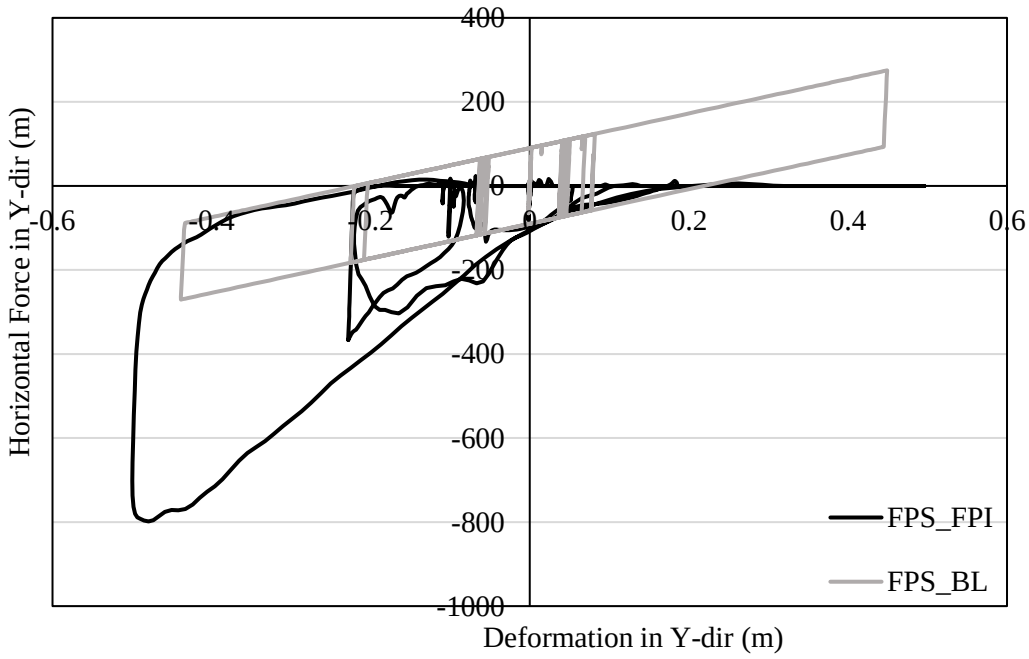


Figure 5.48. Hysteresis of Iso3 link for Kocaeli1158 ground motion for Y direction

## 5.6 Uplift Behavior

Isolators in structures with high aspect ratios are prone to tensile (uplift) deformations during seismic actions (Feng et al., 2004; Takaoka et al., 2011; Masaki et al., 2000) due to the overturning moment and rocking behavior. Especially isolators that are located under the shear walls or at the corner of the building are more susceptible to high compressive and tensile actions. In order to sustain the stability of the isolators, the evaluation of the uplift behavior is crucial. For both HDRB and FPS bearings, the isolator forces and deformations were obtained from MCE seismic level with LB isolator properties. For each ground motion, peak uplift deformations among each type were received and compared with the findings from the literature. Also, maximum tensile forces in HDRB bearings were examined in terms of tensile stresses.

Maximum uplift displacements of eleven ground motions are shown in Table 5.7. For HDRB, the peak tensile displacement was retrieved as 5.07 mm from RSN316 ground motion (Westmorland, 1981) in the DHI model. This value corresponds to 2.54% tensile strain when the total rubber height of 200 mm is considered. Therefore the HDRB design complies with the 5% tensile strain, in which isolators remain almost linear elastic, in the Japanese literature (Kani et al., 1999; Iwabe et al., 1999; Takayama et al., 1999) and also mentioned in Yang et al. (2010).

From Table 5.7, the maximum uplift displacement for FPS bearings was attained as 3.56 mm from the RSN850 event (Landers, 1992) among the FPS models. These results of all cases are nearly inside the range (2-3) mm observed by Fenz (2008). These displacement magnitudes are only instantaneous, there might be a risk of slider topping over the isolator, which can induce severe damage. In some earthquakes, uplift behavior for durations of 1-2 seconds were observed for the isolator under the shear wall. Therefore, in a design project with such structural characteristics, uplift response should be investigated carefully.

When BW or BL models are used instead of more comprehensive models, the uplift displacement response can be underestimated or overestimated depending on the ground motion.

Table 5.7 Peak uplift displacements for eleven ground motion

| | **Uplift Displacements (mm)** | | | | |
|---|---|---|---|---|---|
| | **HDRB-DHI** | **HDRB-BW** | **HDRB-BL** | **FPS-FPI** | **FPS-MLP** |
| Imperial Valley-06_187 | 3.03 | 2.74 | 3.47 | 2.05 | 1.99 |
| Westmorland_316 | 5.07 | 4.49 | 5.06 | 2.56 | 2.37 |
| Chalfant Valley_549 | 1.72 | 1.63 | 2.04 | 0.83 | 1.24 |
| Chalfant Valley-02_558 | 1.32 | 1.45 | 1.88 | 0.79 | 1.04 |
| Erzican_ Turkey_821 | 3.74 | 3.32 | 4.12 | 1.67 | 1.60 |
| Landers_850 | 2.48 | 2.48 | 2.66 | 3.56 | 3.43 |
| Kobe_ Japan_1116 | 2.37 | 2.42 | 2.98 | 1.17 | 1.53 |
| Kocaeli_ Turkey_1158 | 2.95 | 2.38 | 3.12 | 1.38 | 1.52 |
| Duzce_ Turkey_1605 | 2.94 | 2.58 | 3.11 | 2.07 | 1.41 |
| Chi-Chi_ Taiwan-04_2752 | 2.18 | 2.32 | 2.74 | 1.32 | 1.28 |
| Darfield_ New Zealand_6893 | 1.81 | 1.50 | 2.17 | 1.33 | 1.06 |

For HDRB models, the maximum isolator tensile forces were obtained for each ground motion. The forces were divided by the effective area for the corresponding isolator type. The average response of eleven ground motion is assessed. As a result, tensile stresses were calculated and are presented in Table 5.8. The DHI and BW models yielded results that are close to each other and satisfying the 1 MPa tensile limit stress, recommended by Bridgestone and Yang et al. (2010), except some ground motions with high intensities or pulse-like behavior. However the response of BL model showed significantly higher tensile demands on the bearings, especially the Type 4 isolators, which are located under the shear walls due to their effective area to bear high tensile and compressive demands.

Table 5.8 Peak tensile stresses for HDRB models

| | Maximum Tensile Stresses (kPa) | | | | | | | | | | | |
|---|---|---|---|---|---|---|---|---|---|---|---|---|
| | DHI Types | | | | BW Types | | | | BL Types | | | |
| | **1** | **2** | **3** | **4** | **1** | **2** | **3** | **4** | **1** | **2** | **3** | **4** |
| **187** | 680 | 752 | 824 | 884 | 616 | 698 | 759 | 881 | 663 | 942 | 793 | 1084 |
| **316** | 1140 | 1274 | 709 | 1938 | 945 | 1134 | 780 | 1743 | 880 | 1155 | 930 | 1965 |
| **549** | 376 | 441 | 446 | 668 | 303 | 431 | 358 | 546 | 371 | 526 | 426 | 790 |
| **558** | 266 | 349 | 324 | 378 | 309 | 386 | 362 | 531 | 385 | 512 | 463 | 554 |
| **821** | 719 | 990 | 1023 | 1197 | 719 | 880 | 910 | 1253 | 825 | 993 | 1050 | 1597 |
| **850** | 484 | 484 | 619 | 963 | 490 | 474 | 618 | 964 | 521 | 530 | 640 | 1032 |
| **1116** | 419 | 628 | 482 | 793 | 482 | 643 | 437 | 916 | 521 | 730 | 525 | 1156 |
| **1158** | 659 | 751 | 882 | 1005 | 521 | 630 | 704 | 924 | 627 | 745 | 701 | 1210 |
| **1605** | 622 | 781 | 904 | 1036 | 570 | 685 | 832 | 950 | 575 | 844 | 941 | 916 |
| **2752** | 441 | 580 | 565 | 792 | 453 | 615 | 550 | 837 | 490 | 714 | 738 | 1061 |
| **6893** | 355 | 470 | 311 | 700 | 296 | 388 | 368 | 581 | 368 | 488 | 462 | 840 |
| **Ave** | 560 | 682 | 644 | 941 | 519 | 633 | 607 | 920 | 566 | 744 | 697 | 1110 |

# CHAPTER 5

# CONCLUSIONS

In this thesis, performance evaluation of investigated base-isolated hospital building with irregular T plan shape and high aspect ratio (2:1) is conducted using various nonlinear isolator models. Two types of base isolation systems, high damping rubber bearing, and friction pendulum system, were designed according to the Turkish Building Seismic Code (TBDY2019) using different nonlinear models. The most commonly used types of modeling approaches in research and practice were used for nonlinear time history analysis under eleven ground motions. For HDRB, the deformation history integral type (DHI) model, the smoothed Bouc-Wen (BW) bilinear model, and sharp bilinear (BL) model were considered. Moreover, the friction and pendulum behavior (friction pendulum isolator, FPI) model and the sharp BL model were adopted for FPS isolators. The superstructural and isolation system response for various mathematical models are evaluated and compared in terms of maximum isolator displacements, structural forces, floor accelerations, inter-story drifts, and isolator uplift behavior. Based on the results, the following conclusions can be made for the investigated building:

- The maximum isolation system displacements can be overestimated or underestimated by the bilinear models. On average, the resulting displacements in sharp and smoothed bilinear models are close when compared to the highly nonlinear models for elastomeric isolators. However, the variation in maximum displacements between the sharp bilinear (BL) and nonlinear friction models is high. The resultant displacements are also highly dependent on the ground motion characteristics.
- There is a significant increase in the superstructural response (superstructural forces, floor accelerations and inter-story drifts) when idealized bilinear models are used instead of more accurate nonlinear models. The sharp

transitions of BL model could result in a response that are excessively overestimated. The smoothed bilinear model yields superstructural response that is more acceptable and comparable with the sophisticated models.

- Among the HDRB models, the bilinear models can capture the force-displacement behavior and energy dissipation of the rubber isolators. However, the sharp BL model could diverge from the actual behavior when the effect of bidirectional loading is significant. Moreover, the horizontal stiffness of FPS isolators highly dependent on the axial load and becomes zero during the uplift. When modeled as an FPS isolator, the sharp bilinear model whose all three directions are uncoupled, yields unrealistic results, especially at locations with higher overturning moments and shear walls.
- The average uplift deformations were observed to be within the safe margins found in the literature for all HDRB and FPS models. Also, the DHI and smooth BW model shows similar response, while the sharp BL model yielded the highest tensile stresses and might lead to overdesign.

Although the smoothed bilinear model predicts relatively more accurate results, both idealized bilinear models significantly overestimate the superstructural response for this building. Many design guidelines do not include recommendations about highly nonlinear sophisticated models. An engineer should carefully assess the isolator models' capabilities and possible outcoming structural response before selecting the mathematical model to include in the analysis and design. The results have shown that the sharp bilinear model is not very suitable to use in the sophisticated 3-D model, especially for FPS isolators.

## 6.1 Future Studies

Although bilinear models may not capture the most realistic behavior, they are practical to implement in the analysis software by the engineers inexperienced in the high nonlinear concept of DHI and FPI models. The bilinear models can be modified to capture the behavior relatively better. For HDRB isolators, the sharp BL or smoothed BW model can be modified to include the stiffness increase when the shear strain exceeds 200%. The modification of the BL model have been already under investigation under a joint research by the writer, thesis supervisor and the Bridgestone Corporation.

By experience in base-isolated hospital projects, the sharp BL model does not yield significant superstructural response in all buildings. It is observed and studied by several researchers in the literature and also specific for this hospital model. The reason for this enormous difference in this thesis when compared to other isolator models is still not very clear. The reason can be studied parametrically with different configurations of structural and hysteretic characteristics.

## REFERENCES


Bouc, R. (1971). Modele mathematique d'hysteresis. *Acustica*, *24*(1), 16–25.

Calvi, P. M., & Calvi, G. M. (2018). Historical development of friction-based seismic isolation systems. *Soil Dynamics and Earthquake Engineering*, *106*(October 2017), 14–30. https://doi.org/10.1016/j.soildyn.2017.12.003

Chopra, A. K. (2012). *Dynamics of structures : theory and applications to earthquake engineering, 4/E*.

Computers and Structures Inc. (2017). *CSI Analysis Reference Manual*.

Constantinou, M., Mokha, A., & Reinhorn, A. (1990). Teflon Bearings in Base Isolation II: Modeling. *Journal of Structural Engineering*, *116*(2), 455–474. https://doi.org/10.1061/(ASCE)0733-9445(1990)116:2(455)

Disaster and Emergency Management Presidency, T. M. of the I. (2018). *Türkiye Bina Deprem Yönetmeliği 2019* (Vol. 30364, Issue 1).

Erdik, M., Ülker, Ö., Şadan, B., & Tüzün, C. (2018). Seismic isolation code developments and significant applications in Turkey. *Soil Dynamics and Earthquake Engineering*, *115*, 413–437. https://doi.org/10.1016/j.soildyn.2018.09.009

Erkakan, E. (2014). *EXPERIMENTAL INVESTIGATION OF UPLIFT ON SEISMIC BASE ISOLATORS*. Middle East Technical University.

Feng, D., Miyama, T., Lu, X., & Ikenaga, M. (2004). A Shaking Table Test Study on Shear Tensile Properties of Lead Rubber Bearings. *13th World Conference on Earthquake Engineering Vancouver, B.C., Canada*. https://doi.org/10.1061/ASCEEM.1943-7889.0000007

Fenz, D. M. (2008). *DEVELOPMENT, IMPLEMENTATION AND VERIFICATION OF DYNAMIC ANALYSIS MODELS FOR MULTI-SPHERICAL SLIDING BEARINGS*. State University of New York.

Fenz, D. M., & Constantinou, M. C. (2008). Modeling Triple Friction Pendulum Bearings for Response-History Analysis. *Earthquake Spectra*, *24*(4), 1011–1028. https://doi.org/10.1193/1.2982531

Furukawa, T., Ito, M., Izawa, K., & Noori, M. N. (2005). System Identification of Base-Isolated Building using Seismic Response Data. *Journal of Engineering Mechanics*, *131*(3), 268–275. https://doi.org/10.1061/(ASCE)0733-9399(2005)131:3(268)

Griffith, M. C., Aiken, I. D., & Kelly, J. M. (1990). Displacement Control and Uplift Restraint for Base-Isolated Structures. *Journal of Structural Engineering*, *116*(4), 1135–1148. https://doi.org/10.1061/(ASCE)0733-9445(1990)116:4(1135)

Ibrahimbegovic, A., & Wilson, E. L. (1989). Simple numerical algorithms for the mode superposition analysis of linear structural systems with non-proportional damping. *Computers & Structures*, *33*(2), 523–531. https://doi.org/10.1016/0045-7949(89)90026-6

Kampas, G., & Makris, N. (2012). Time and frequency domain identification of seismically isolated structures: advantages and limitations. *Earthquakes and Structures*, *3*(3_4), 249–270. https://doi.org/10.12989/eas.2012.3.3_4.249

Kasalanati, A., & Constantinou, M. C. (2005). Testing and Modeling of Prestressed Isolators. *Journal of Structural Engineering*, *131*(6), 857–866. https://doi.org/10.1061/(ASCE)0733-9445(2005)131:6(857)

Kato, H., Mori, T., Murota, N., & Kikuchi, M. (2015). Analytical Model for Elastoplastic and Creep-Like Behavior of High-Damping Rubber Bearings. *Journal of Structural Engineering*, *141*(9), 04014213. https://doi.org/10.1061/(ASCE)ST.1943-541X.0001181

Kelly, J. M. (1986). Aseismic base isolation: review and bibliography. *Soil Dynamics and Earthquake Engineering*, *5*(4), 202–216. https://doi.org/10.1016/0267-7261(86)90006-0

Khoshnudian, F., & Motamedi, D. (2013). Seismic response of asymmetric steel isolated structures considering vertical component of earthquakes. *KSCE Journal of Civil Engineering*, *17*(6), 1333–1347. https://doi.org/10.1007/s12205-013-0115-5

Kikuchi, M., & Aiken, I. D. (1997). An Analytical Hysteresis Model for Elastomeric Seismic Isolation Bearings. *Earthquake Engineering & Structural Dynamics*, *26*(2), 215–231. https://doi.org/10.1002/(SICI)1096-9845(199702)26:2<215::AID-EQE640>3.0.CO;2-9

Kulicki, J. M. (2014). Highway bridge design specifications. In *Bridge Engineering Handbook: Fundamentals, Second Edition* (Issue September). https://doi.org/10.1201/b15616

Makris, N., & Vassiliou, M. F. (2011). The existence of ‘complete similarities’ in the response of seismic isolated structures subjected to pulse-like ground motions and their implications in analysis. *Earthquake Engineering & Structural Dynamics*, *40*(10), 1103–1121. https://doi.org/10.1002/eqe.1072

Mano, T., & Mangerig, I. (2015). Determination of Tensile Capacity of Elastomeric Bearings. *Structural Engineering International*, *25*(2), 134–140. https://doi.org/10.2749/101686615X14210663188376

Markou, A. A., & Manolis, G. D. (2016). Mechanical formulations for bilinear and trilinear hysteretic models used in base isolators. *Bulletin of Earthquake Engineering*, *14*, 3591–3611. https://doi.org/10.1007/s10518-016-0014-5

Masaki, N., Mori, T., Murota, N., & Kasai, K. (2017). *Validation of Hysteresis Model of Deformation-History Integral Type for High Damping Rubber Bearings*. http://www.wcee.nicee.org/wcee/article/16WCEE/WCEE2017-4583.pdf

Mavronicola, E. A. (2017). *Nonlinear Modeling Considerations on the Seismic Response of Base-Isolated Buildings: 2D and 3D Investigations of Pounding*. University of Cyprus.

Mavronicola, E., & Komodromos, P. (2014). On the response of base-isolated buildings using bilinear models for LRBs subjected to pulse-like ground motions: Sharp vs. smooth behaviour. *Earthquake and Structures*, *7*(6), 1223–1240. https://doi.org/10.12989/eas.2014.7.6.1223

Mokha, A., Constantinou, M., & Reinhorn, A. (1990). Teflon Bearings in Base Isolation I: Testing. *Journal of Structural Engineering*, *116*(2), 438–454. https://doi.org/10.1061/(ASCE)0733-9445(1990)116:2(438)

Morgan, T. A. (2007). *The Use of Innovative Base Isolation Systems to Achieve Complex Seismic Performance Objectives*. University of California, Berkeley.

Murota, N., Suzuki, S., Mori, T., Wakishima, K., Sadan, B., Tuzun, C., Sutcu, F., & Erdik, M. (2021). Performance of high-damping rubber bearings for seismic isolation of residential buildings in Turkey. *Soil Dynamics and Earthquake Engineering*, *143*, 106620. https://doi.org/10.1016/j.soildyn.2021.106620

Naeim, F., & Kelly, J. M. (1999). Design of Seismic Isolated Structures. In *Earthquake Spectra*. John Wiley & Sons, Inc. https://doi.org/10.1002/9780470172742

Nagarajaiah, S., Reinhorn, A. M., & Constantinou, M. C. (1991). Nonlinear Dynamic Analysis of 3-D-Base-Isolated Structures. *Journal of Structural Engineering*, *117*(7), 2035–2054. https://doi.org/10.1061/(ASCE)0733-9445(1991)117:7(2035)

Özdemir, G. (2010). *RESPONSE OF ISOLATED STRUCTURES UNDER BI-DIRECTIONAL EXCITATIONS OF NEAR-FIELD GROUND MOTIONS*. Middle East Technical University.

Park, Y. J., Wen, Y. K., & Ang, A. H.-S. (1986). Random vibration of hysteretic systems under bi-directional ground motions. *Earthquake Engineering & Structural Dynamics*, *14*(4), 543–557. https://doi.org/10.1002/eqe.4290140405

Pietra, D., & Park, A. R. L. (2017). Behaviour and Modelling of Lead-Rubber Bearings Subjected To Tensile Actions. *16th World Conference on Earthquake, 16WCEE*.

Ray, T., Sarlis, A. A., Reinhorn, A. M., & Constantinou, M. C. (2013). Hysteretic models for sliding bearings with varying frictional force. *Earthquake Engineering & Structural Dynamics*, *42*(15), 2341–2360. https://doi.org/10.1002/eqe.2373

Robinson, W. H. (1982). Lead-rubber hysteretic bearings suitable for protecting structures during earthquakes. *Earthquake Engineering & Structural Dynamics*, *10*(4), 593–604. https://doi.org/10.1002/eqe.4290100408

Roussis, P. C. (2009). Study on the Effect of Uplift-Restraint on the Seismic Response of Base-Isolated Structures. *Journal of Structural Engineering*, *135*(12), 1462–1471. https://doi.org/10.1061/(ASCE)ST.1943-541X.0000070

Roussis, P. C., & Constantinou, M. C. (2006). Uplift-restraining Friction Pendulum seismic isolation system. *Earthquake Engineering & Structural Dynamics*, *35*(5), 577–593. https://doi.org/10.1002/eqe.545

Simo, J. C., & Hughes, T. J. R. (1997). *Computational Inelasticity*. Springer.

Skinner, R. I., Robinson, W. H., & McVerry, G. H. (1993). An Introduction to Seismic Isolation. In *John Wiley & Sons Ltd*. https://doi.org/10.1111/j.1475-1305.1993.tb00842.x

Subcommittee on Bridges, S. S. and T. O. (2010). *Guide Specifications for Seismic Isolation Design, AAHSTO*.

Vassiliou, M. F., Tsiavos, A., & Stojadinović, B. (2013). Dynamics of inelastic base-isolated structures subjected to analytical pulse ground motions. *Earthquake Engineering & Structural Dynamics*, *056*, n/a-n/a. https://doi.org/10.1002/eqe.2311

Warn, G. P., & Ryan, K. L. (2012). A Review of Seismic Isolation for Buildings: Historical Development and Research Needs. *Buildings*, *2*, 300–325. https://doi.org/10.3390/buildings2030300

Wen, Y.-K. (1976). Method for Random Vibration of Hysteretic Systems. *Journal of the Engineering Mechanics Division*, *102*(2), 249–263. https://doi.org/10.1061/JMCEA3.0002106

Wilson, E. L. (2000). No Title. In *Three Dimensional Static and Dynamic Analysis of Structures*. Computers and Structures, Inc. http://www.edwilson.org/Book/book.htm#Author

Yakut, A., Akyüz, U., Çabuk, E., Murota, N., & Suzuki, S. (2019, July 7). *Comparison of Modeling Approaches for High Damping Rubber Bearing*. https://doi.org/10.37153/2686-7974-2019-16-902-909

Yang, Q. R., Liu, W. G., He, W. F., & Feng, D. M. (2010). Tensile Stiffness and Deformation Model of Rubber Isolators in Tension and Tension-Shear States. *Journal of Engineering Mechanics*, *136*(4), 429–437. https://doi.org/10.1061/(asce)em.1943-7889.0000007

Zayas, V. A., Low, S. S., & Mahin, S. A. (1990). A Simple Pendulum Technique for Achieving Seismic Isolation. *Earthquake Spectra*, *6*(2), 317–333. https://doi.org/10.1193/1.1585573

# APPENDICES

## A. Appendix A – Time History Components of 11 Ground Motion

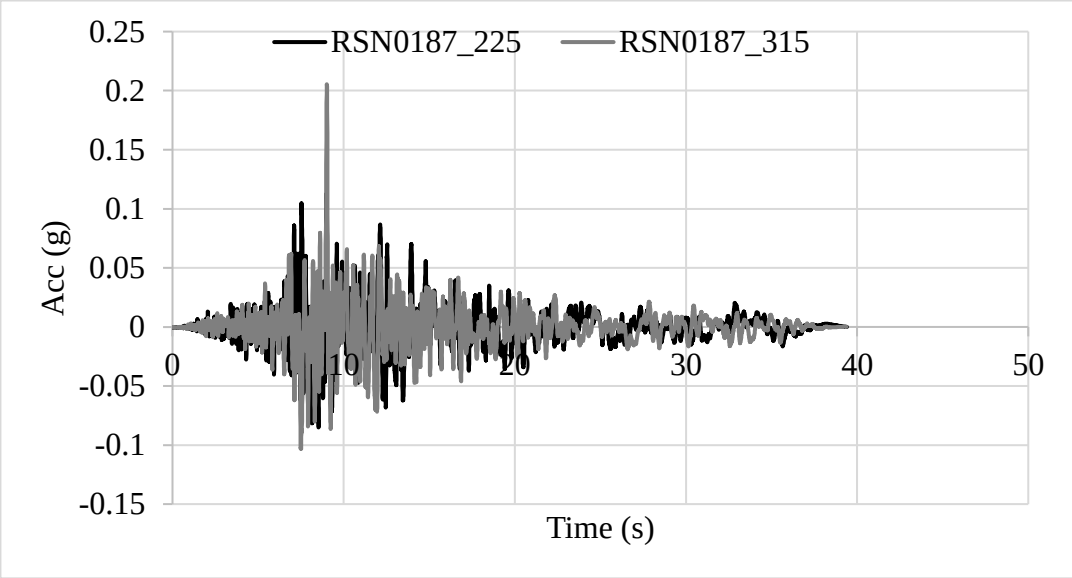


Figure A-1: Lateral components of Imperial Valley-06, 1979 ground motion

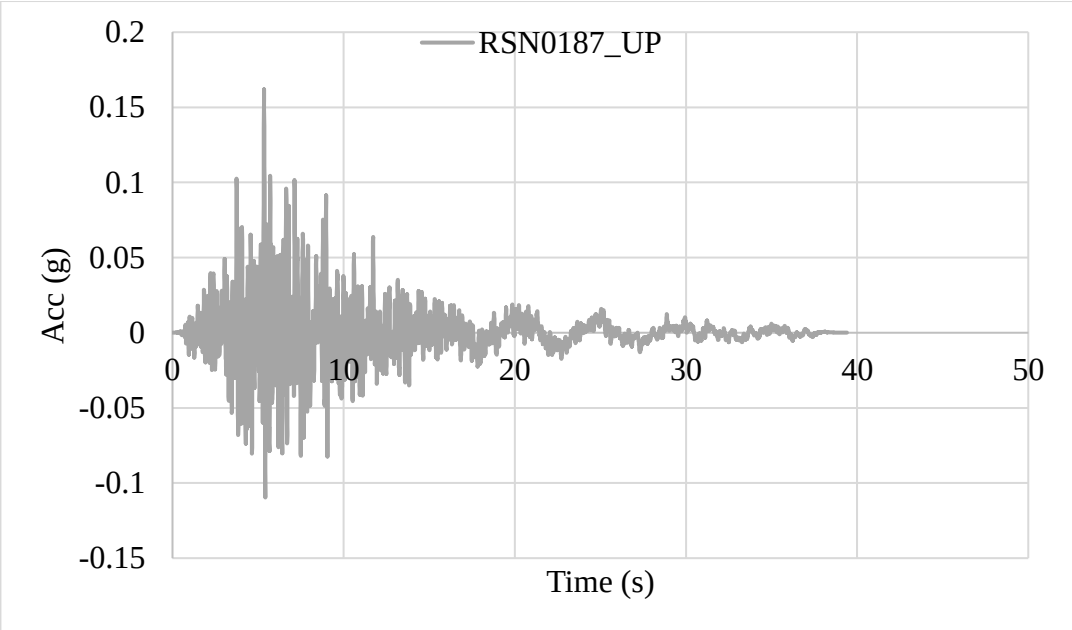


Figure A-2: Vertical component of Imperial Valley-06, 1979 ground motion

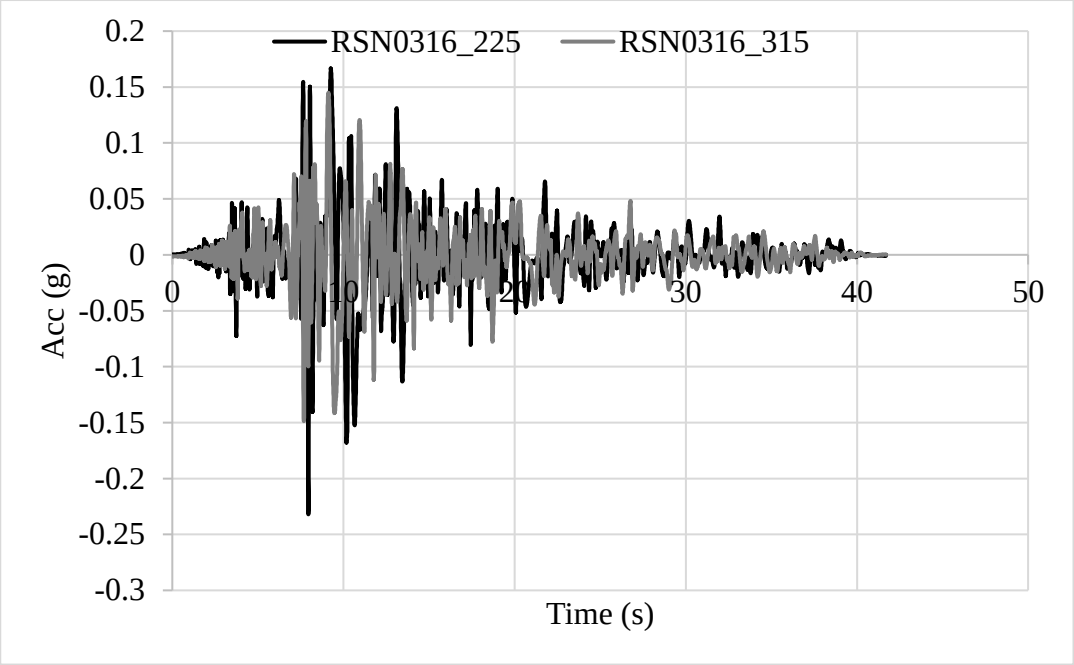


Figure A-3: Lateral components of Westmorland, 1981 ground motion

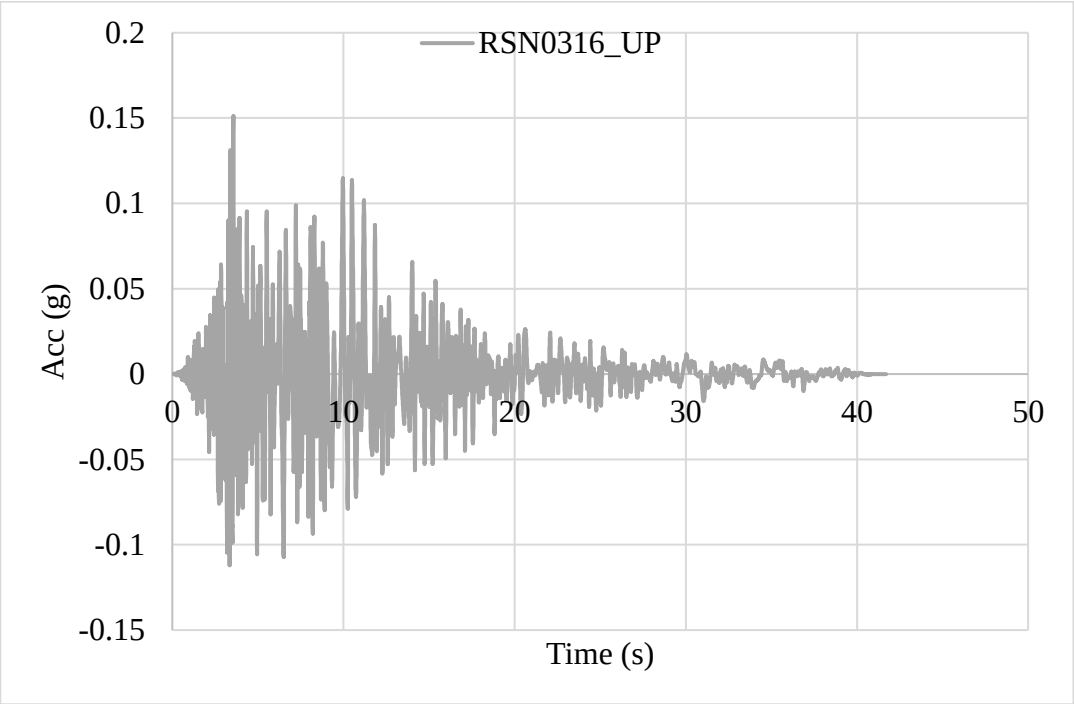


Figure A-4: Vertical component of Westmorland, 1981 ground motion

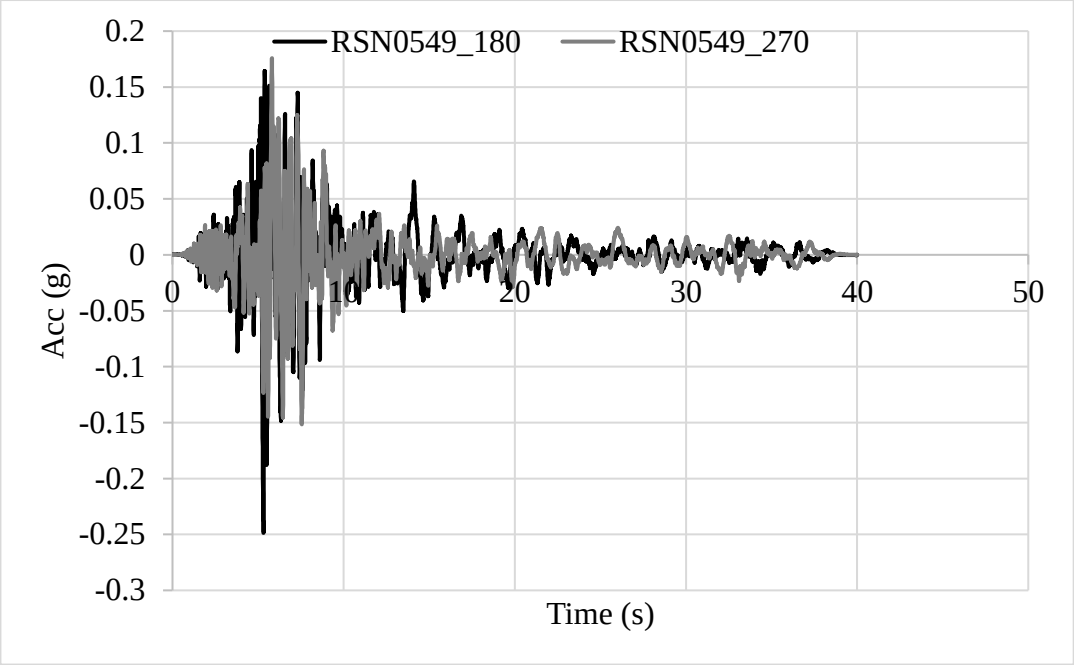


Figure A-5: Lateral components of Chalfant_Valley-02_Bishop-LADWP South St, 1986 ground motion

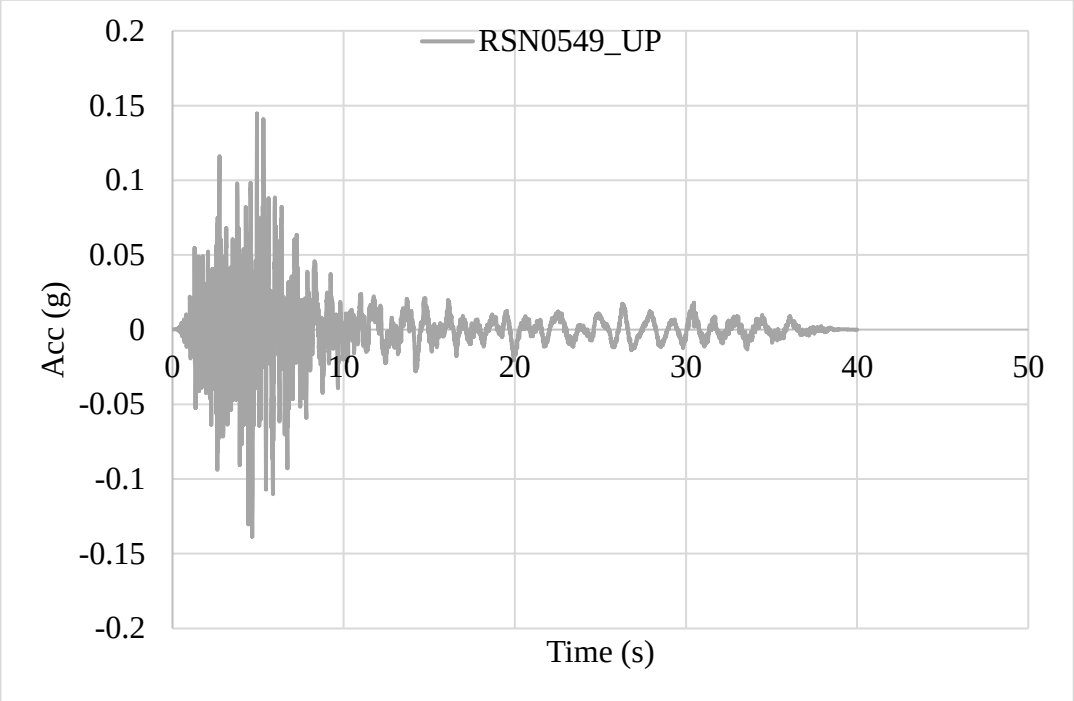


Figure A-6: Vertical component of Chalfant_Valley-02_Bishop-LADWP South St, 1986 ground motion

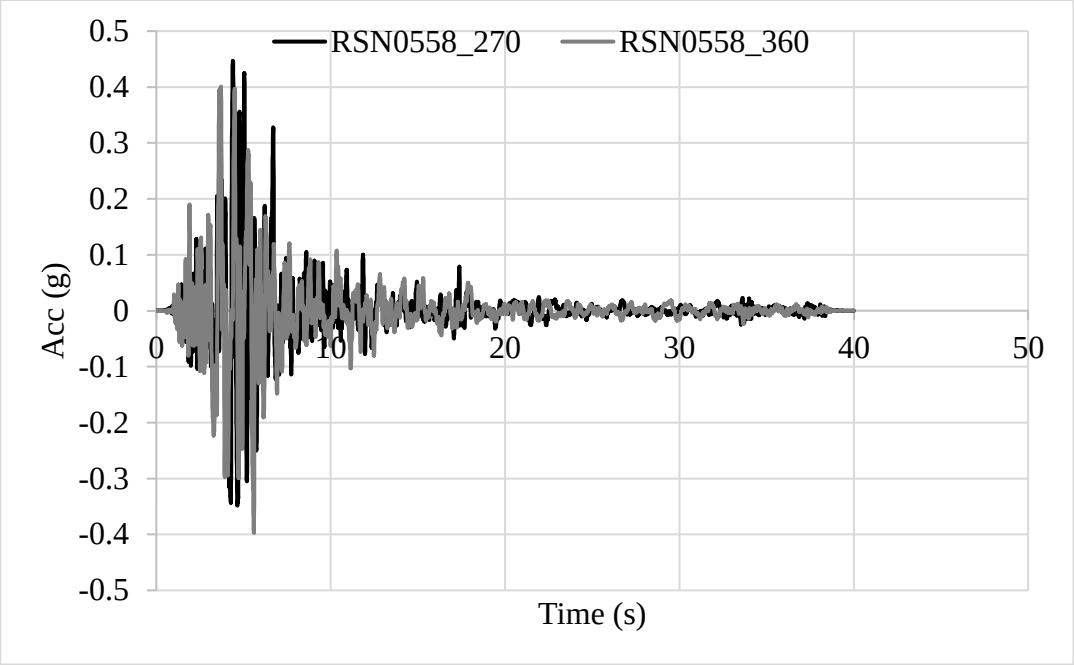


Figure A-7: Lateral components of Chalfant_Valley-02_Zack Brothers Ranch St, 1986 ground motion

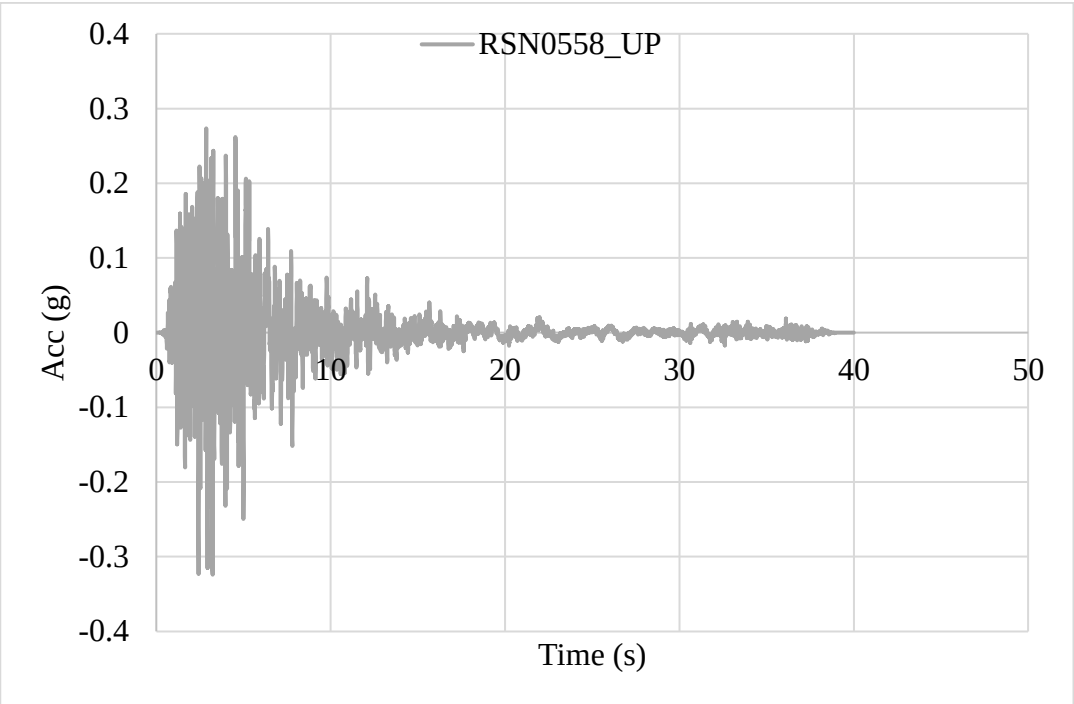


Figure A-8: Vertical component of Chalfant_Valley-02_Zack Brothers Ranch St, 1986 ground motion

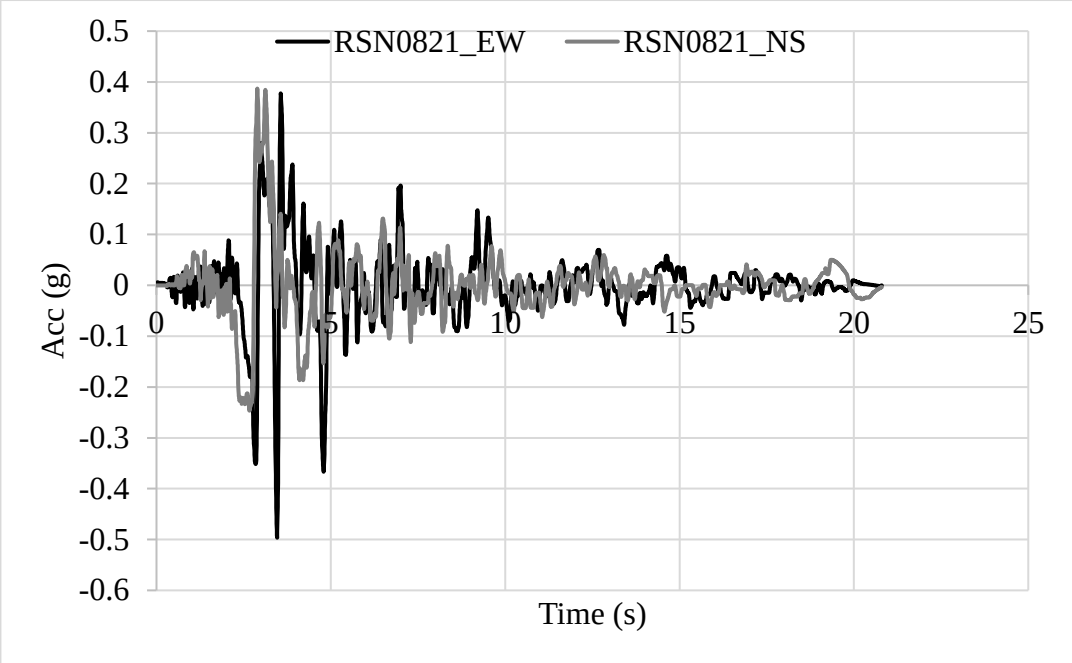


Figure A-9: Lateral components of Erzincan_Turkey, 1992 ground motion

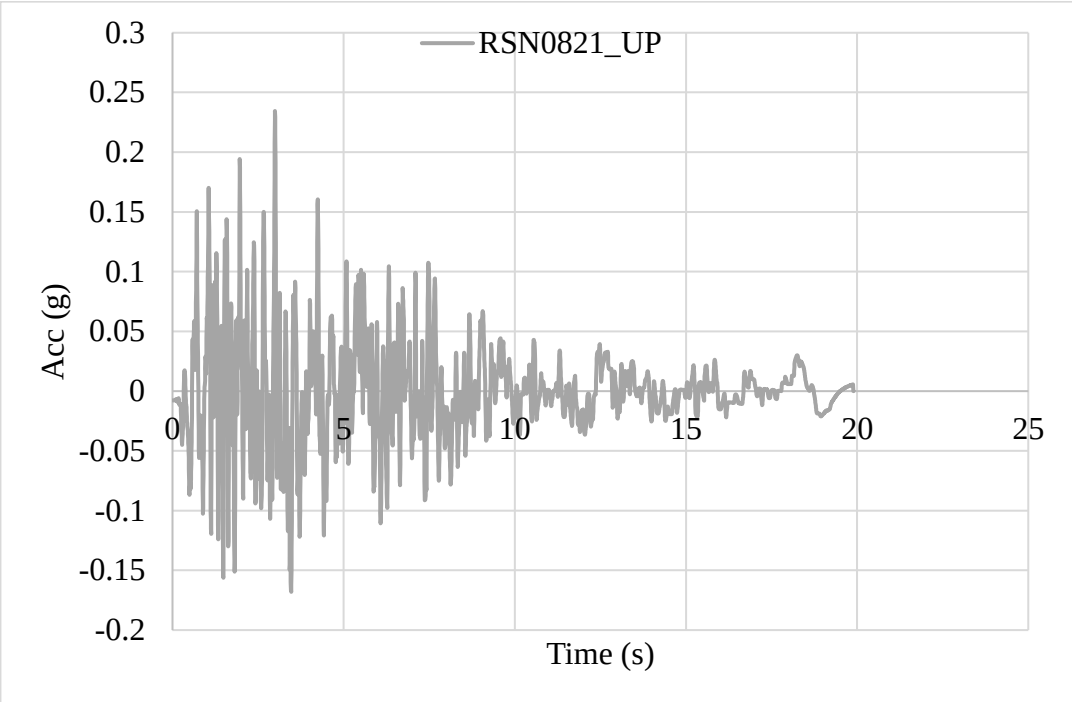


Figure A-10: Vertical component of Erzincan_Turkey, 1992 ground motion

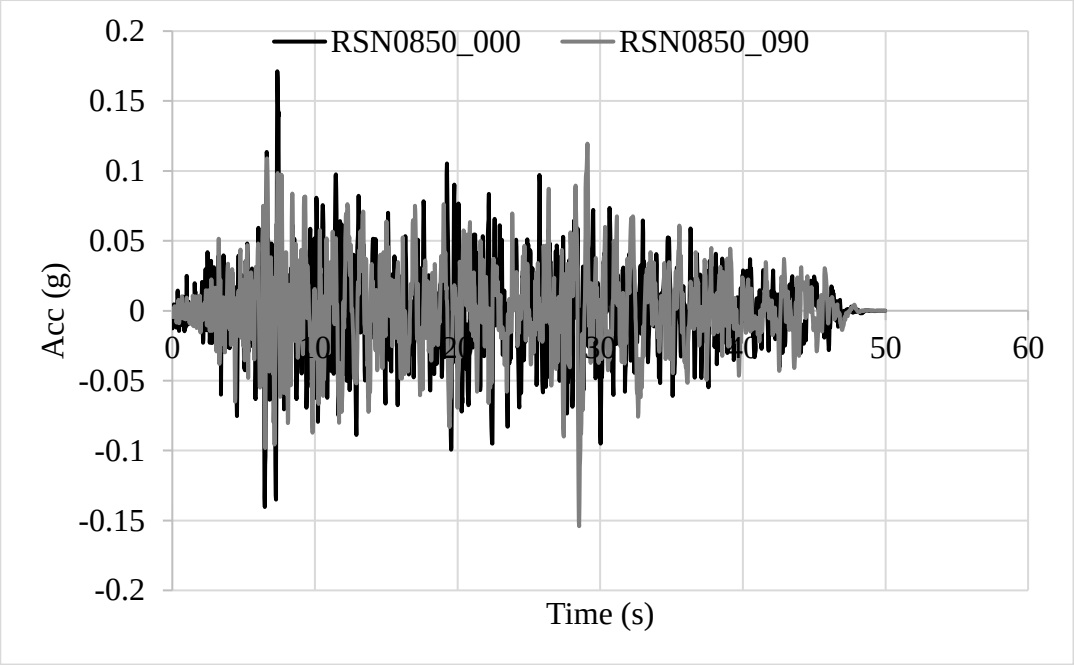


Figure A-11: Lateral components of Landers, 1992 ground motion

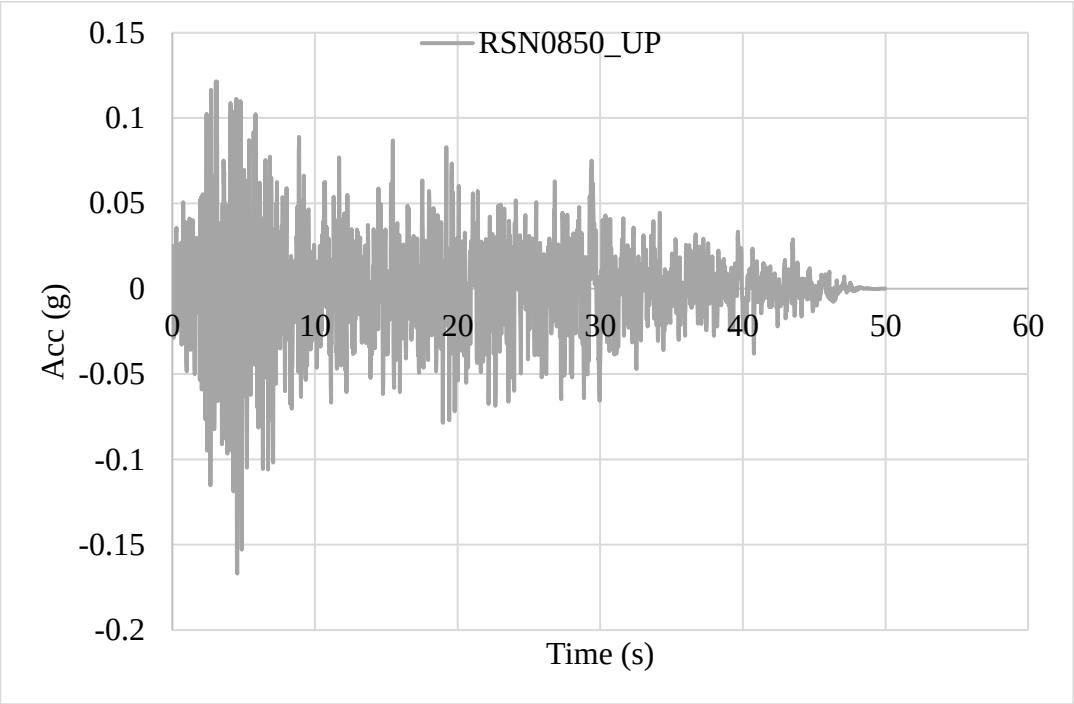


Figure A-12: Vertical component of Landers, 1992 ground motion

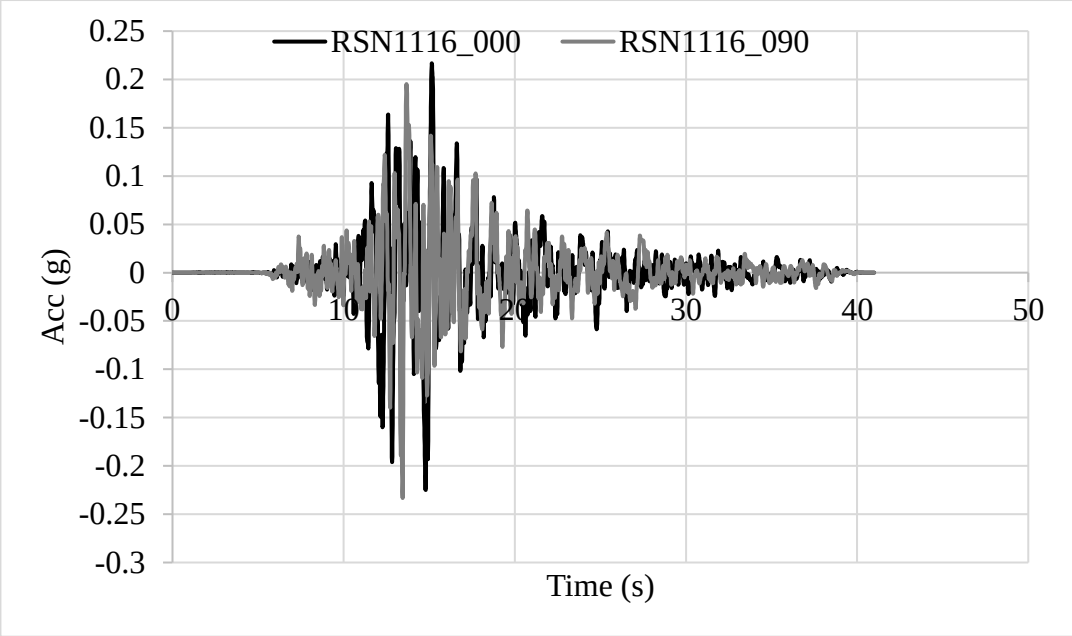


Figure A-13: Lateral components of Kobe_Japan, 1995 ground motion

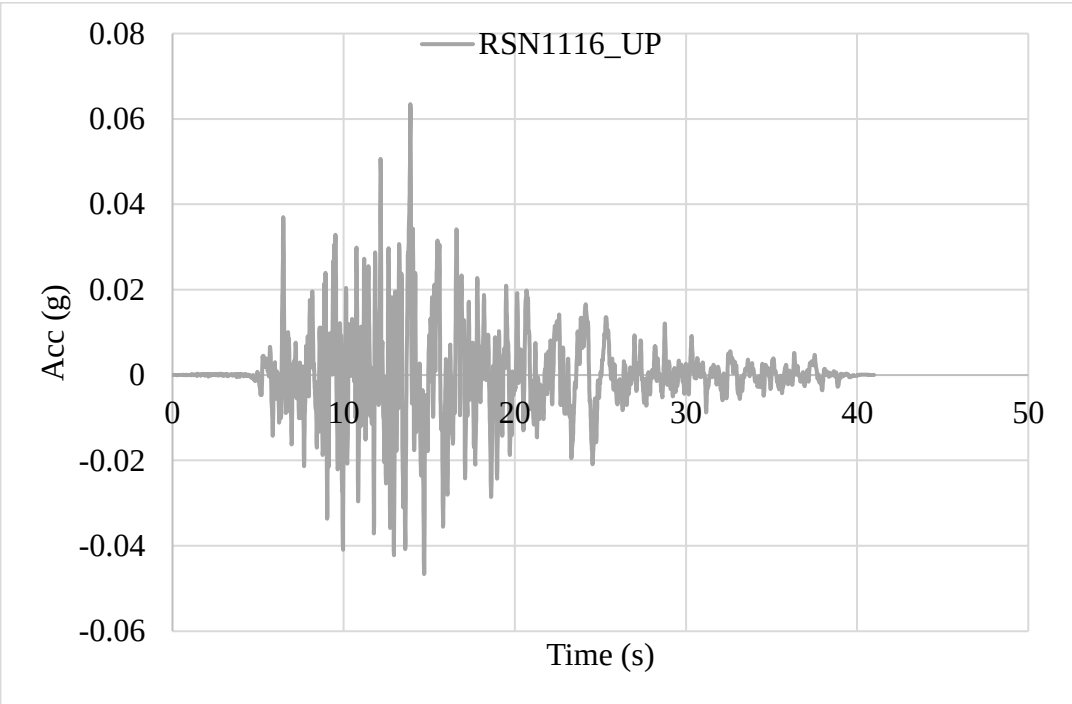


Figure A-14: Vertical component of Kobe_Japan, 1995 ground motion

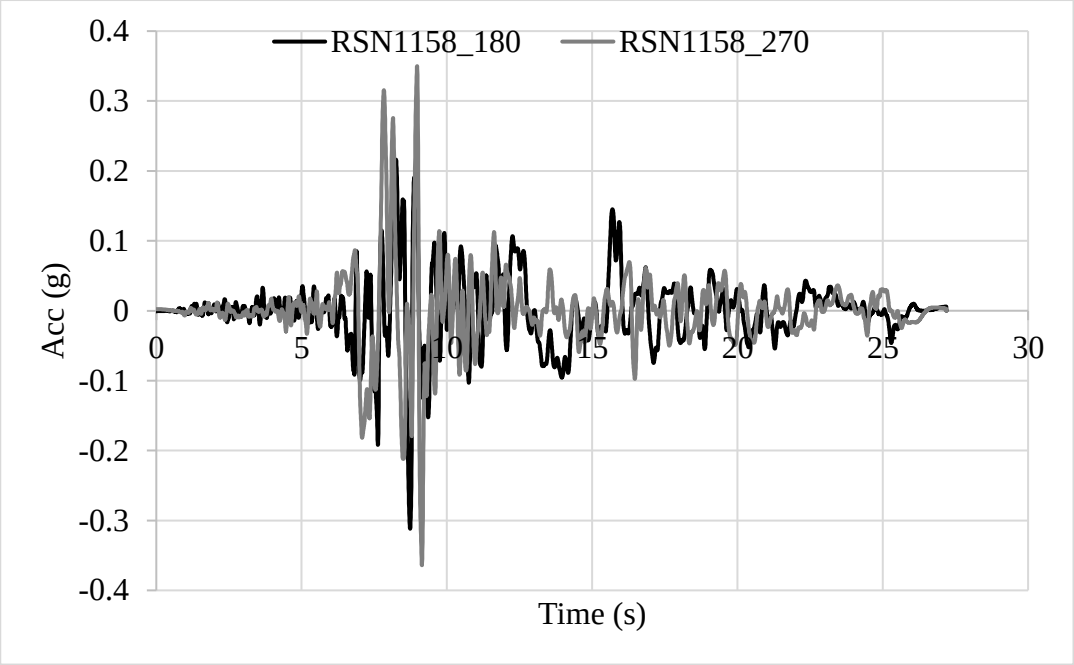


Figure A-15: Lateral components of Kocaeli_Turkey, 1999 ground motion

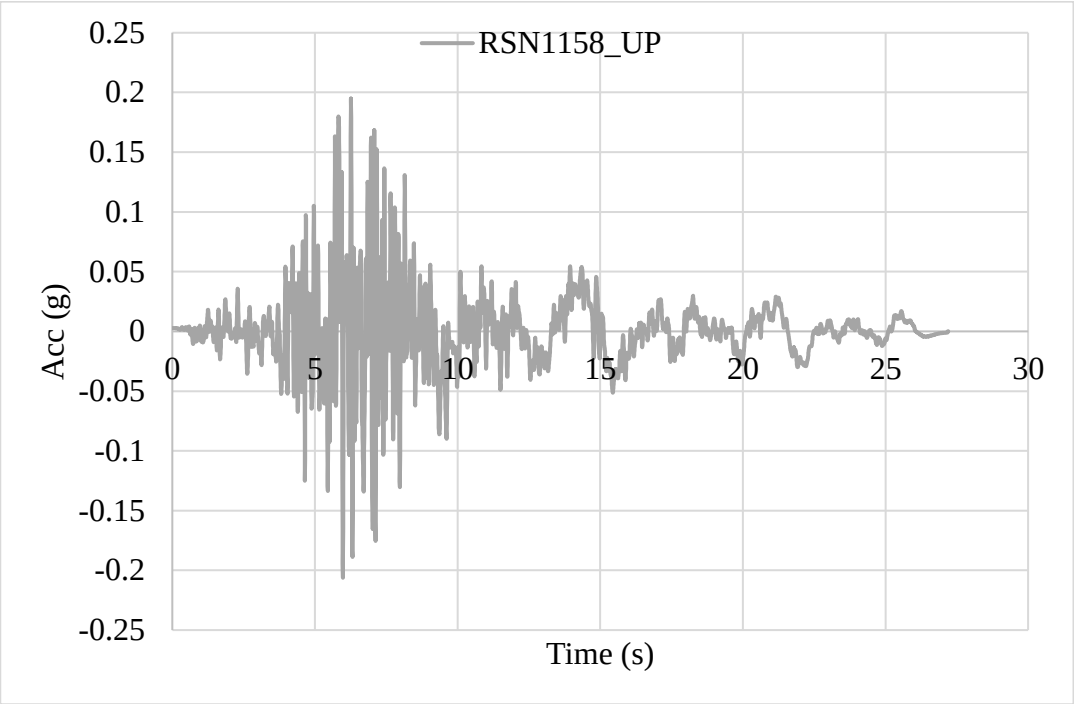


Figure A-16: Vertical component of Kocaeli_Turkey, 1999 ground motion

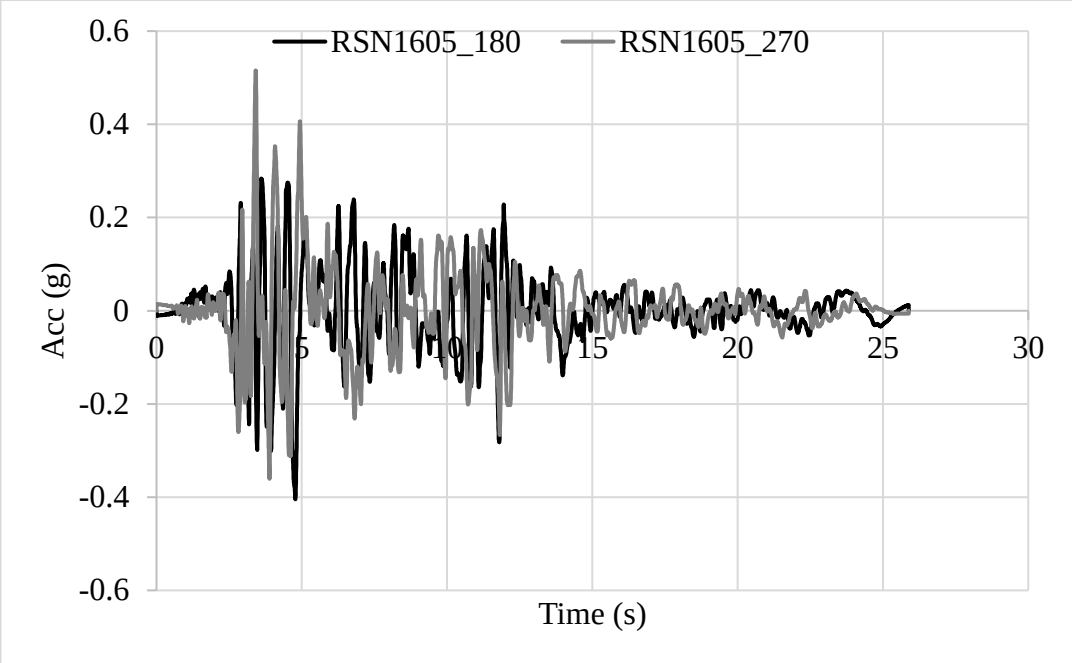


Figure A-17: Lateral components of Duzce_Turkey, 1999 ground motion

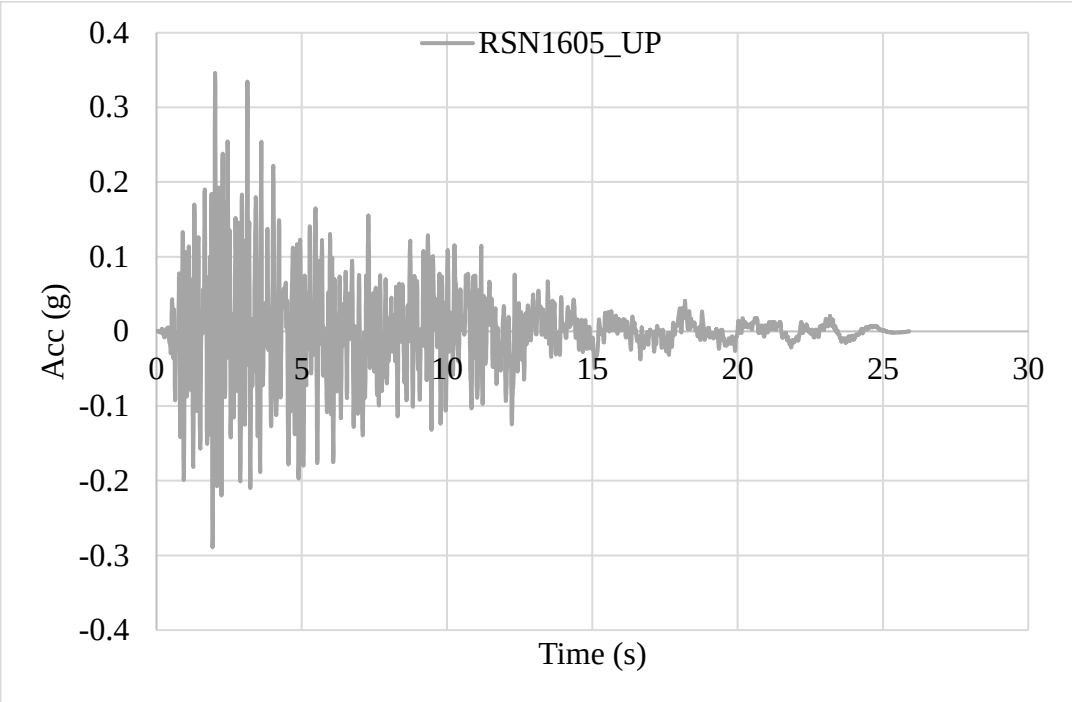


Figure A-18: Vertical component of Duzce_Turkey, 1999 ground motion

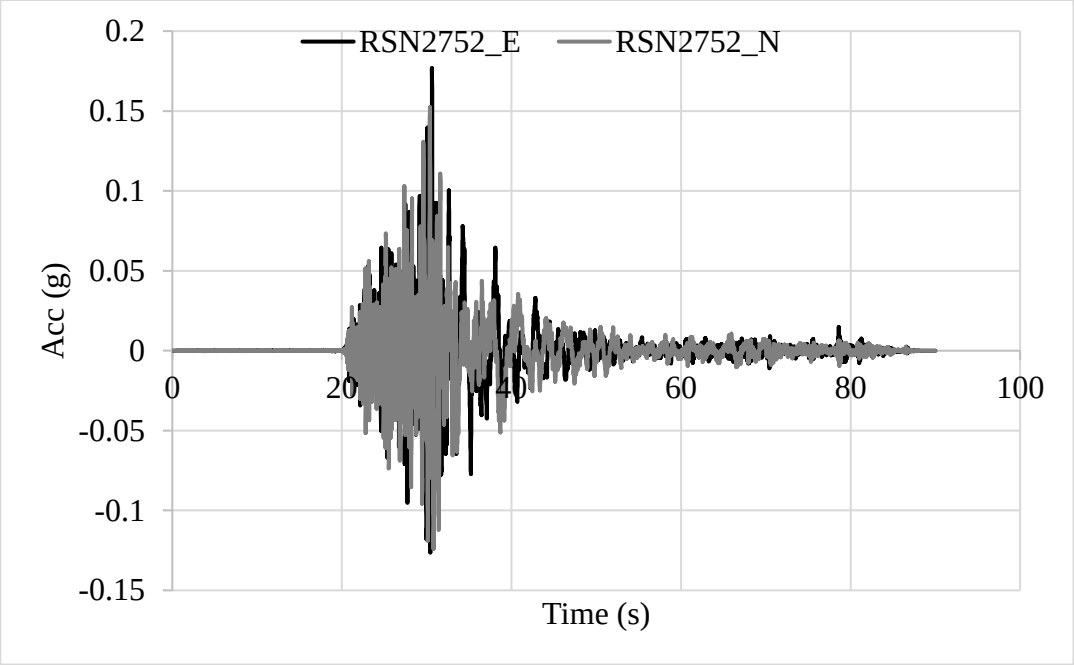


Figure A-19: Lateral components of Chi-Chi_Taiwan-04, 1999 ground motion

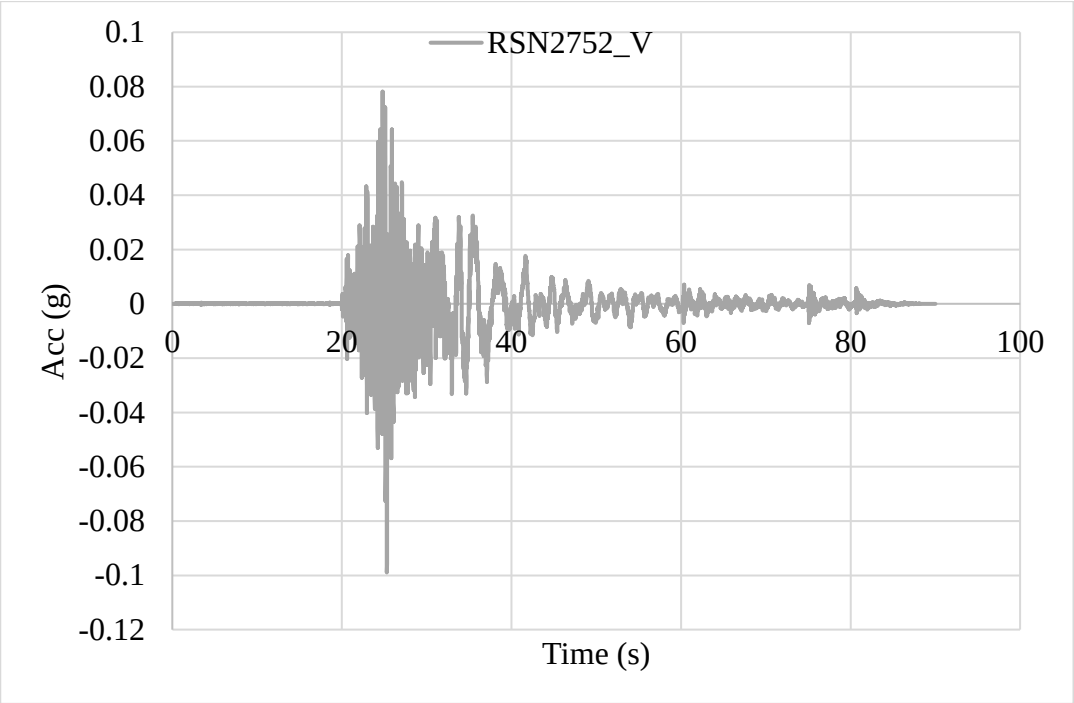


Figure A-20: Vertical component of Chi-Chi_Taiwan-04, 1999 ground motion

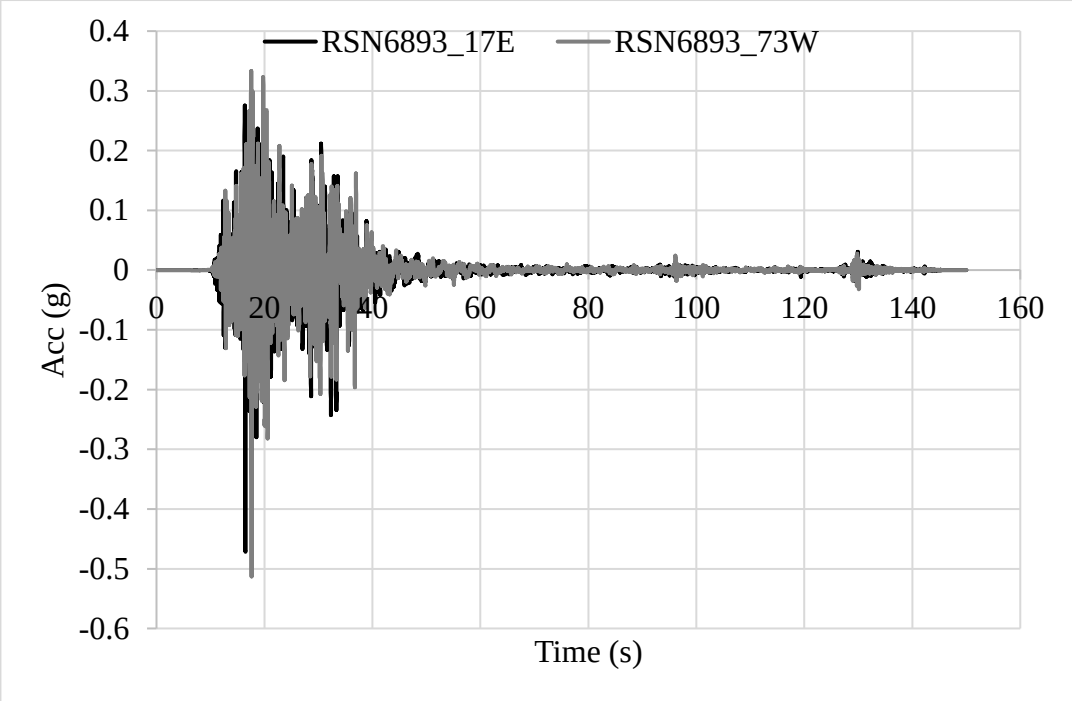


Figure A-21: Lateral components of Darfield_New Zealand, 2010 ground motion

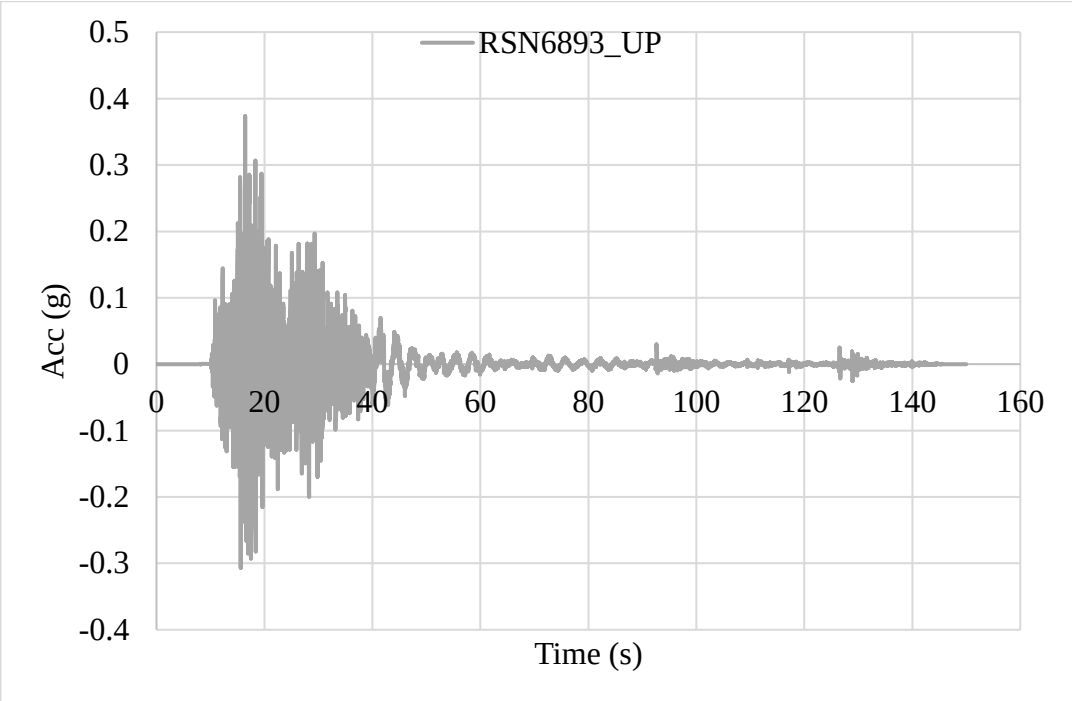


Figure A-20: Vertical component of Darfield_New Zealand, 2010 ground motion

## B. Appendix B – Comparison of Accelerations of Different Locations of the Building

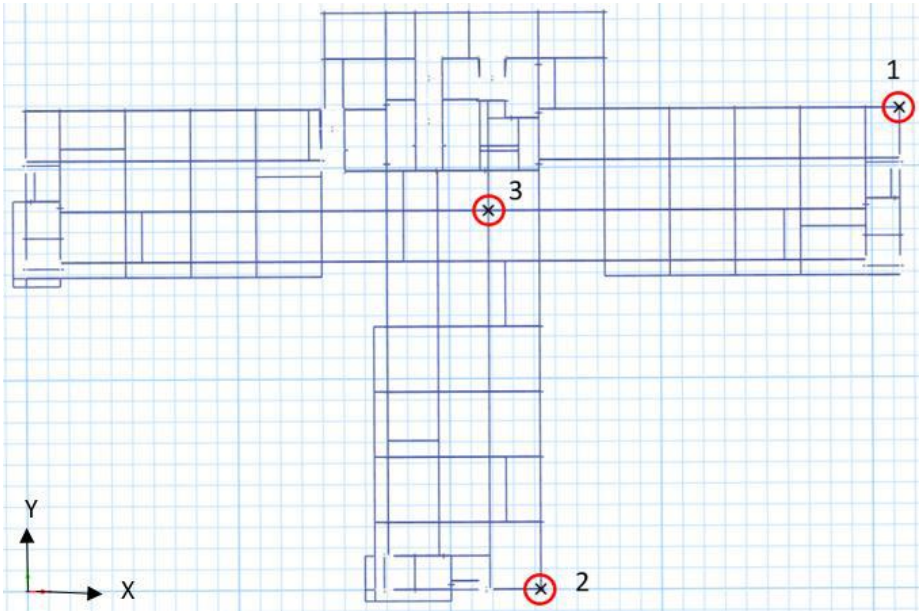


Figure B-1: Three selected joints to compare maximum accelerations

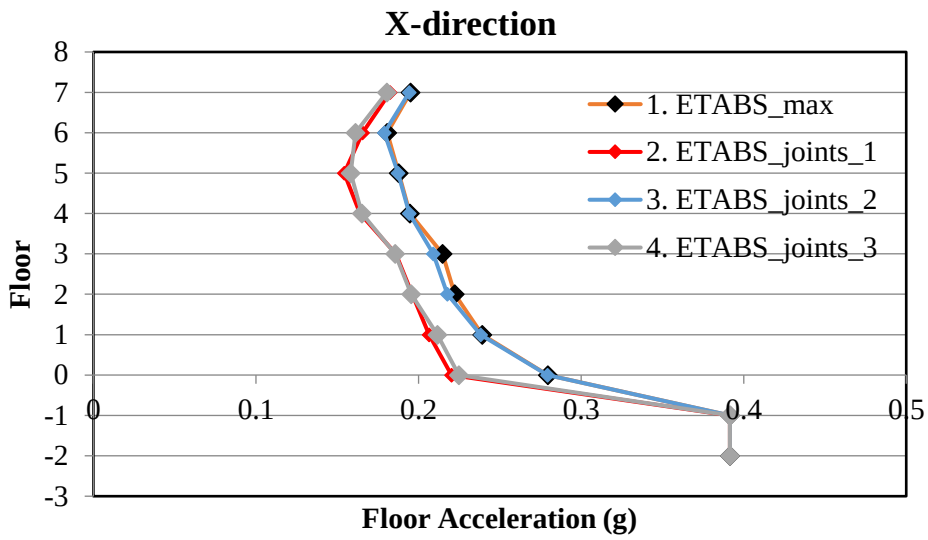


Figure B-2: Acceleration comparison of average of 7 ground motions from three different locations and the maximum response in the X direction

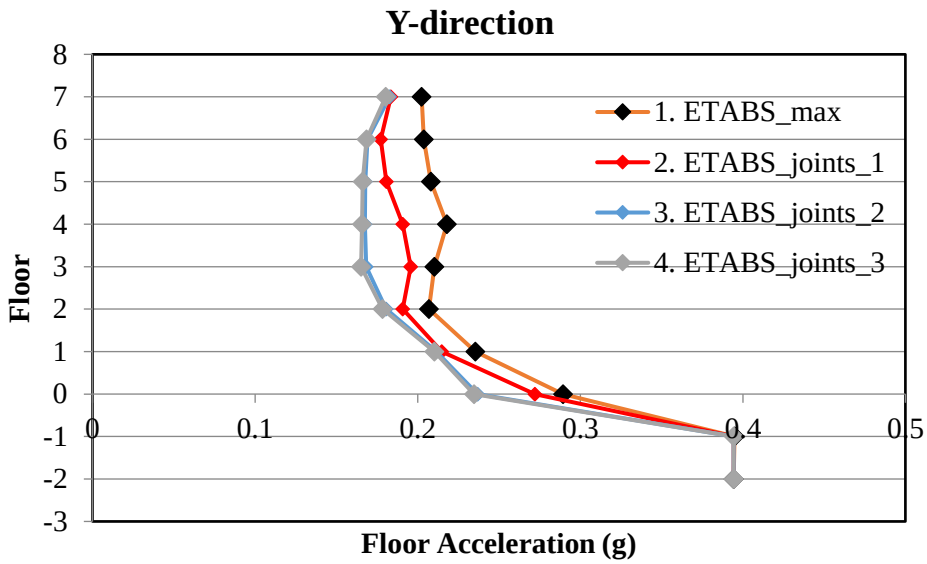


Figure B-2: Acceleration comparison of average of 7 ground motions from three different locations and the maximum response in the Y direction

## C. Appendix C – Hysteresis Curves Comparison for Westmorland, 1982 (RSN316) and Chalfant Valley-02 (RSN558) Ground Motions

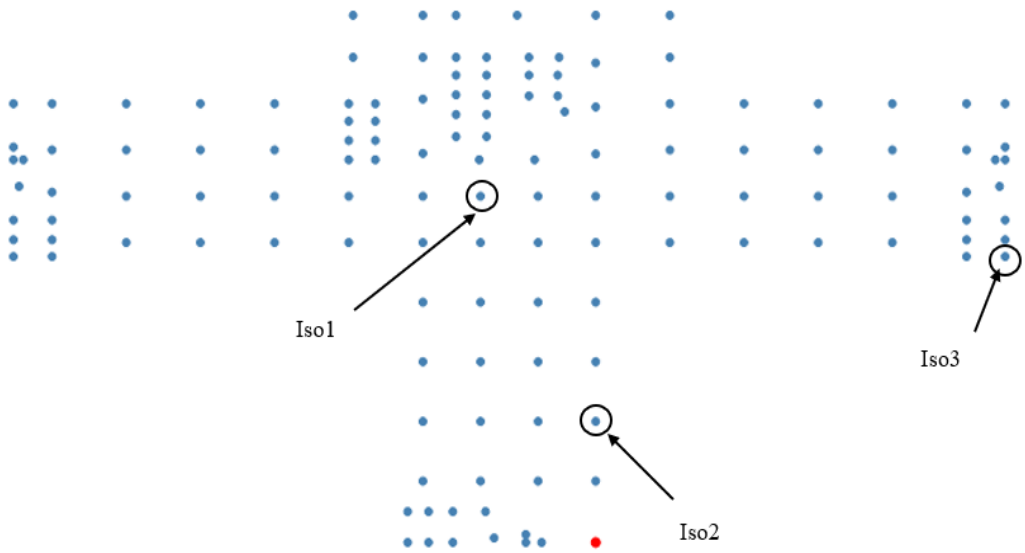


Figure C-1: The selected isolator locations to compare hysteretic response (the isolator layout is retrieved from ETABS plugin by Ulker Eng.)

- **HDRB Comparison**

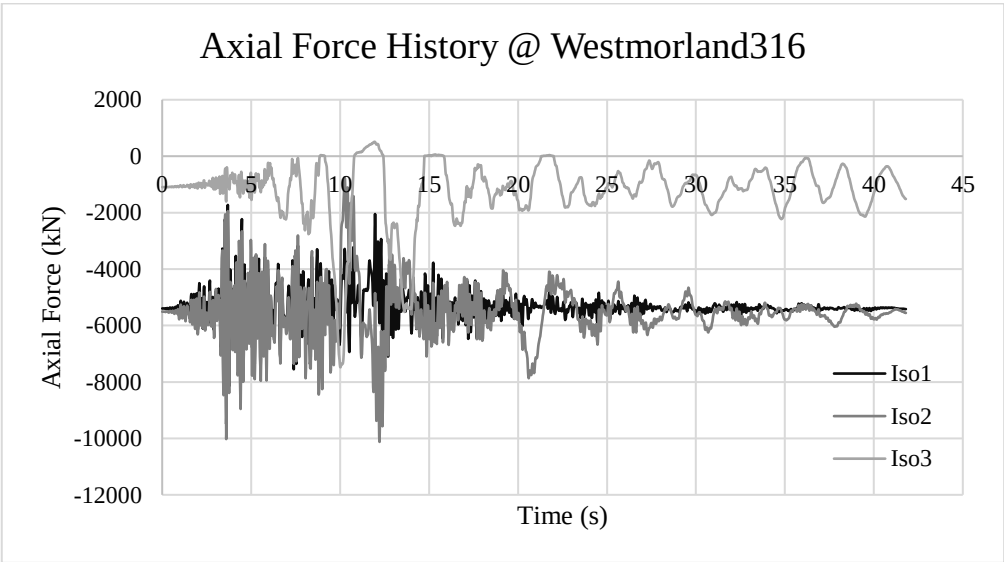


Figure C-2: Axial load history of selected isolators for RSN316 ground motion

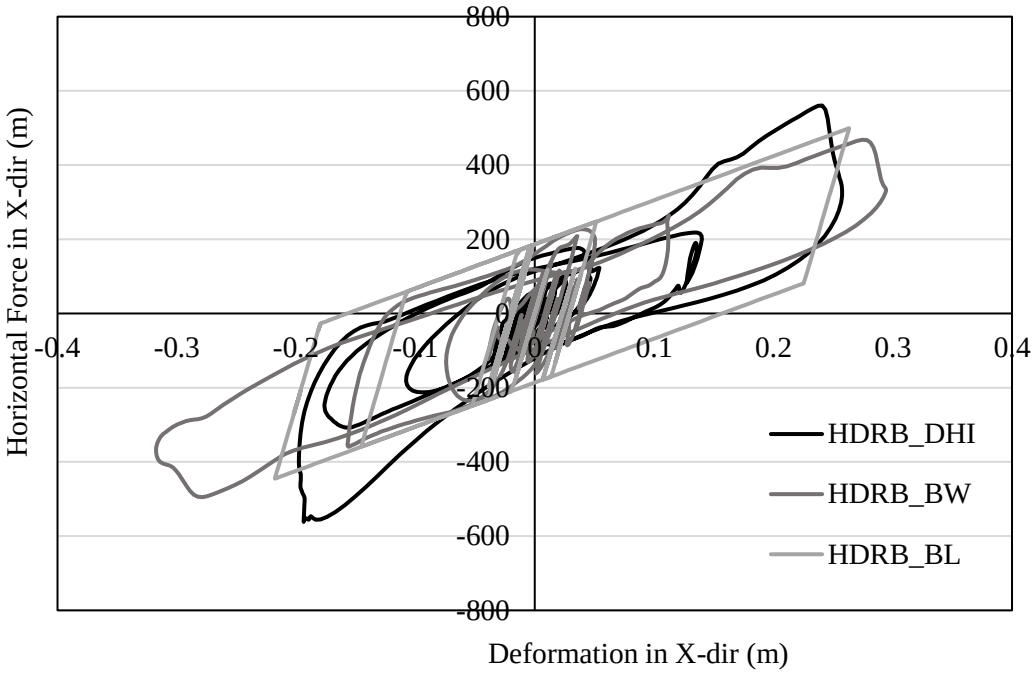


Figure C-3: Hysteresis of Iso1 models under RSN316 ground motion in X dir.

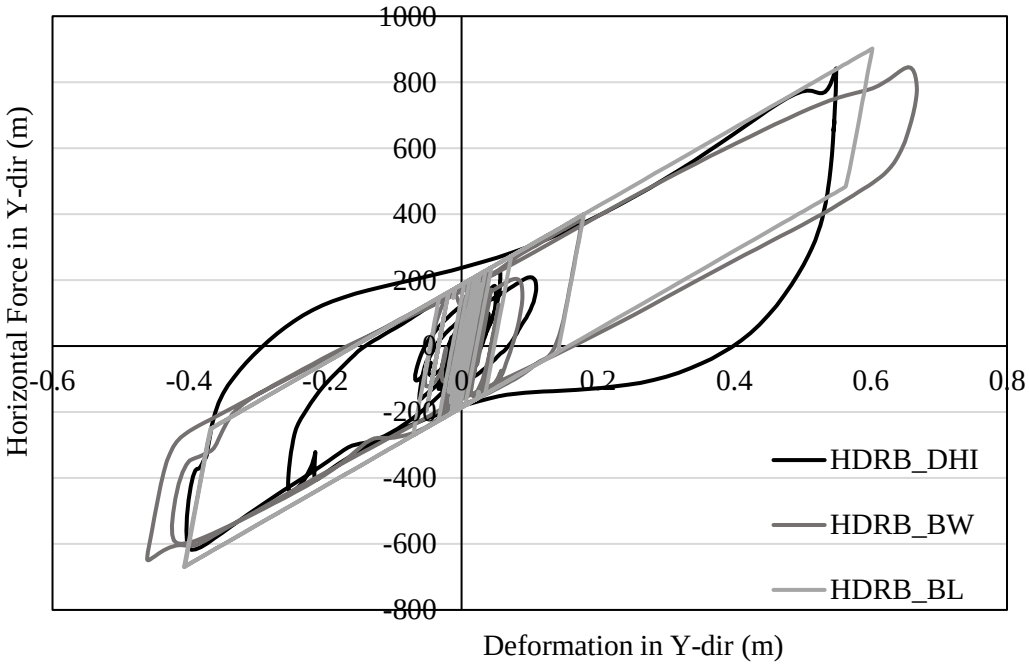


Figure C-4: Hysteresis of Iso1 models under RSN316 ground motion in Y dir.

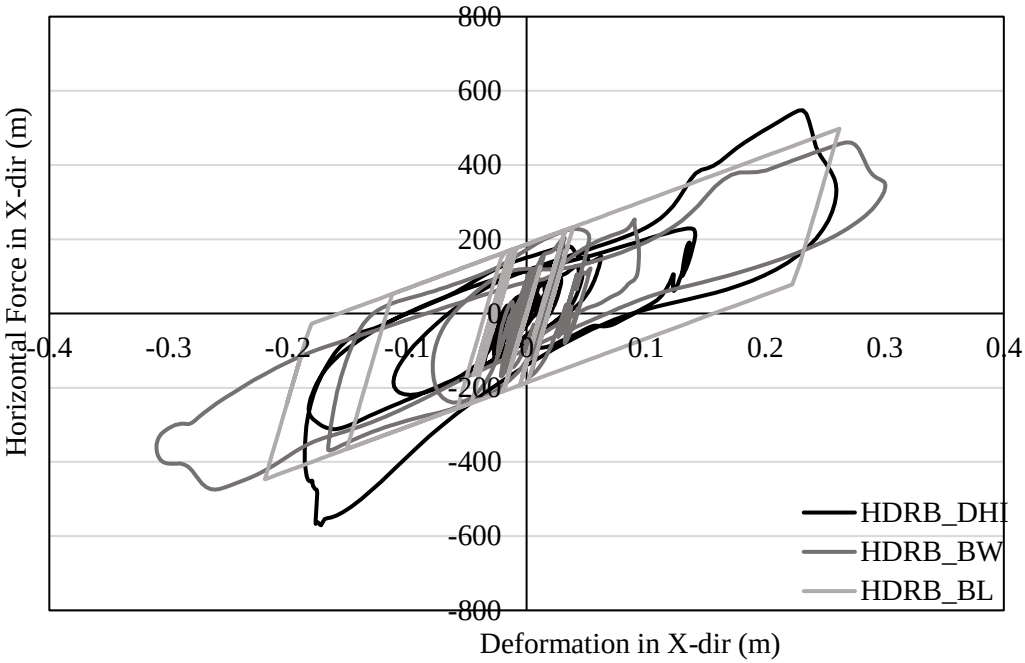


Figure C-5: Hysteresis of Iso2 models under RSN316 ground motion in X dir.

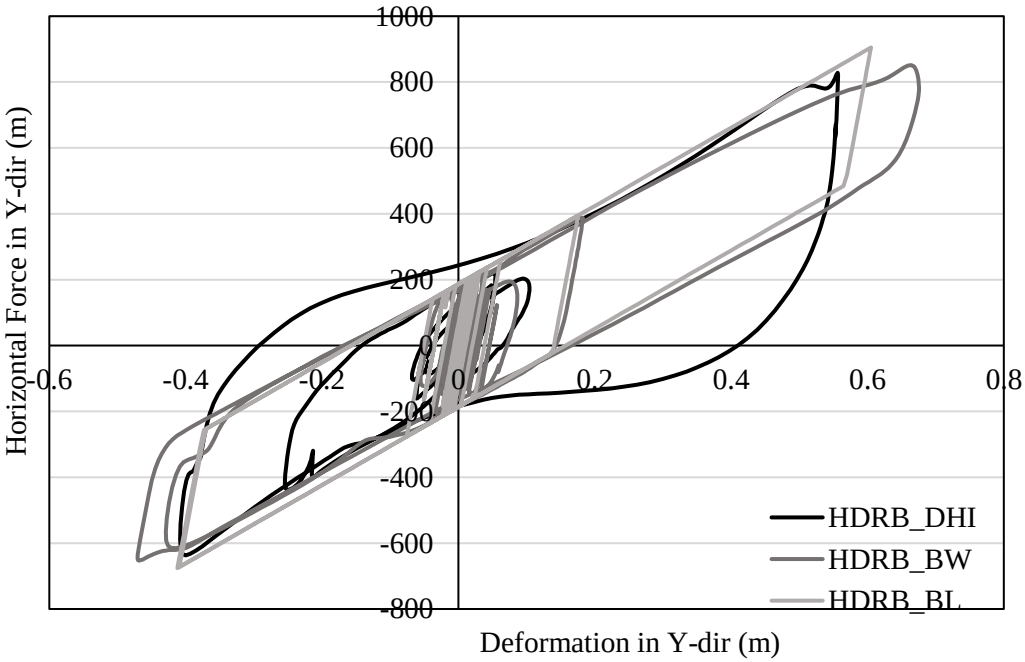


Figure C-6: Hysteresis of Iso2 models under RSN316 ground motion in Y dir.

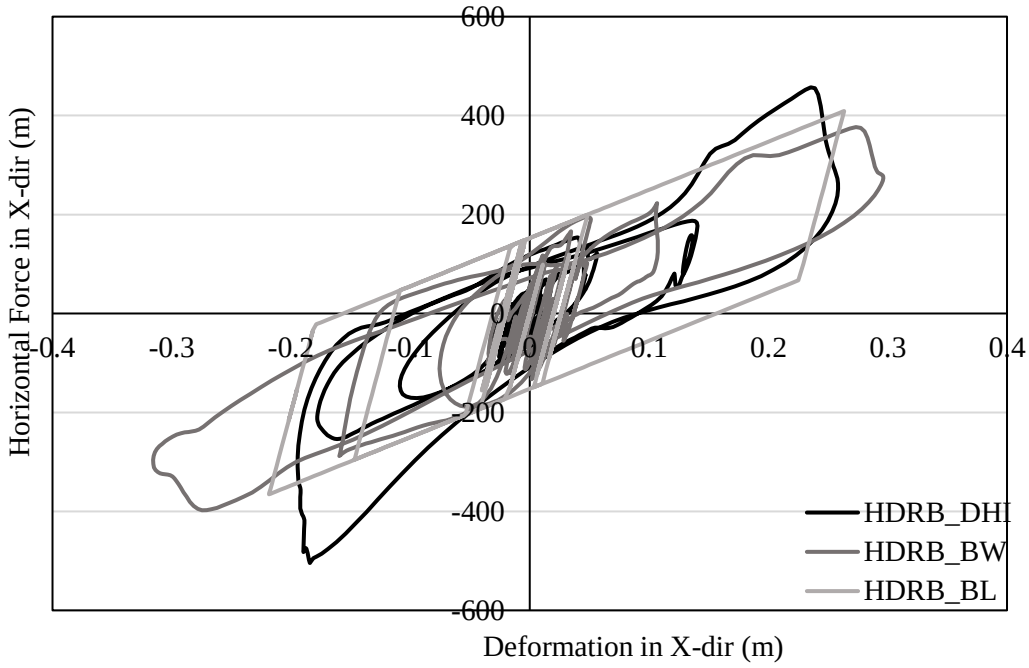


Figure C-7: Hysteresis of Iso3 models under RSN316 ground motion in X dir.

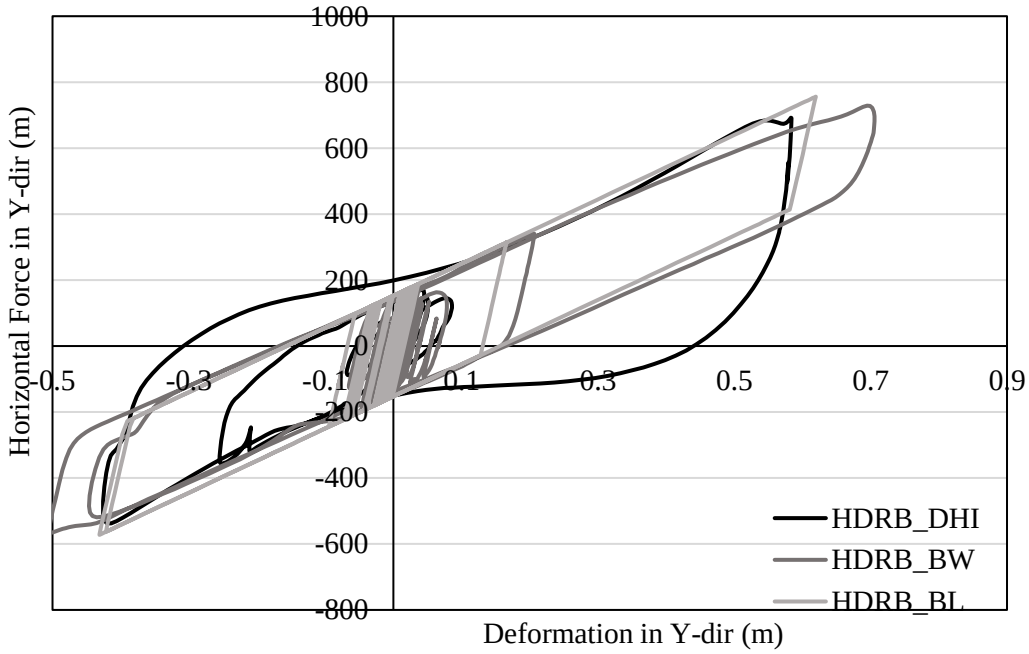


Figure C-8: Hysteresis of Iso3 models under RSN316 ground motion in Y dir.

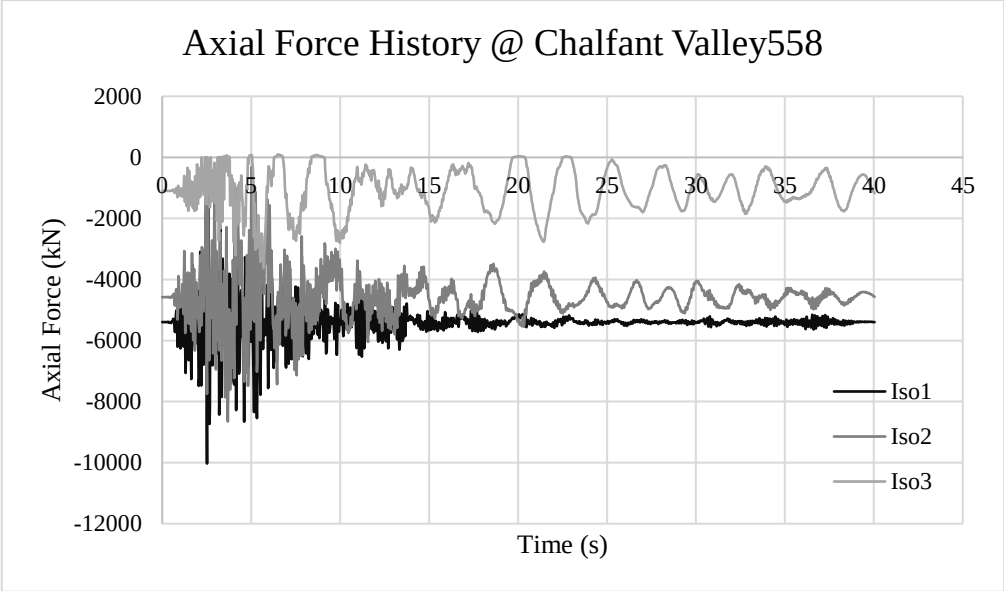


Figure C-9: Axial load history of selected isolators for RSN558 ground motion

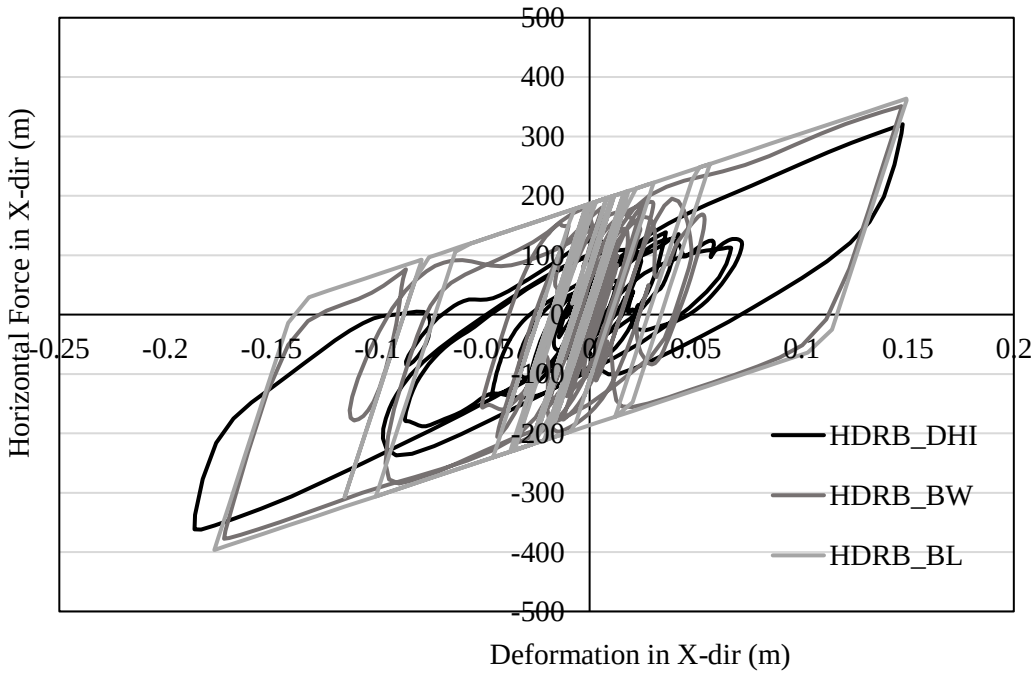


Figure C-10: Hysteresis of Iso1 models under RSN558 ground motion in X dir.

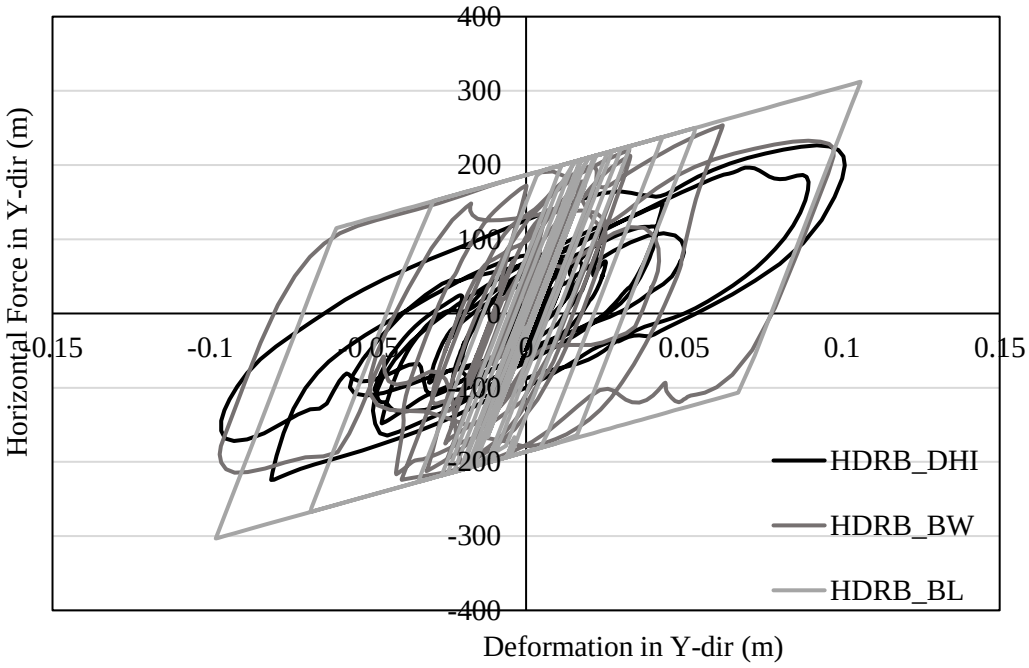


Figure C-11: Hysteresis of Iso1 models under RSN558 ground motion in Y dir.

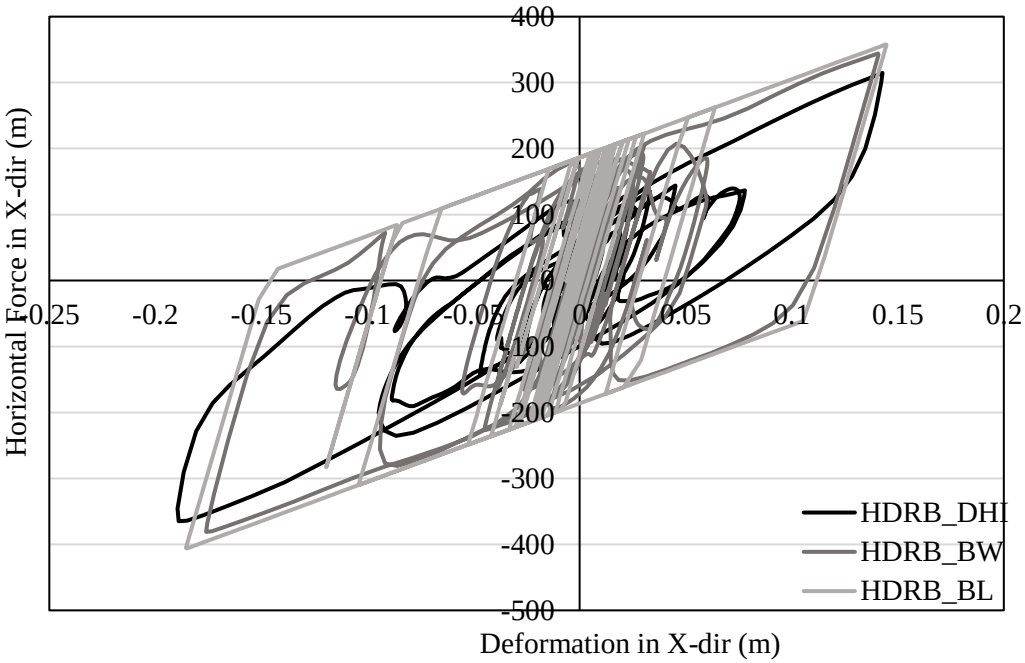


Figure C-11: Hysteresis of Iso2 models under RSN558 ground motion in X dir.

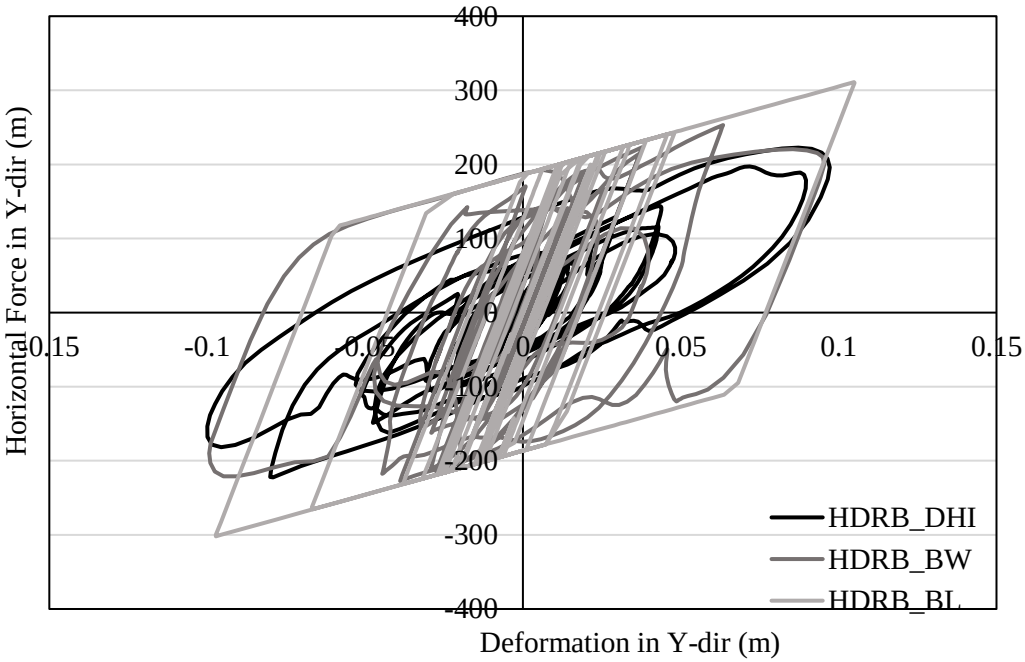


Figure C-12: Hysteresis of Iso2 models under RSN558 ground motion in Y dir.

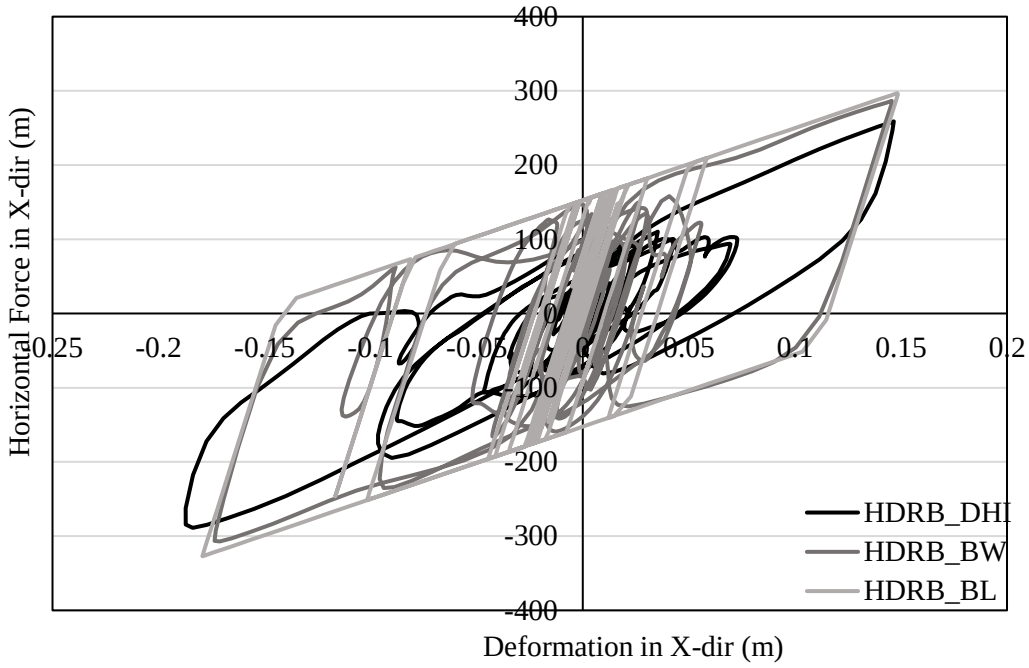


Figure C-13: Hysteresis of Iso3 models under RSN558 ground motion in X dir.

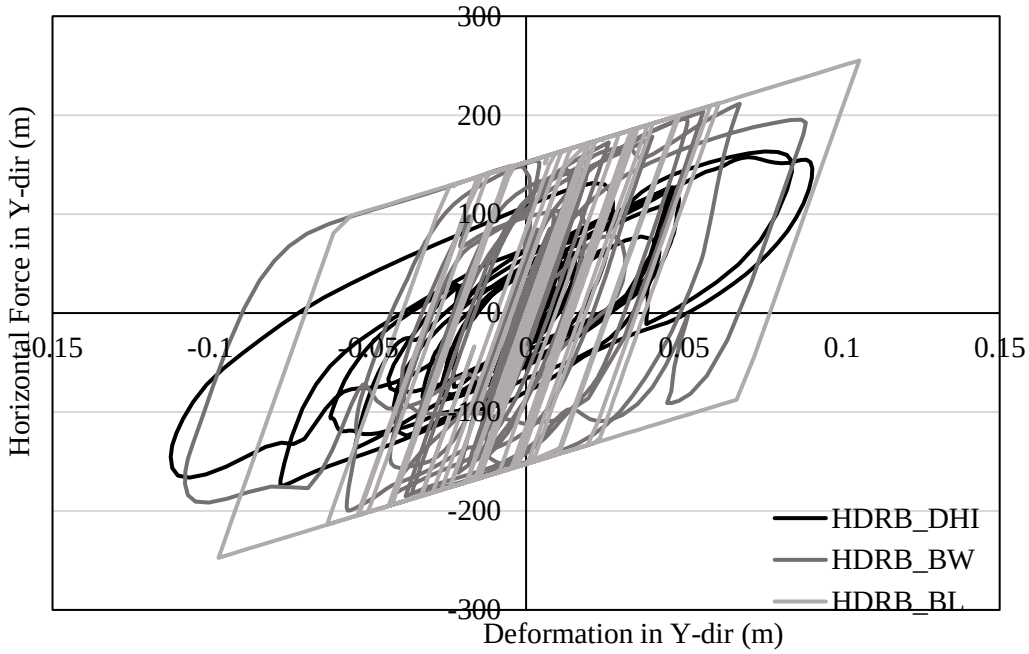


Figure C-14: Hysteresis of Iso3 models under RSN558 ground motion in X dir.

- **FPS Comparison**

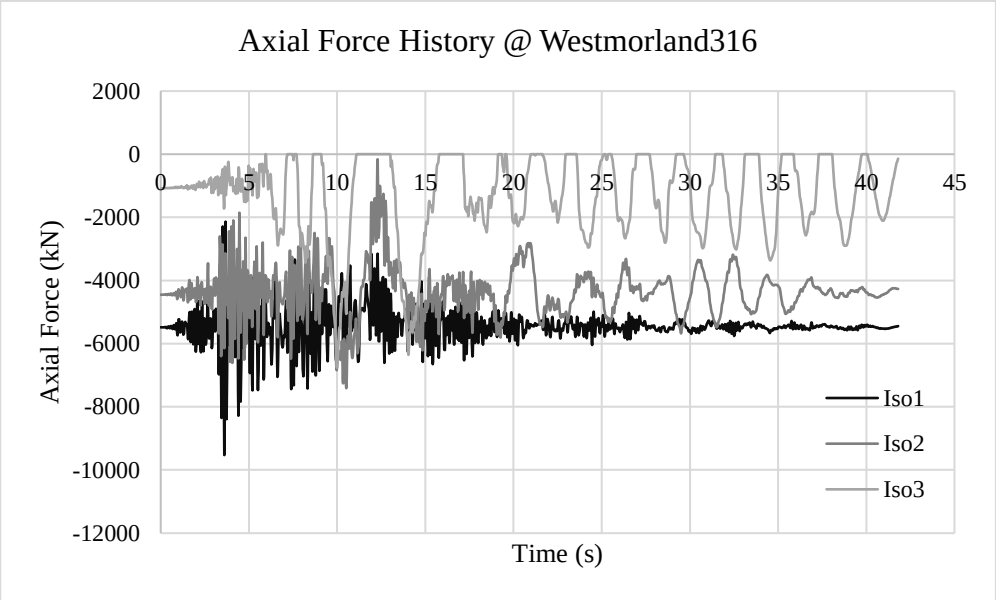


Figure C-15: Axial load history of selected isolators for RSN316 ground motion

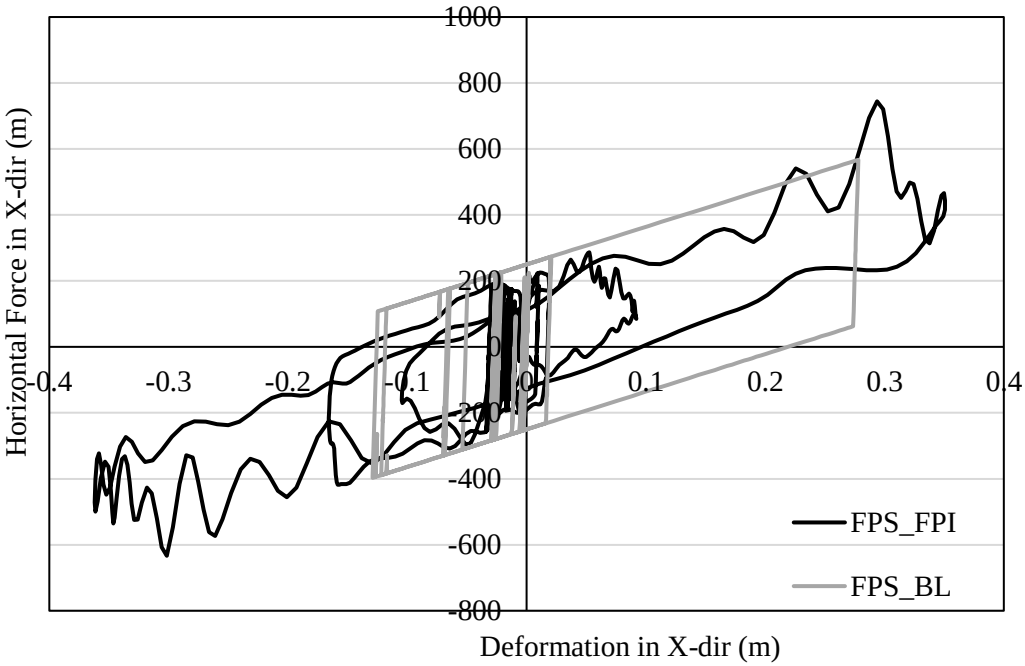


Figure C-16: Hysteresis of Iso1 models under RSN316 ground motion in X dir.

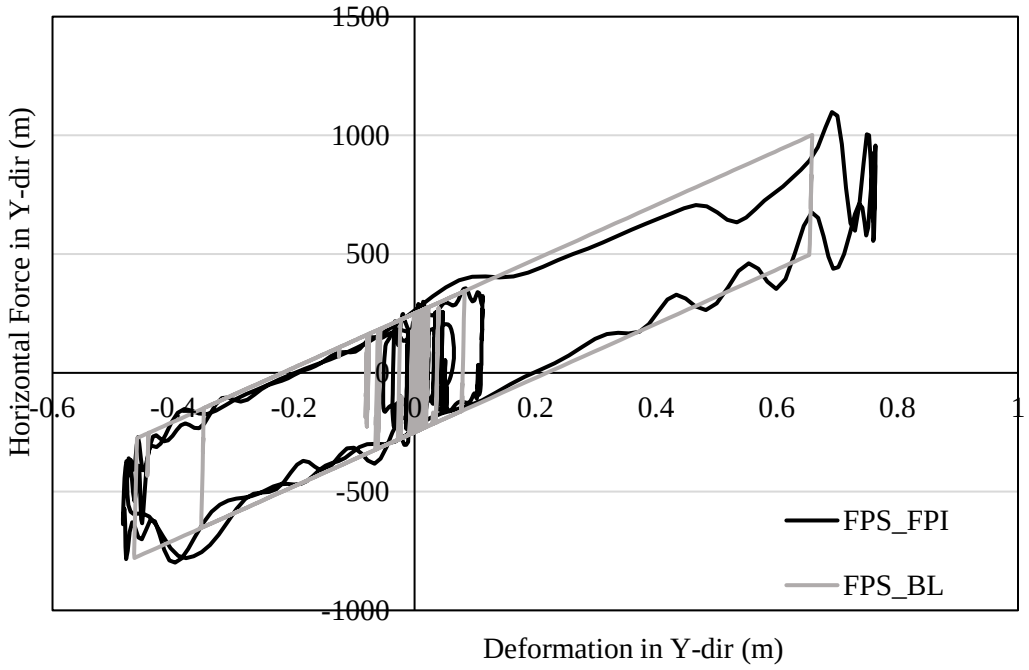


Figure C-17: Hysteresis of Iso1 models under RSN316 ground motion in Y dir.

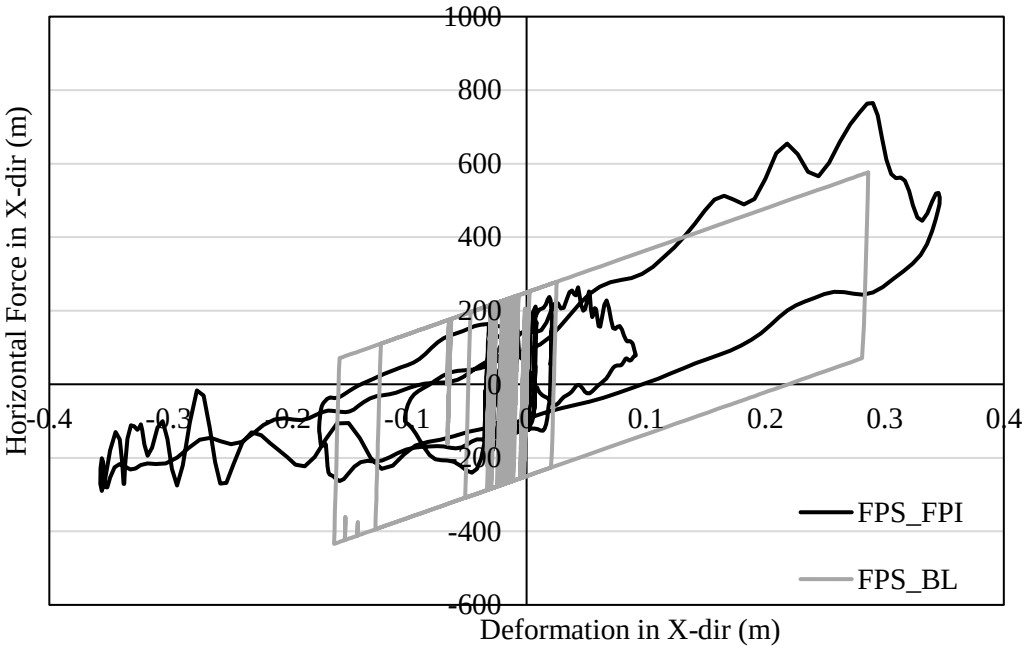


Figure C-18: Hysteresis of Iso2 models under RSN316 ground motion in X dir.

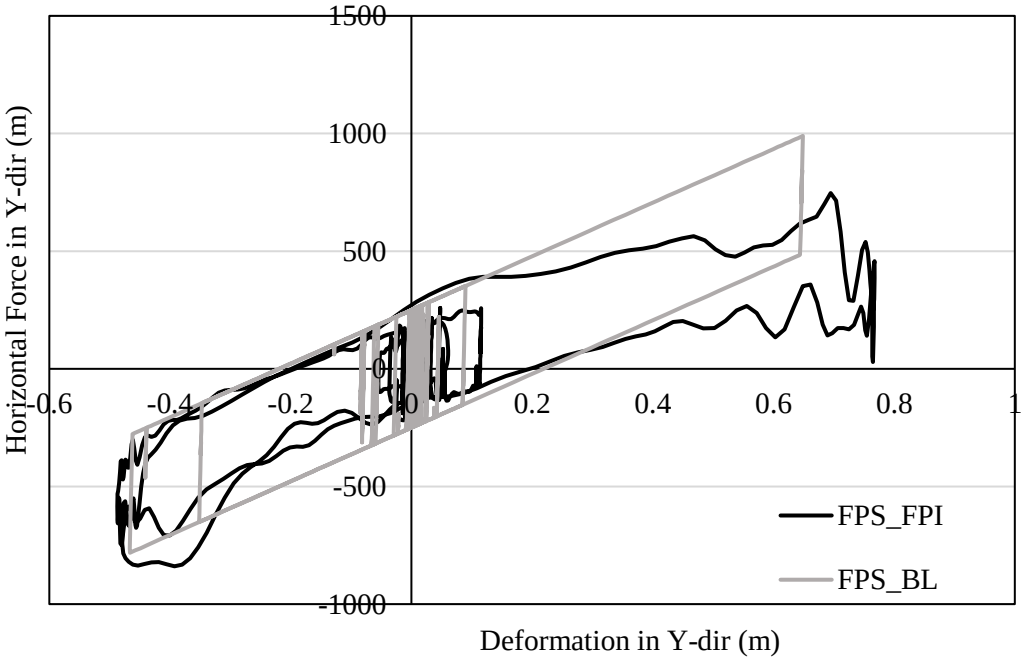


Figure C-19: Hysteresis of Iso2 models under RSN316 ground motion in Y dir.

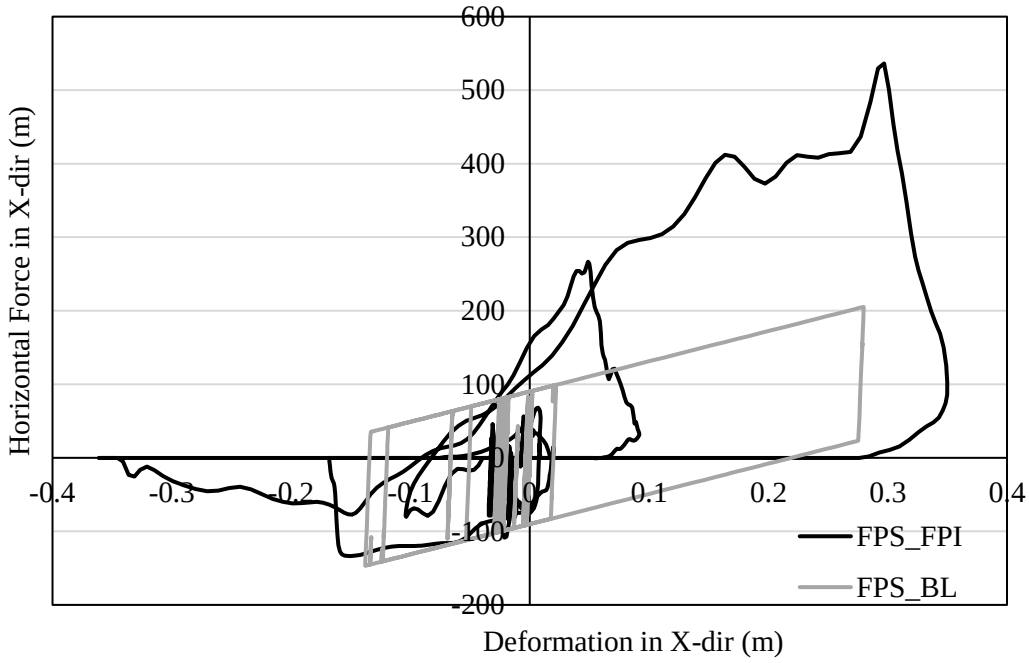


Figure C-20: Hysteresis of Iso3 models under RSN316 ground motion in X dir.

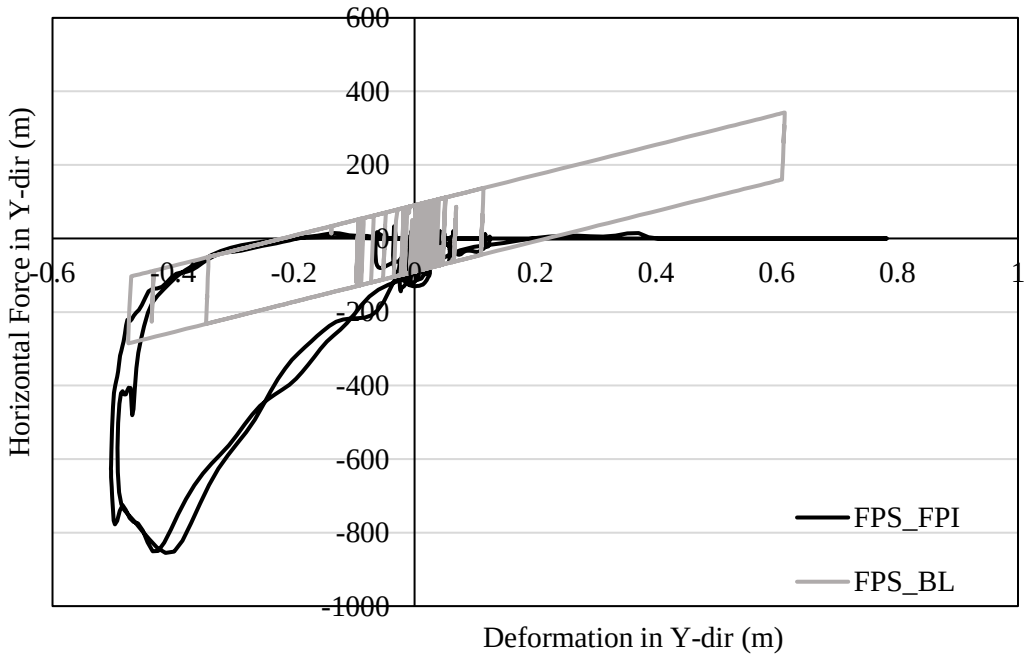


Figure C-21: Hysteresis of Iso3 models under RSN316 ground motion in Y dir.

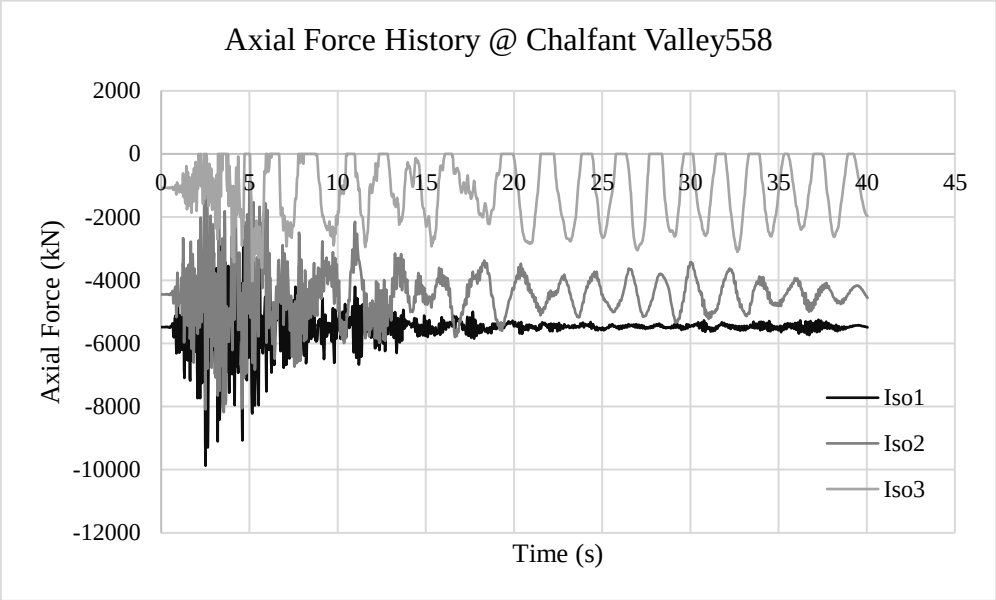


Figure C-22: Axial load history of selected isolators for RSN558 ground motion

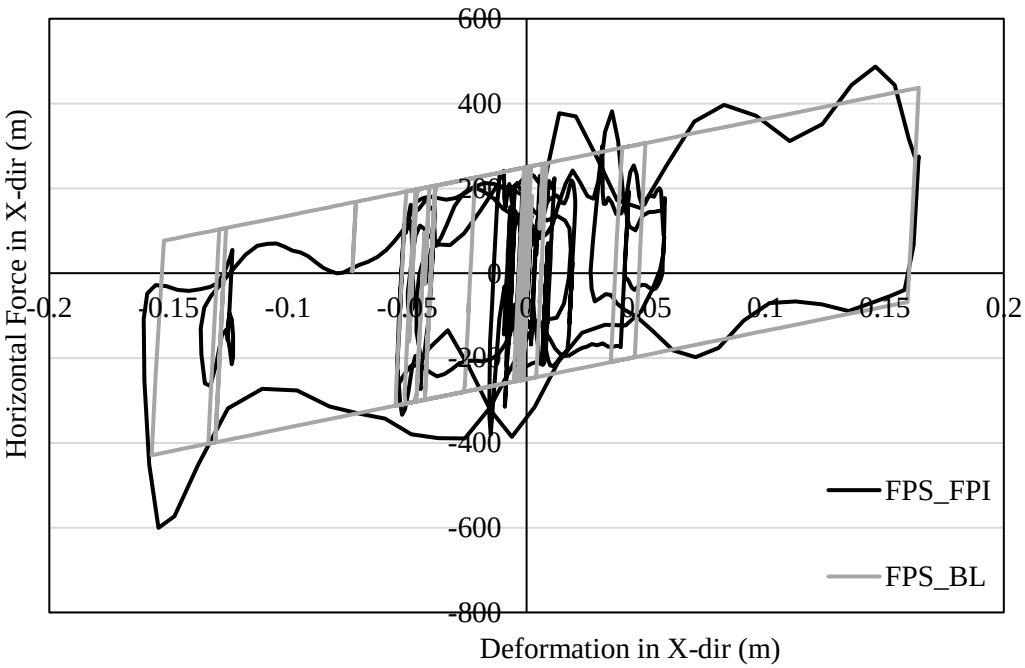


Figure C-23: Hysteresis of Iso1 models under RSN558 ground motion in X dir.

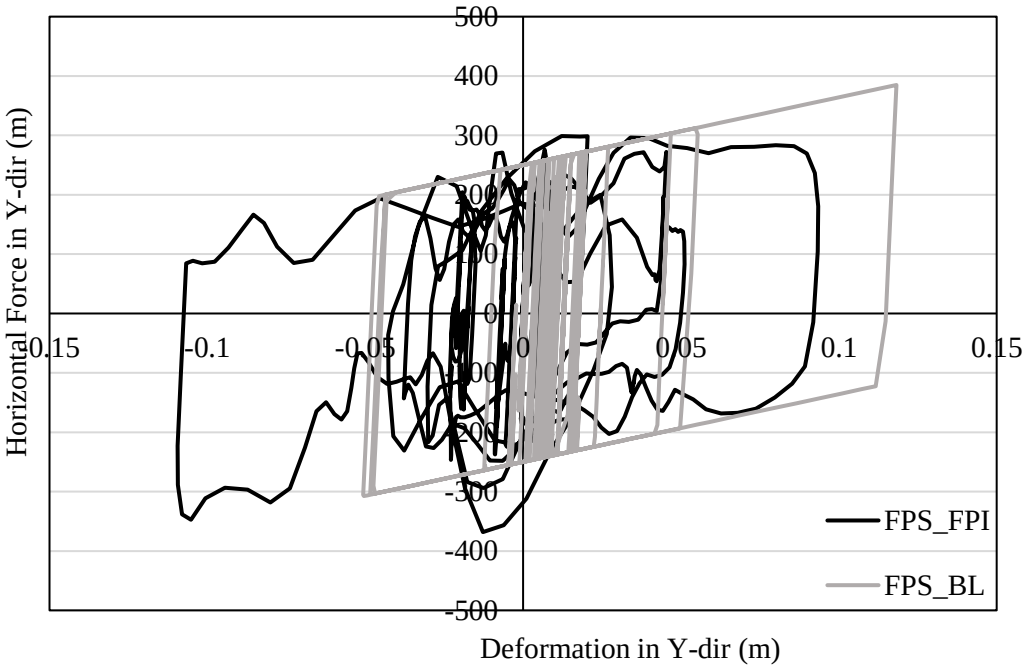


Figure C-24: Hysteresis of Iso1 models under RSN558 ground motion in Y dir.

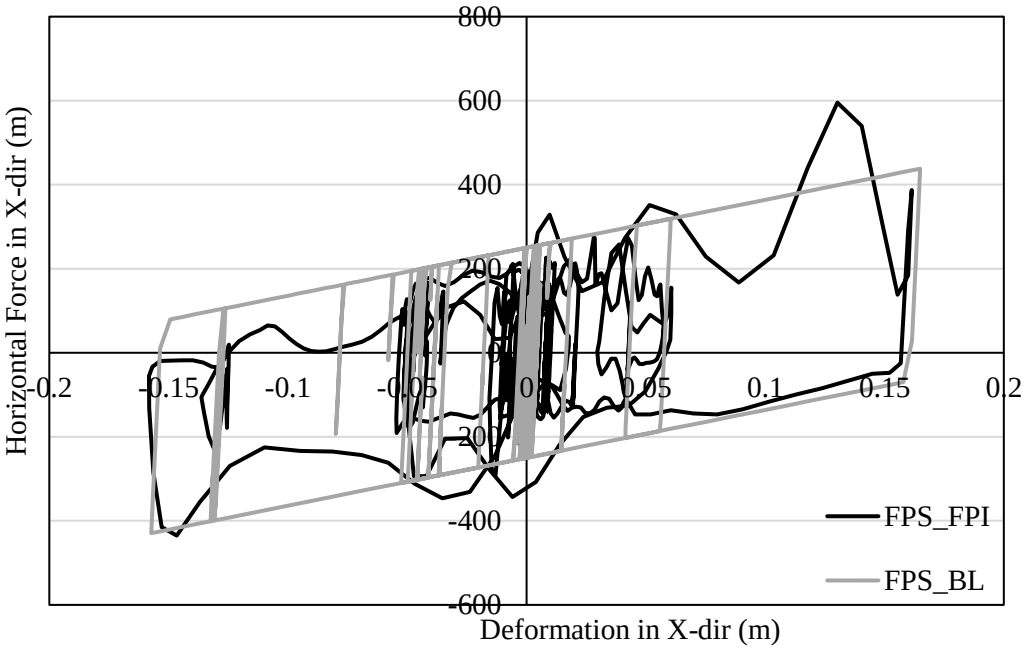


Figure C-25: Hysteresis of Iso2 models under RSN558 ground motion in X dir.

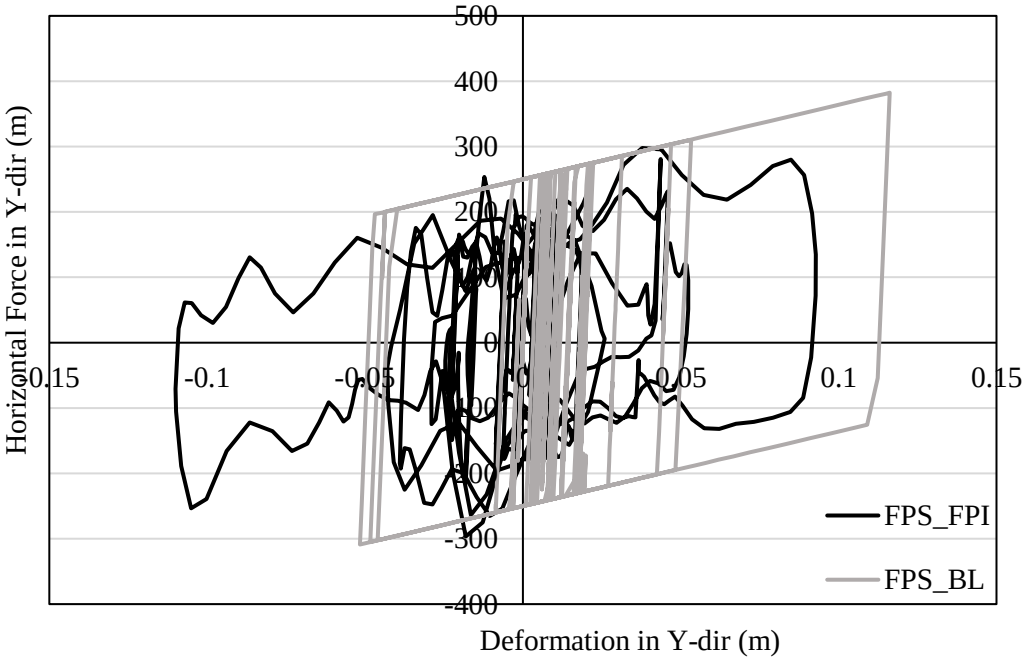


Figure C-26: Hysteresis of Iso2 models under RSN558 ground motion in Y dir.

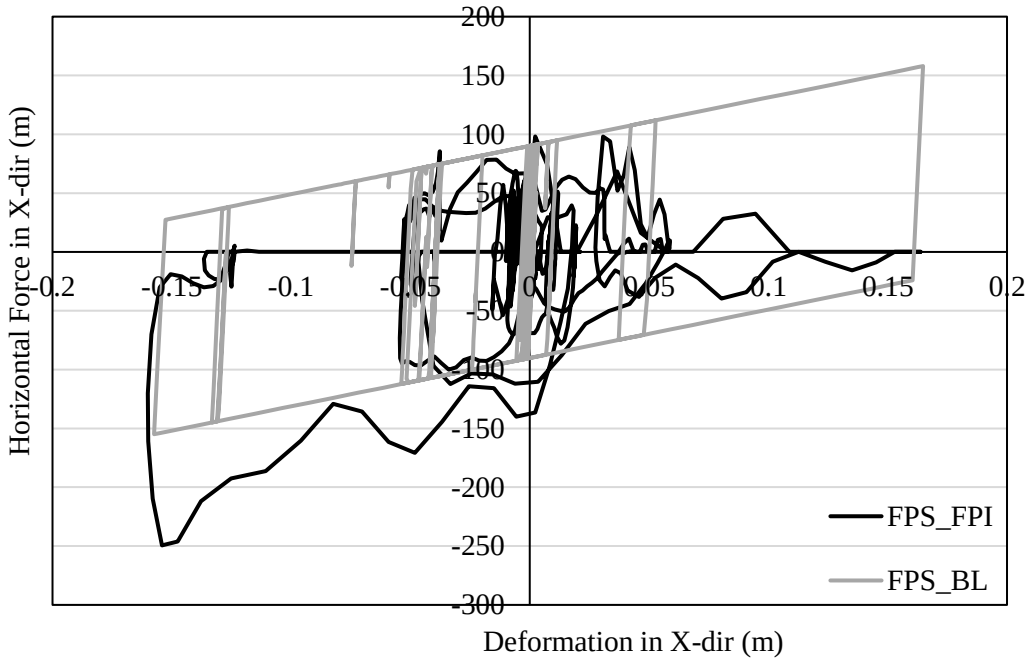


Figure C-27: Hysteresis of Iso3 models under RSN558 ground motion in X dir.

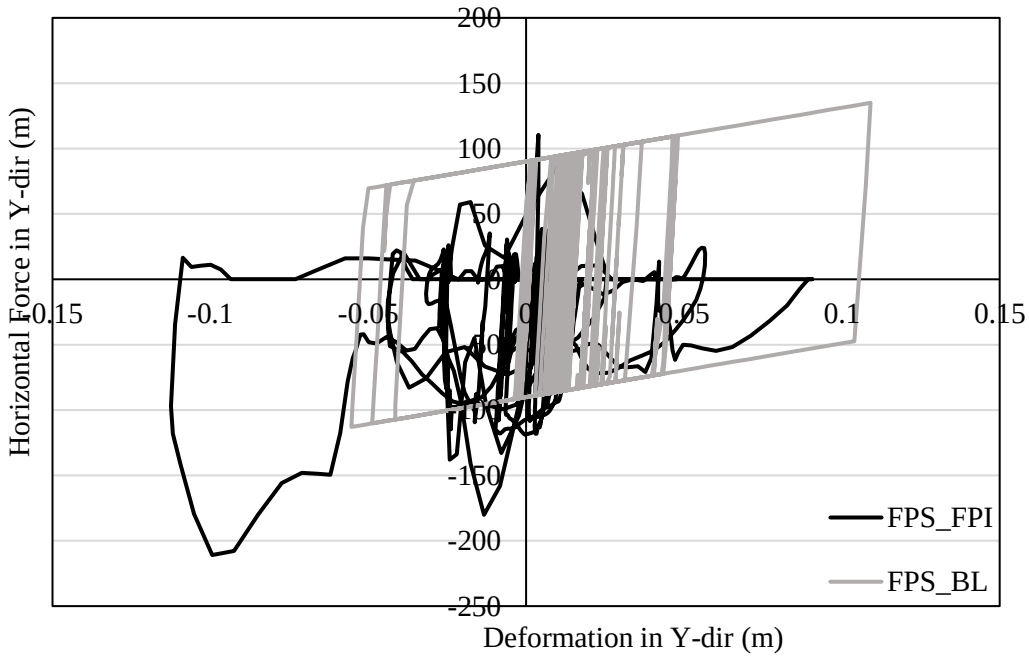


Figure C-28: Hysteresis of Iso3 models under RSN558 ground motion in Y dir.

## D. Appendix D – Performance Comparison for 5% and 2% superstructural damping

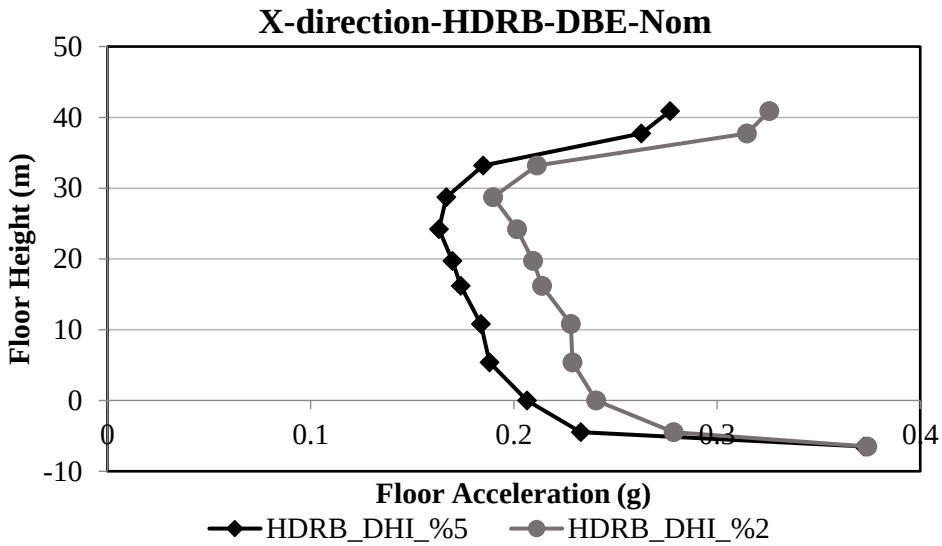


Figure D-1: Average floor accelerations for HDRB models in X direction

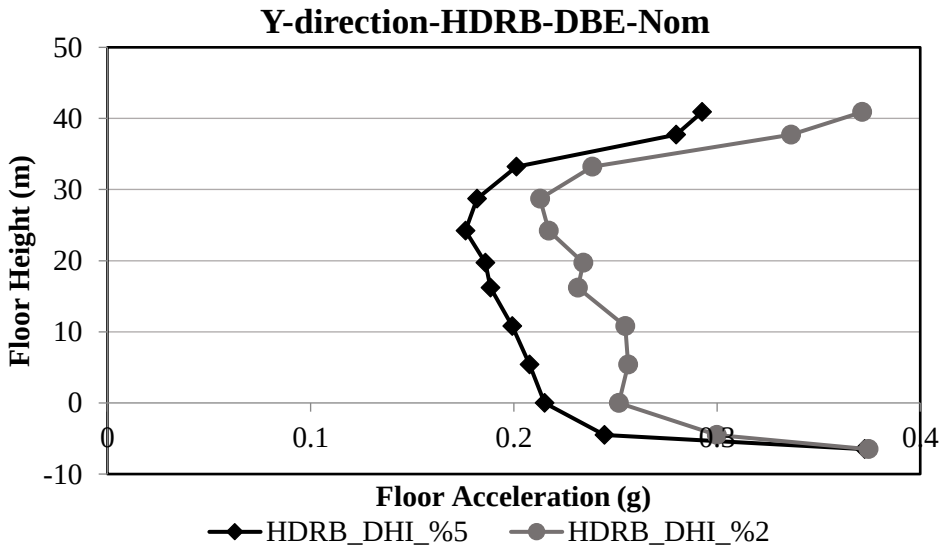


Figure D-2: Average floor accelerations for HDRB models in Y direction

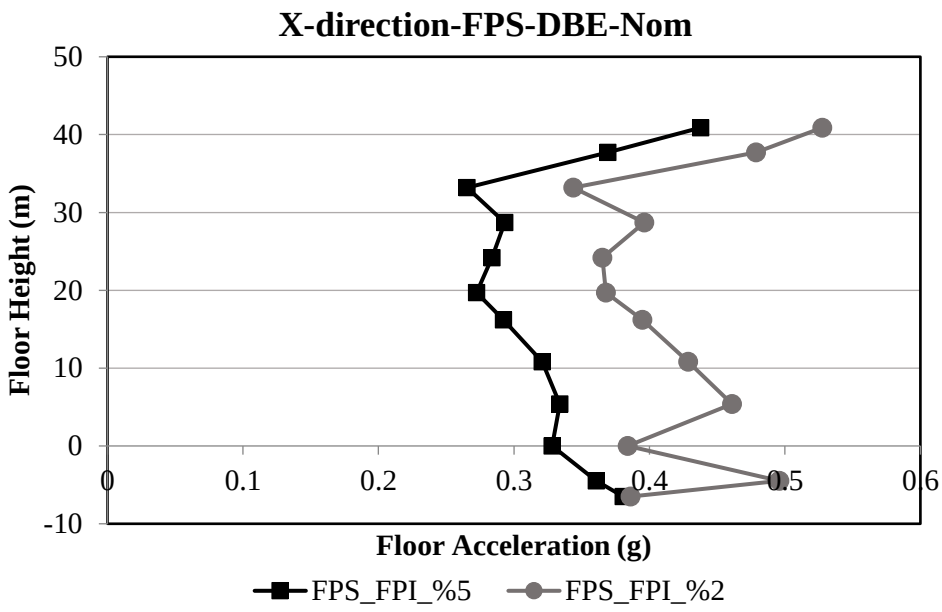


Figure D-3: Average floor accelerations for FPS models in X direction

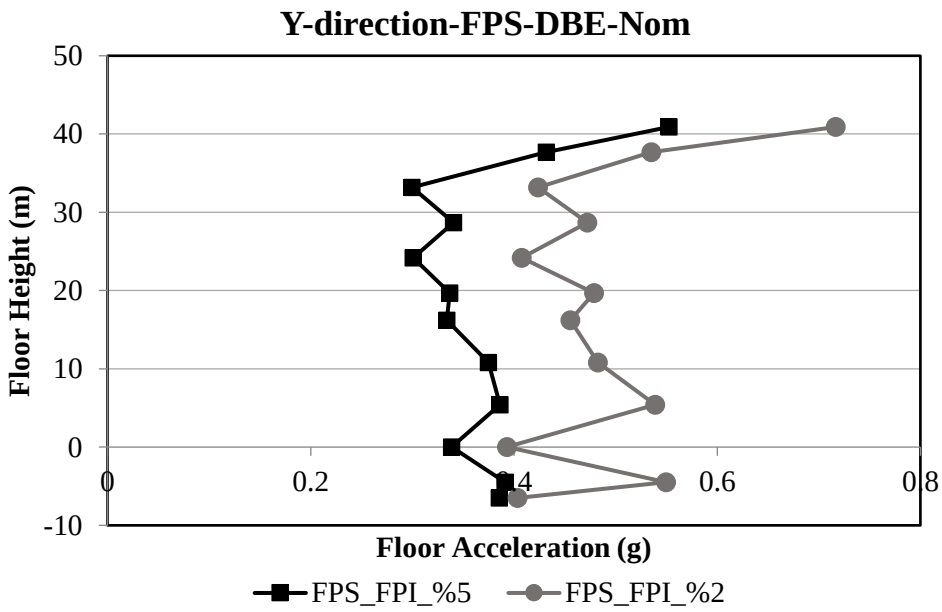


Figure D-4: Average floor accelerations for FPS models in Y direction

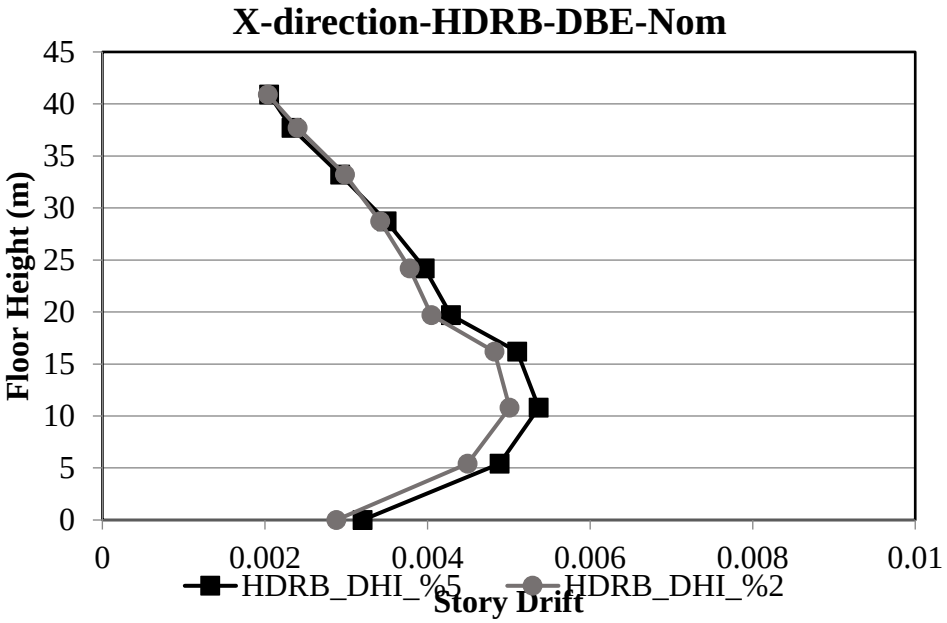


Figure D-5: Average interstory drifts for HDRB models in X direction

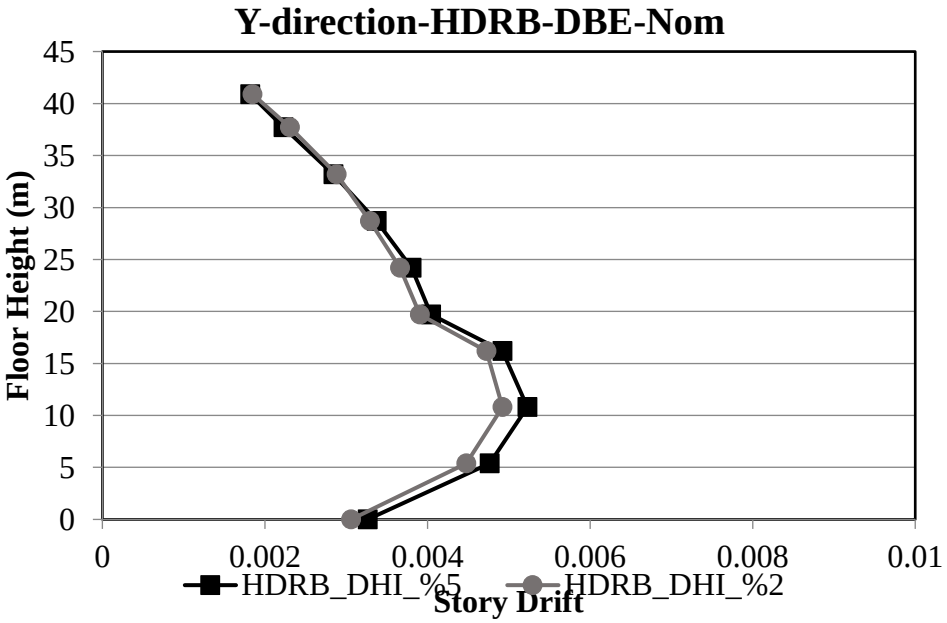


Figure D-6: Average interstory drifts for HDRB models in Y direction

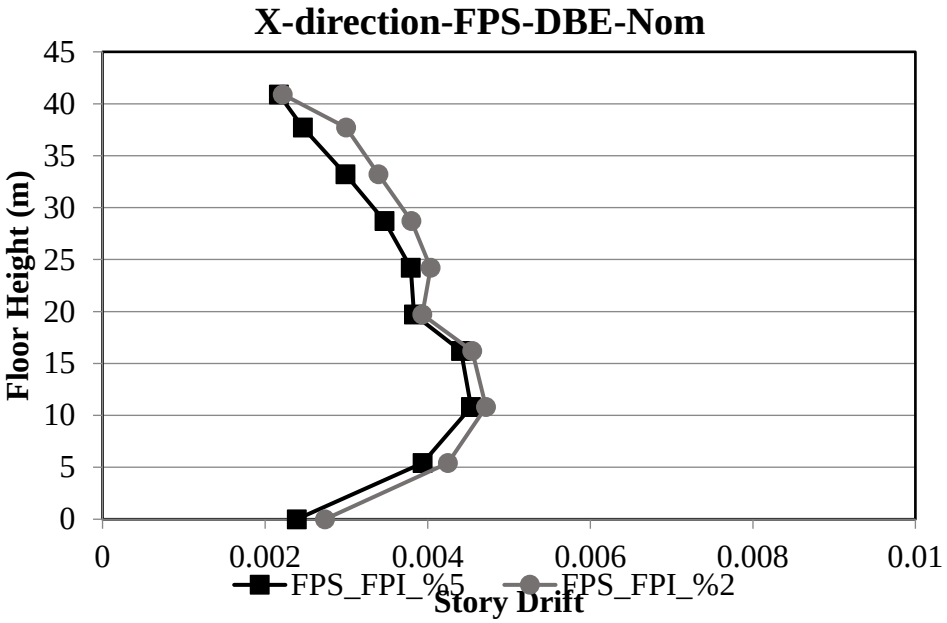


Figure D-7: Average interstory drifts for FPS models in X direction

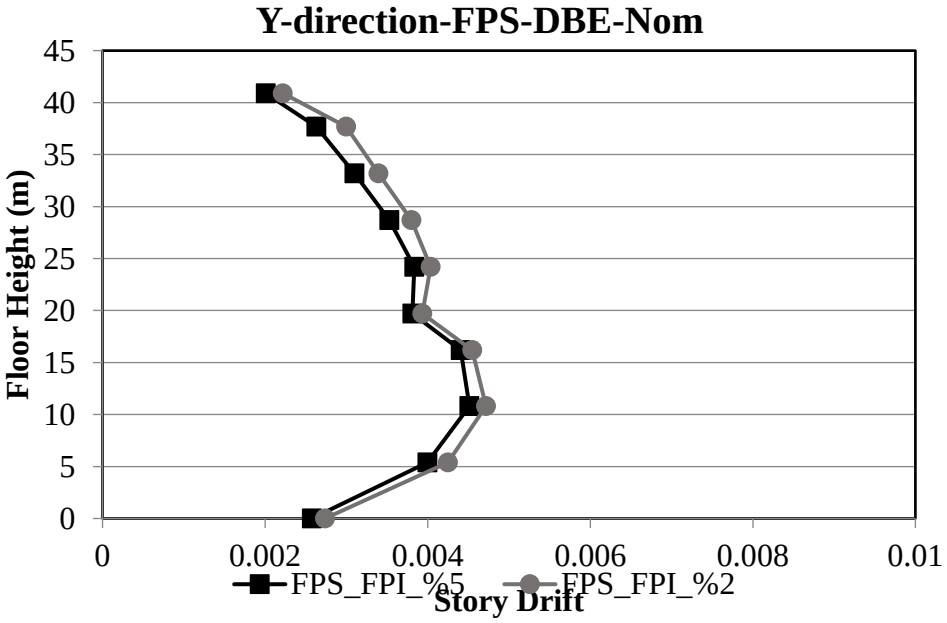


Figure D-8: Average interstory drifts for FPS models in Y direction

## E. Appendix E – Performance Comparison for FNA and DI methods

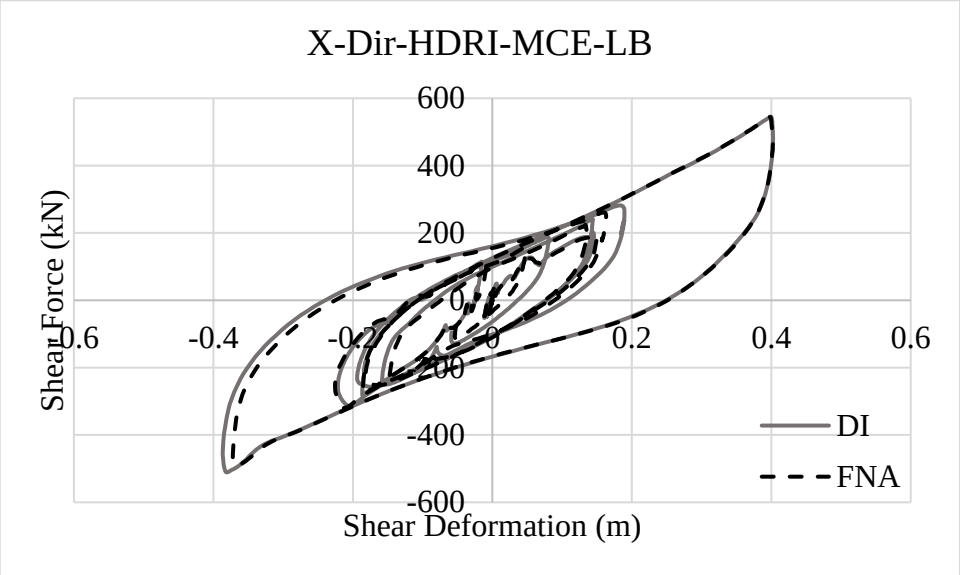


Figure E-1: Hysteresis curves for Iso3 under Kocaeli1158 ground motion in X dir

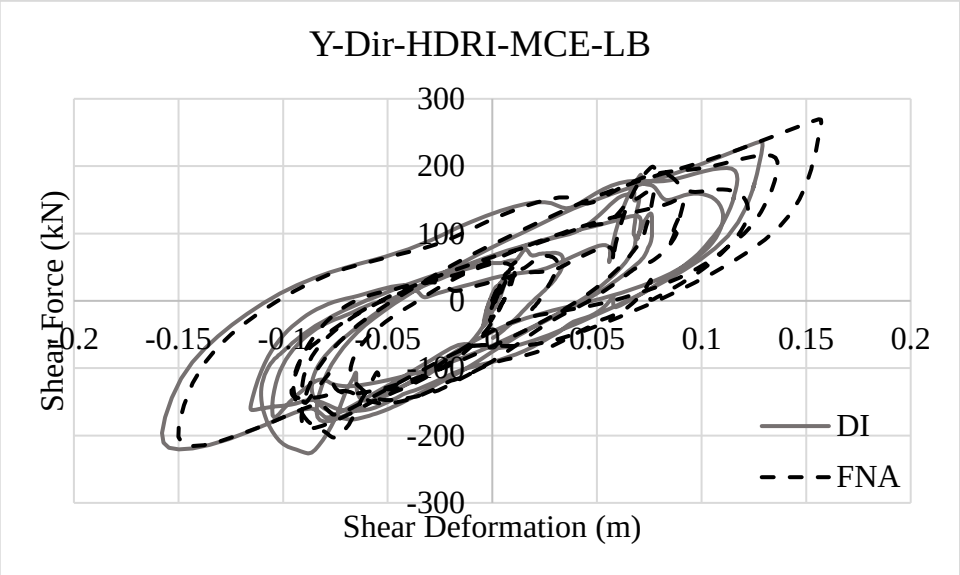


Figure E-2: Hysteresis curves for Iso3 under Kocaeli1158 ground motion in Y dir

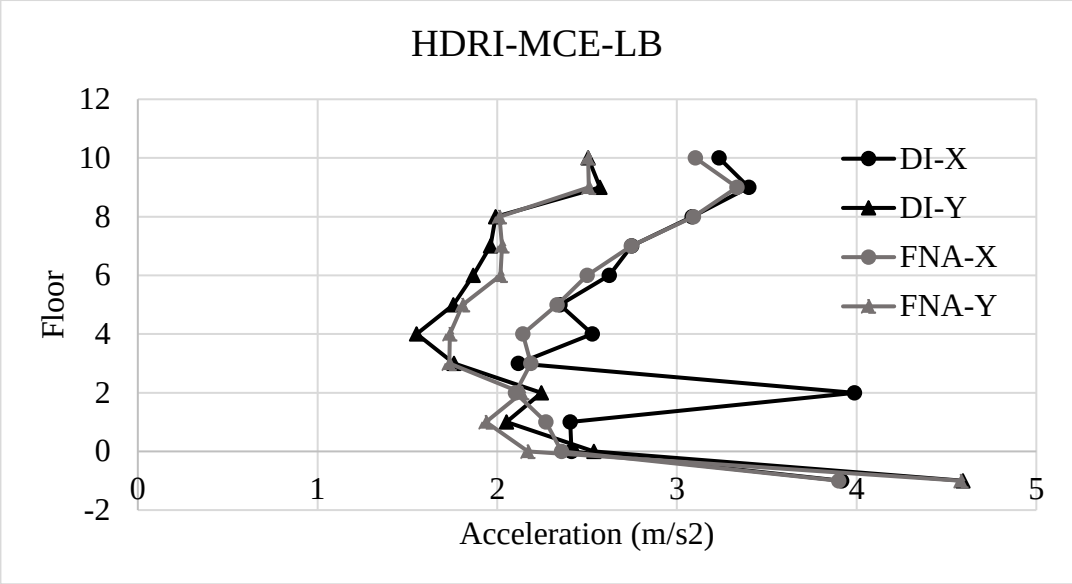


Figure E-3: Floor acceleration for Iso3 under Kocaeli1158 ground motion

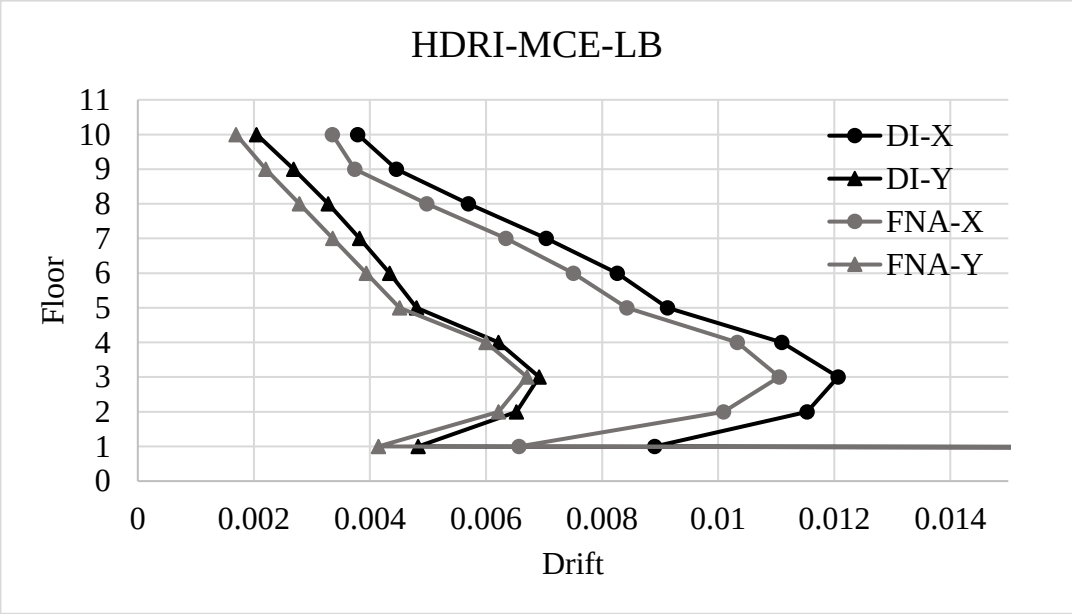


Figure E-3: Inter-story drifts for Iso3 under Kocaeli1158 ground motion

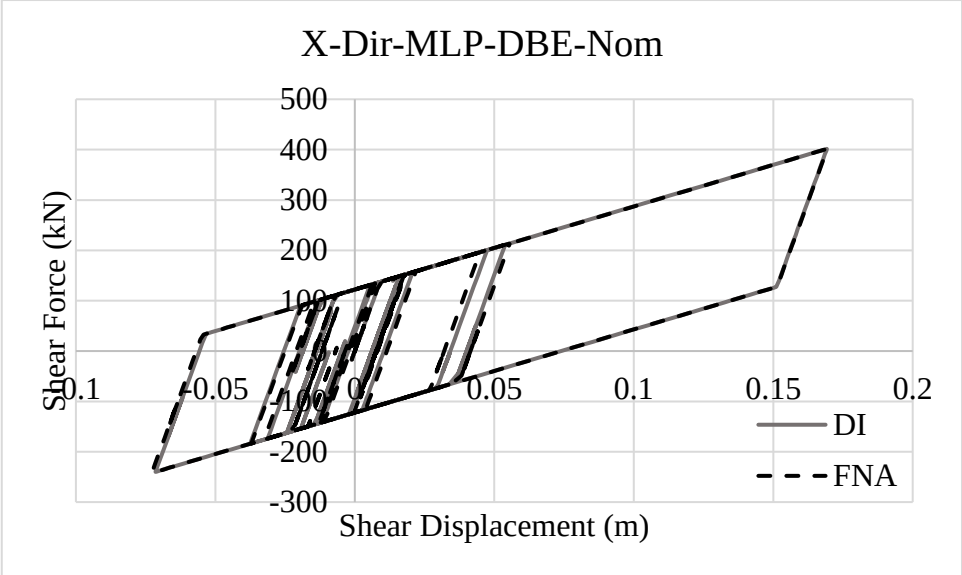


Figure E-5: Hysteresis curves for Iso3 under Duzce1605 ground motion in X dir

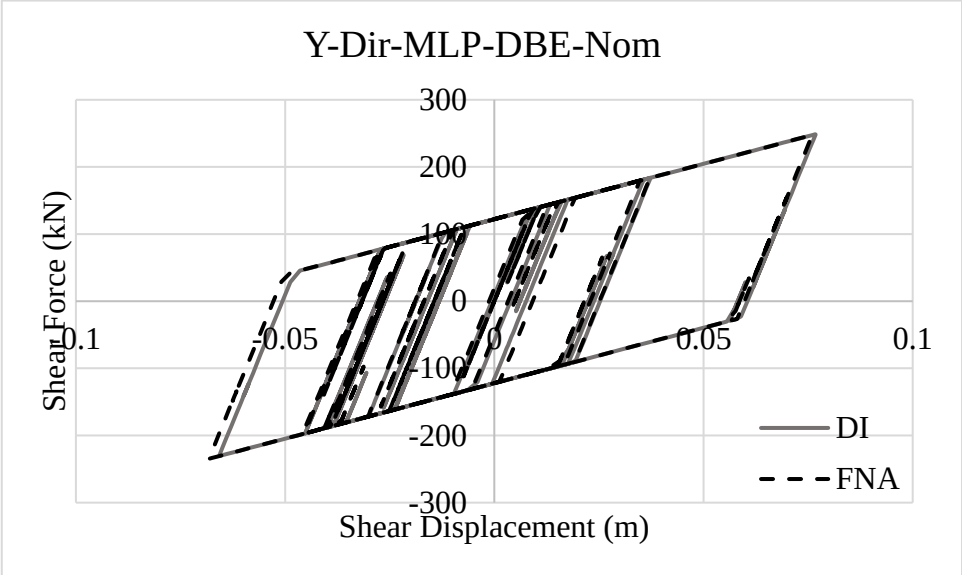


Figure E-6: Hysteresis curves for Iso3 under Duzce1605 ground motion in Y dir

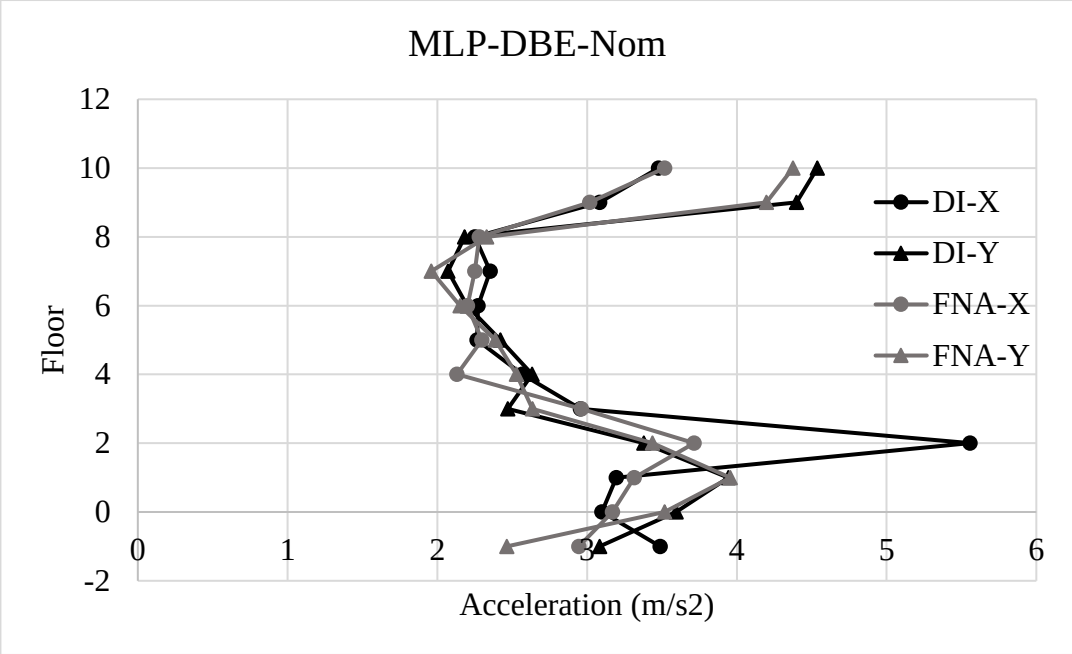


Figure E-7: Floor accelerations for Iso3 under Duzce1605 ground motion

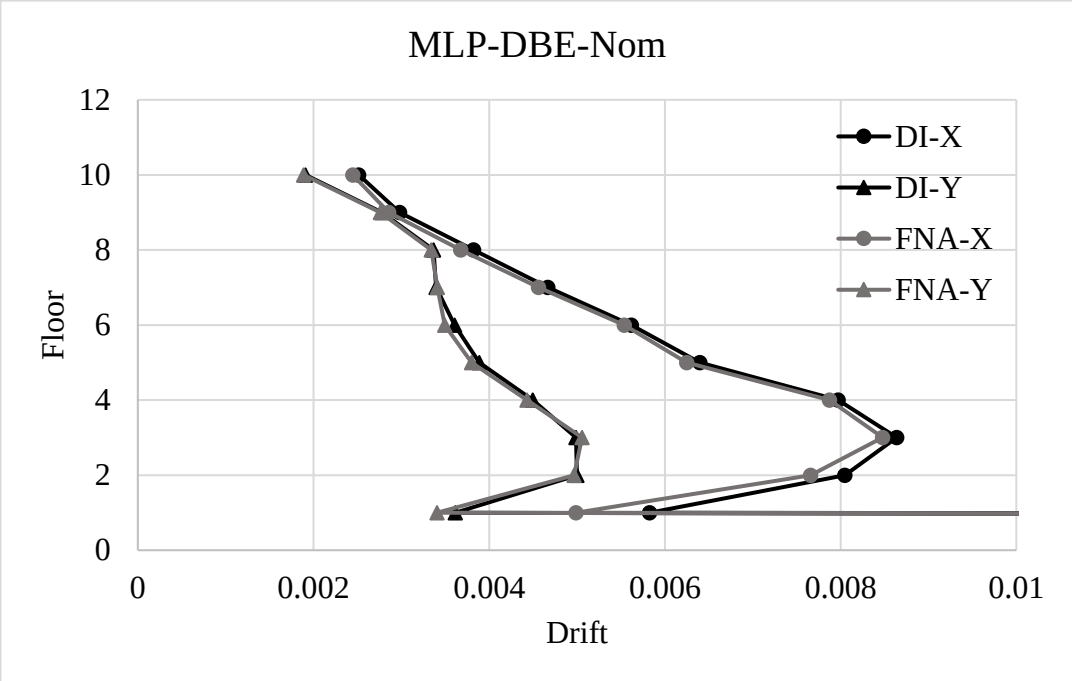


Figure E-8: Inter-story drifts for Iso3 under Duzce1605 ground motion